MORPHOLOGY AND CHARGE TRANSPORT IN POLYMER ORGANIC SEMICONDUCTOR FIELD-EFFECT TRANSISTORS

ZHUO JINGMEI

(B.Sc. (Hons.), NUS)

A THESIS SUBMITTED

FOR THE DEGREE OF DOCTOR OF PHILOSOPHY

DEPARTMENT OF CHEMISTRY

NATIONAL UNIVERSITY OF SINGAPORE

2011

For my parents

For Jianxiang

Acknowledgements

The work described in this thesis was carried out in the Organic Nano Device Laboratory (ONDL), National University of Singapore, supported by a research scholarship from the Department of Chemistry.

This thesis would not have been possible without the support and assistance from many people whom I would like to thank. I would first like to express my utmost sincere gratitude to my supervisors, Dr Peter Ho and Dr Chua Lay-Lay for giving me the privilege to work in the group. I thank them for their guidance, patience and inspiring words. I am also grateful to Dr Sim Wee Sun for giving me the opportunity to work with him and guiding me in the early years of this research journey.

Thanks to current and former colleagues, Loke Yuen, Zhi Kuang, Li Hong, Rui Qi, Liu Bo, Siva, Zhou Mi, Jon, Roland and Bibin for their wonderful company, encouragement and discussions. Thanks to all junior members in the group for the friendship and adding colors to my PhD journey.

Special thanks to my father for his unconditional support and constant encouragement throughout my University days. Last but not least, a big thanks to Jianxiang for standing by me and being my pillar of strength.

Declaration

The work in this thesis is the original work of ZHUO Jingmei, performed independently under the supervision of Dr Peter Ho and Dr Chua Lay-Lay, (in ONDL), Chemistry/Physics Department, National University of Singapore, between 4 Aug 2007 and 5 Aug 2011.

The content of the thesis has been partly published in:

1. J.-M. Zhuo, L.-H. Zhao, R.-Q. Png, L.-Y. Wong, P.-J. Chia, J.-C. Tang, S. Sivaramakrishnan, M. Zhou, E. C.-W. Ou, S.-J. Chua, W.-S. Sim, L.-L. Chua, P. K.-H. Ho, “Direct spectroscopic evidence for a photodoping mechanism in polythiophene and poly(bithiophene-alt-thienothiophene) organic semiconductor thin films involving oxygen and sorbed moisture”, *Adv. Mater*., 21 (2009) 4747

2. J.-M. Zhuo, L.-H. Zhao, P.-J. Chia, W.-S. Sim, R. H. Friend, P. K.-H. Ho, “Direct evidence for delocalization of charge carriers at the Fermi level in a doped conducting polymer”, *Phys. Rev. Lett.*, 100 (2008) 186601

Name	Signature	Date

Abstract

π-conjugated organic semiconductor (OSC) is a new class of materials that opens up new applications in a variety of opto(electronic) devices including field-effect transistors, light-emitting diodes and photovoltaics. The unique tailorability and solution processability of these materials lead to a paradigm shift in the design, processing and manufacturing of semiconductor devices. Industry sources are optimistic that the manufacturing capabilities for large-area light-weight organic light-emitting diodes (OLED) for high-efficiency display and lighting applications, solar cells and printed organic thin-film transistor (OTFT) plastic electronic circuits can be put in place. Despite significant recent advances in the development of high-performance materials, a number of fundamental aspects of their semiconductor physics and device chemistry remain to be clarified, including the nature of the charge carriers and interactions between the semiconductor and the environment. These issues determine their characteristics, such as their charge-carrier mobility and stability, which underpin technological applications. Among polymer OSCs, the regioregular poly(3-hexylthiophene) (rr-P3HT) and poly[2,5-bis(3-tetradecylthiophen-2-yl)thieno(3,2-*b*)thiophene] (PBTTT) are the two most important models of a semicrystalline π-stacked OSC with reasonably high field-effect carrier mobility that have been widely studied in both organic field-effect transistor (OFET) and photovoltaic (PV) device applications. This thesis seeks to understand several factors that influence nature of the charge carriers and their transport in these thiophene-based OSCs.

In chapter 1, a brief introduction to several fundamental OSC topics relevant to this thesis is given. This includes a short description of rr-P3HT and PBTTT, and the general mechanism and electrical characteristics of an organic field-effect transistor (OFET). Then a brief review of the known

ambient stability of these materials, and of the known influence of film morphology and gate dielectric interface on device characteristics is given. Finally the nature of charge carriers in OSCs is briefly described followed by a short review on charge modulation spectroscopy (CMS).

In chapter 2, a new reversible photo-induced doping mechanism of thiophene-based OSC involving sorbed moisture uncovered by sensitive Fourier-transform infrared spectrometry is described. This mechanism explains the degradation of the *on – off* ratio when these FETs are exposed to the ambient. The higher resilience of PBTTT compared to rr-P3HT FETs to this doping mechanism is shown to be largely kinetic in origin. The electrical characteristics of rr-P3HT and PBTTT FETs were measured with progressive ambient exposure with and without light. *In-situ* Fourier-transform infrared spectroscopy (FTIR) was used to probe the initial stages of the evolution of the films and correlated to the changes in their electrical characteristics. The photo-doping pathway involving electron transfer from the OSC to the dissolved H_2O was identified from the increase in the intensities of the electronic and vibrational transitions of the polarons, and vibrations related to the hydroxide counter-ions.

In chapter 3, the development of an efficient interferogram-modulated Fourier-transform charge modulation spectroscopy (FT-CMS) technique to collect the infrared spectra of charge carriers in FET devices is described. This technique is an improvement over the conventional *on-off* method because it allows both the in-phase and out-of-phase spectra to be efficiently collected away from zero frequency. As demonstration of a first application, the IR spectrum of the hole carriers in poly(3,4-ethylenedioxythiophene)–poly(styrenesulfonic acid) (PEDT:PSSH) at its Fermi level (E_f) has been collected. The spectrum reveals evidence that these holes at the E_f are surprisingly more delocalized than in the bulk of this degenerately *p*-doped disordered material.

In chapter 4, evidence for the formation of a transition layer with an unfavorable lying-down orientation of the polymer OSC at the dielectric interface and charge-carrier trapping in this layer depending on molecular interactions with the dielectric surface is described. The significance of this finding is that the bulk organization of the polymer does not extend to the frontier layer at the interface where the charge-transport occurs, despite widespread assumptions in the literature. The self-consistent picture that emerges from ultrathin atomic-force microscopy (AFM), near-edge X-ray absorption fine structure spectroscopy (NEXFAS), UV-Vis spectroscopy and charge-modulated spectroscopy in both infrared and optical spectral regions, and detailed variable temperature and variable carrier-density μ_{FET}, using rr-P3HT as model polymer OSC, and various 200 nm-thick SiO_2 substrates with well-defined 1 – 3 nm-thick monolayers as model dielectric surfaces in bottom-gate FETs explains how dielectric surfaces can so markedly influence the μ_{FET} of the charge carriers even amongst films prepared under identical conditions.

Table of Contents

List of Figure

Chapter 1. Introduction

1.1 Organic semiconductors

The first studies of organic semiconductors date back to the early 20th century and the scientific research in organic electronics has since witnessed extraordinary growth and garnered significant industrial interest for the past few decades. Intensive research in organic electronics driven by the prospect of low cost fabrication, low temperature processing techniques and structural flexibility in contrast to conventional inorganic semiconductors-based technology was spurred on when Alan J. Heeger, Alan G. MacDiarmid and Hideki Sirakawa were jointly awarded the Nobel Prize in Chemistry in the year 2000 for "the discovery and development of conductive polymers".[1] To date, the most advanced organic electronic systems already available commercially are thin displays based on organic light-emitting devices (OLEDs)[2], notably in the displays of mobile electronic appliances. Significant progress is also made in the realization of thin film transistors in which performance is comparable to that of vacuum-deposited amorphous silicon (a-Si) where field-effect mobilities is between 0.5 – 1 $cm^2V^{-1}s^{-1}$, and organic photovoltaic (OPV) cells[3] that make low-cost solar energy generation possible. Other demonstrations as potential candidates of organic-based electronics include chemical sensors[4] and RFID tags which aim to replace conventional barcodes.

Organic semiconductors are carbon-rich compounds with semiconducting properties. Of the various types of π-electron system, conjugated polymeric semiconductors have been at the centre-stage of research and development for the last decade. Short chain oligomers or small molecules are usually deposited by vacuum sublimation which is disadvantaged in terms of cost and large-area fabrication. Polymers on the other hand are solution-processable and thus can be deposited via a variety of coating methods such as simple spin-coating, drop-casting or inkjet-printing with which large-area fabrication on flexible plastic sheets is possible. These polymers are long-chain molecules, typically made up of an indeterminate number of aromatic monomer repeating units coupled together where the chain consists of alternating single (σ-bonds) and double bonds (π-bonds), termed conjugation (illustrated in Figure 1.1). The π orbital conjugation is extended along the length of the polymer chain and electrical conduction in these compounds is made possible with the help of delocalized π-electrons. The filled π-orbitals form the valence band while the empty π^*-orbitals form the conduction band. The presence of a small but non-zero energy gap between the highest occupied molecular orbital (HOMO) and the lowest unoccupied molecular orbital (LUMO) results in a semiconducting nature instead of a metallic conduction. The extent of delocalization of π-electrons determines the size of this energy gap. The structures of the polymers can be tailored to optimize a desired property such as high charge mobility or luminescent properties via tuning the energy gap in these materials.

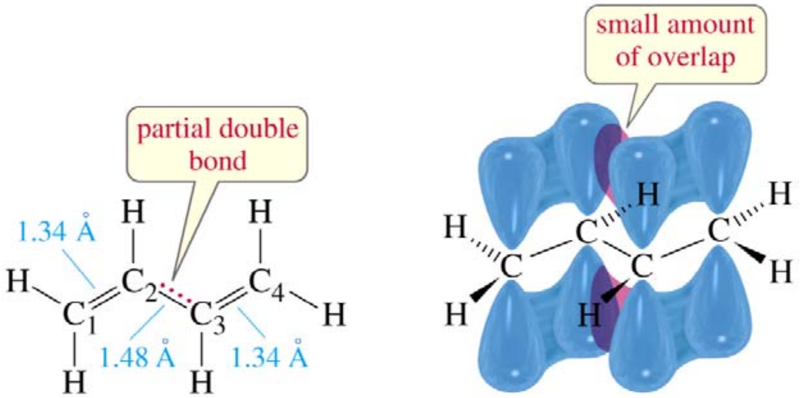

Figure 1.1 Illustration of π-conjugation in 1,3-butadiene. The pure p_z orbitals of two adjacent carbon atoms overlap to form π orbitals where electrons are delocalized over the entire molecule.

1.1.1 Poly(3-alkylthiophene)

Of all conjugated polymers, thiophene-based polymers have exhibited one of the highest charge carrier mobilities from OFETs fabricated by spin-casting. Poly(3-alkythiophenes) were among the first polymers to exhibit high field-effect mobilities[5] of up to 0.1 cm^{2}V^{-1}s^{-1},[6] and regio-regular poly(3-hexylthiophene) (rr-P3HT)[7,8] has emerged as one of the most widely studied polymer for FETs and PV applications. The observations based on this model system have provided critical guidance for the chemical design of new high-performance polymers that can supersede its performance in FETs.

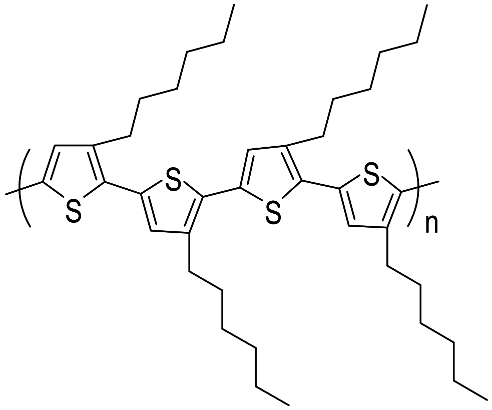

Figure 1.2 Chemical structure of regioregular poly(3-hexylthiophene) (rr-P3HT).

The thiophene units in P3ATs are coupled together at the second and fifth positions and adopt a coplanar conformation, providing a template for achieving highly crystalline thin-film microstructure while the alkyl chains are attached in a head-to-tail arrangement as shown in Figure 1.2. An extended delocalized electronic orbital system is formed where conjugation extends through the electron-rich thiophene rings. Regioregular P3HT packs such that the backbones in the ordered regions are π-stacked in lamellar sheets separated by their side chains[9] as shown in Figure 1.3. The surface morphology of rr-P3HT films is typically nodular (see Figure 1.4) but it can also exhibit whisker (fibrillar) morphology (as illustrated in Figure 1.5) with variations in its molecular weight and processing conditions.

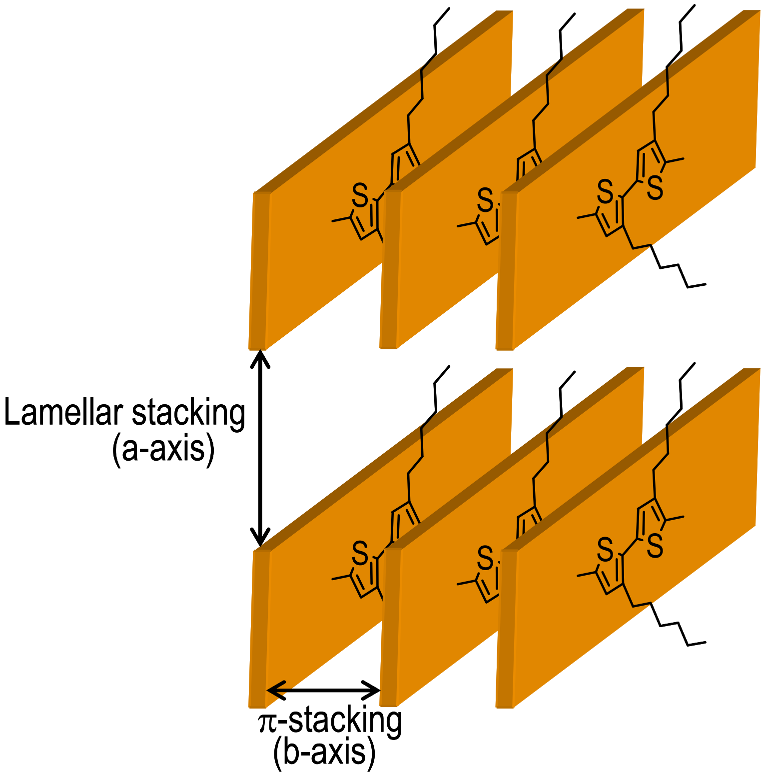

Figure 1.3 Schematic of the molecular packing of regioregular P3HT. The planar conjugated backbones are cofacially stacked along the b-axis while the alkyl side chains are separated along the a-axis.

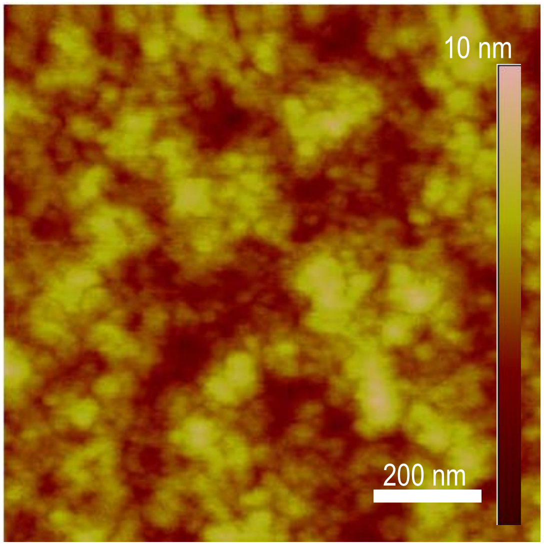

Figure 1.4 Atomic force microscopy (AFM) image of a 50 nm-thick rr-P3HT film spun from chlorobenzene on hexamethyldisilazane (HMDS)-treated SiO_2/Si substrate.

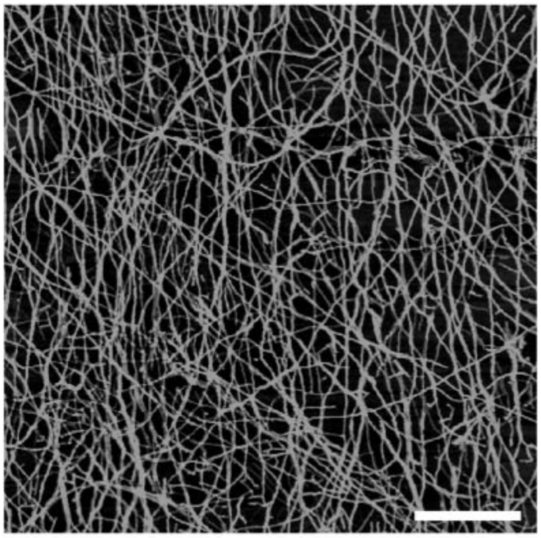

Figure 1.5 AFM image of P3HT nanofibers spincoated on SiO_2/Si substrate using a solvent mixture of anisole/ chloroform (4:1 vol. %).[10] Scan size is 5 x 5 μm.

Various studies using X-ray diffraction and grazing incidence X-ray scattering have shown that rr-P3HT films are microcrystalline where well-ordered small crystalline domains are embedded in a largely amorphous disordered matrix.[11,12] The microstructure and hence performance of P3HT-based OFET depends very sensitively on the degree of head-to-tail regioregularity[5,6] , molecular weight[13-17] among other processing factors such as boiling point of solvent[5,18] used, interfacial treatment[19] and deposition method[5,20-22].

Chang *et* al.[18] demonstrated an enhancement in the μ_{FET} by spin-coating rr-P3HT of a fixed molecular weight from high boiling point solvents. It was explained that the high boiling point solvent allows more time for crystallization to occur during the spin-coating process by evaporating slowly hence improving the degree of microcrystalline order. This is similar to the effect of increased drying time in drop-casting method where large morphological difference and device performance is seen when compared to the spin-coated film. Kline *et* al.[15] found that μ_{FET} can vary by as much as four orders of magnitude when the molecular weight is increased from 3.2 kD to 36.5 kD. The surface morphology in the film changes from whisker-form to nodular-form in low and high molecular rr-P3HT respectively. They attributed this observation to the substantial effect of the molecular weight on way rr-P3HT chains pack. Chang *et* al.[17] reported similar dependence of μ_{FET} on the molecular weight which was explained by fewer defects due to folding in the lamellar, leading to a longer conjugation length and less perturbed interchain packing in longer chains. This reduces the transport dependence on thermally activated hopping of charges between localized segments of chains hence increasing the μ_{FET}.

1.1.2 Poly(bithiophene-*alt*-thienothiophene)

In an effort to improve on intermolecular organization of the conventional thiophene-based polymers, a family of polythiophene derivatives[23,24] has been designed in which thienothiophene copolymers are incorporated. Poly[2,5-bis(3-tetradecylthiophen-2-yl)thieno(3,2-*b*)thiophene] (PBTTT) (see Figure 1.6 for chemical structure), a recently synthesized polymer made up of an alternating copolymer of thieno[3,2-*b*]thiophene and 4,4-dialkyl 2,2-bithiophene monomer units, has been reported to exhibit a higher mobility than the benchmark comparison of P3HT[24]. As a result of incorporating unsubstituted thieno[3,2-*b*]thiophene units, the number of alkyl side chains is reduced which lowers the electron density in the conjugation network and increases the chain stiffness.

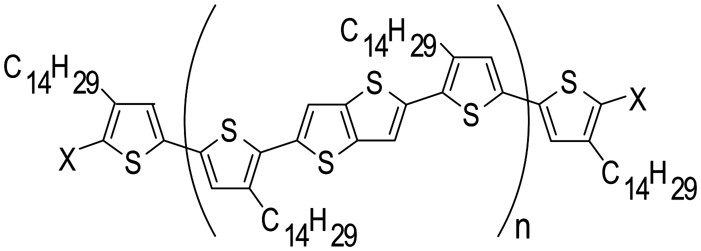

Figure 1.6 Chemical structure of poly[2,5-bis(3-tetradecylthiophen-2-yl)thieno(3,2-*b*)thiophene] (PBTTT).

PBTTT is known to exhibit unusually well-oriented macroscopic lamellar order in which the polymer chains in their chain-extended conformation are π-stacked parallel to the film plane.[24] The lateral extent of this π-stacking can be as large as a few hundred nanometers, which gives rise to the large monolayer lamellae observed in the surface morphology of the films (shown in

Figure 1.7). It is widely believed that the ordered domains manifested in these large terraces contributed to its high μ_{FET}.[24,25]

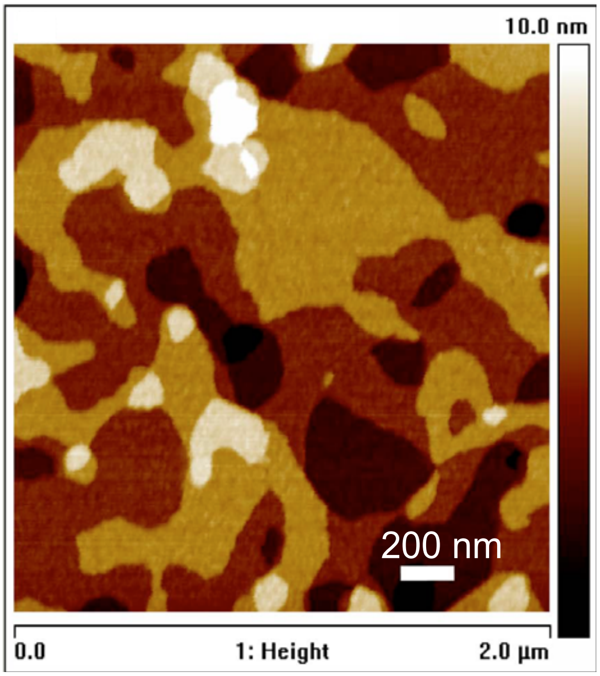

Figure 1.7 AFM image of thin PBTTT film (approximately 20 nm) heated to the liquid-crystal regime.[25]

1.2 Organic field-effect transistors (OFETs)

The principle of the field-effect transistor (FET) was first proposed by Lilienfeld in 1930[26] but it was not until the 1980s where organic field-effect transistors (OFETs) were described[27,28] and being recognized as potential component in electronic devices. It is a three-terminal device consisting of a gate electrode covered by a dielectric insulator layer and semiconducting film that is contacted by source and drain electrodes. Two externally controlled biases are applied for current manipulation in the device. A voltage is applied at the gate electrode (V_g) which accumulates charge carriers at the semiconductor-dielectric interface, forming a channel between the source and drain electrode. These charge carriers then move across the channel when a bias is applied between the source-drain electrodes (V_d). The conductance in the semiconducting channel is modulated by the voltage applied to the gate electrode at a fixed V_d. This control feature allows one to amplify small ac signals or to switch the device from an *on* state to an *off* state and back. These two operations, amplification and switching, are the basis of a host of electronic functions. There are a few variations in FET device configurations, however only one (a bottom- gate, bottom- contact geometry as shown in Figure 1.8) of these is adopted for the purpose of this thesis for consistency.

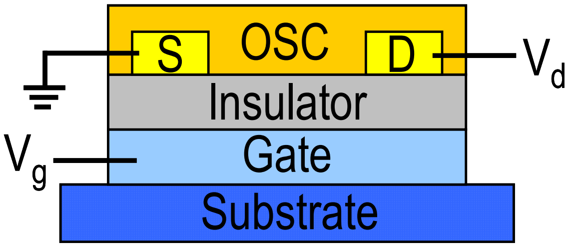

Figure 1.8 Schematic of a bottom-gate, bottom-contact FET where S and D are the source and drain electrode respectively.

Electrical characteristics and extraction of field-effect mobility

An important parameter used to quantify FET performance is the charge carrier mobility, denoted as μ_{FET}. It is a material parameter to quantify the ease with which the accumulated charge can move under the influence of an electric field. The typical current- voltage (*I-V*) characteristics of a *p*-type polymeric FET is shown Figure 1.8. At low V_d where $|V_d| < |V_g - V_{th}|$, the drain current (I_d) increases linearly with V_d (linear regime) and μ_{FET} can be determined from the following equation:

$$\mu_{FET} = \frac{I_d L}{WC_i V_d (V_g - V_{th})}$$

Where L is the channel length, W is the channel width, C_i is the capacitance per unit area of the dielectric layer and V_{th} is the threshold voltage.

When $|V_d| > |V_g - V_{th}|$, I_d tends to saturate (saturation regime) due to the pinch- off at the accumulation layer and the μ_{FET} can be determined from the following equation:

$$\mu_{FET} = \frac{2I_d L}{WC_i (V_g - V_{th})^2}$$

where the μ_{FET} can be extracted from a plot of $\sqrt{I_d}$ against V_g.

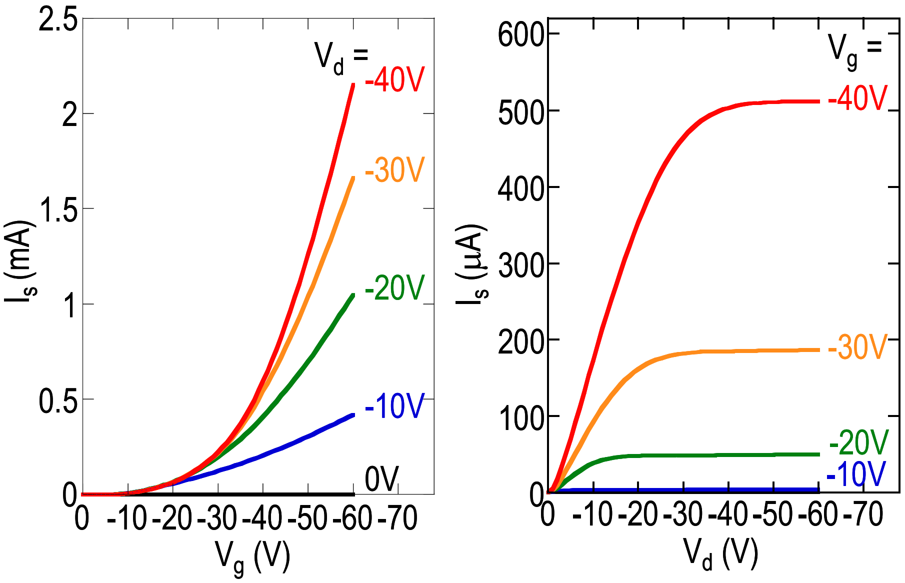

Figure 1.9 Typical current- voltage characteristics of an rr-P3HT based bottom- gate, bottom- contact FET. Left and right panel shows the transfer and output characteristics respectively.

1.2.1 Importance of film morphology

The performance of polymeric FETs is approximately one order of magnitude lower than that of small molecules. This can be understood in terms of the disorder present in thin films of solution-processed polymeric semiconductors as compared to evaporated small molecules that manifest better ordering. Given that polymer chain do not span the entire length of a transistor channel, μ_{FET} is therefore limited by the interchain transport of charge carriers instead of the relatively fast intrachain transport in the absence of backbone imperfections. The morphology of the polymer semiconductor film thus affects the transport on longer length scales. Furthermore, the disorder present in the film causes a broadening in the density-of-states (DOS) in which theoretical studies have shown that charge carriers need to hop up to an effective transport level within the DOS.[29]

The film microstructures of polymer films are often categorized into either disordered or polycrystalline systems. A disordered system is characterized by the absence of any macroscopic arrangement and therefore is not expected to exhibit high μ_{FET} due to the presence of numerous trapping sites that can severely disrupt efficient charge transport along the transistor channel. The presence of crystalline layers in polycrystalline systems facilitates interchain charge transfer as a result of better molecular orbital overlap between neighbouring polymer chains and hence higher μ_{FET} are generally expected in these systems. However, these ordered domains in polycrystalline systems are separated by disordered regions, commonly termed grain boundaries which hamper effective charge transport between ordered domains.

Morphology in polymer films can be controlled by a variety of methods. One way is by engineering the chemical structure of the organic semiconductor such that the polymer chains can, and prefer to form close π-stacking and hence promoting molecular self-assembly. Other methods include the use of various processing conditions and deposition techniques as discussed earlier using rr-P3HT as a model system.

1.2.2 Gate dielectric

The performance of a FET depends critically on the gate dielectric layer since the μ_{FET} is essentially a characterization parameter of the charge carriers in the polymer semiconductor film next to the dielectric layer. Ideally, the gate dielectric layer should be trap-free, has low gate leakage and a high capacitance so that a considerable amount of charges can be accumulated when the FET is turned *on*. The gate dielectric also plays an important role in influencing the molecular ordering or morphology of the organic semiconductor and hence device performance.

Heavily doped silicon wafers and silicon oxide are traditionally used as the gate and dielectric layer respectively in OFETs because of their availability, surface smoothness and a decent dielectric breakdown field of approximately 10 $MVcm^{-1}$. A substantial amount of research has been done in understanding the impact of surface modification of SiO_2 in morphology of the polymer film and charge transport at the dielectric- semiconductor interface. Known effects of the dielectric surface modification include surface roughness,[28-31] dielectric polarization,[30,31] surface energy[29-32] variation and polymer chains alignment through direct chemical interactions.[32] However the exact role of the dielectric surface treatments is still not entirely clear and may be a combination of several effects which can vary in different organic semiconductor systems. Increased roughness can lead to valleys which may act as charge carrier traps in the channel, inhibit the growth of uniform large crystals domains and affect the nucleation density in polycrystalline materials. For example, Knipp *et* al.[33] reported a reduction in the mobility in pentacene films when surfaces exhibit roughness greater than 3–5 Ǻ.

To offer the freedom of fabricating top-gate transistors where deposition of inorganic dielectrics is difficult and expensive and to reduce operational voltages, substantial amount of work has been initiated to develop organic dielectrics. It has been reported by Veres *et* al.[34] that non-polar (low-k) organic insulators consistently perform better in both top-gate and bottom-gate devices which was attributed to the reduced energetic disorder at the interface that causes the broadening of density of states.

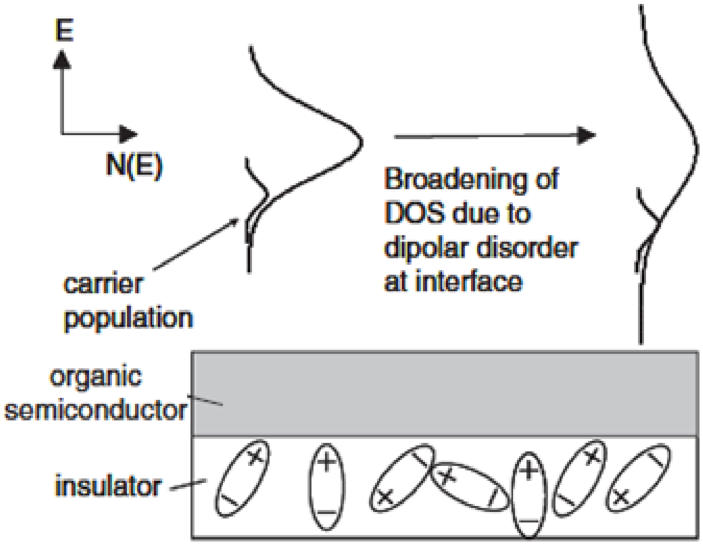

Figure 1.10 Increase in the spread of DOS in the semiconductor at the interface with the dielectric due to local polarization.[34]

1.2.3 Ambient stability of OFETs

The stability of OFETs associated with their shelf life and operation lifetime in the ambient is another important consideration. Similar to numerous other conjugated macromolecules, polythiophenes are known to be susceptible to oxidative doping in the ambient. The effect of degradation is often manifested as a shift to more-positive threshold voltages in *p*-type FETs and higher *off* currents, hence a lower *on*/*off* ratio. However applications such as organic thin-film transistors (TFTs) in display backplanes require a high on/off ratio. An *off* current also contributes an ohmic component to the solar cell and reduces the open-circuit voltage. Understanding the degradation processes is therefore paramount to improve the stability, both during the fabrication and operation of OFETs, PV cells and OLEDs that integrate such polymers. The development of air-stable semiconductors has thereafter been actively investigated. This will negate the need for encapsulation and hence minimizing the cost involved in commercial realization of these technologies originally intended for low-cost and high-volume applications.

It is widely accepted that atmospheric oxygen[35,36] and moisture[37-40] in the ambient predominantly impacts the performance stability of organic semiconductors. Hoshino *et* al.[40] reported at least an order of magnitude increase in the *off*' current in rr-P3HT-based transistors after a few minutes of exposure to a moisturized nitrogen gas. In the presence of intense light, extensive degradation occurs and distinct changes in the chemical structure of polythiophene where a new vibration feature due to formation of carbonyl groups is observed.[41] Abdou *et* al. attributed the primary process leading to the degradation of polythiophene polymers to a photosensitized reaction with singlet oxygen.[42] The Diels-Alder addition reaction of singlet oxygen with the thienyl diene conjugated system leads to the elimination of the thienyl double bonds and formation of carbonyl functional groups.

The poor air stability of rr-P3HT towards oxidative doping has been frequently attributed to its small ionization potential (IP). Hence there have been studies to develop new polymers with a larger ionization potential through chemical structural designs, to improve the air stability.[23,43] The HOMO energy level is modified by controlling the extent of conjugation and electron density in the thiophene backbone. Based on the same OSC system, Majewski *et* al.[44] reported the influence of processing conditions on the stability of rr-P3HT-based transistors where higher stability is correlated to high crystallinity in the film achieved by processing from a high boiling point solvent and substrate surface modification with SAMs. It was interpreted that an ordered and tighter packing of rr-P3HT chains render the diffusion of atmospheric oxygen and water molecules into the film more difficult, hence minimizing the doping of the polymer at the semiconductor-insulator interface.

1.3 Nature of charge carriers

The intrinsic motion of charge carriers within organic semiconductors is of particular interest as it strongly impacts the mobility and hence electrical performance of FETs. However, the physics of charge transport is still a subject of active investigation where the electronic structure of conjugated polymeric semiconductors is a complex interplay between the π-electron delocalization along the polymer backbone, existence of disorder in the solution-processed thin films and electron-phonon coupling. When a charge is introduced into the polymer chain, it causes a distortion in the chain and a polaron is formed.

For example, in the case of a *p*-type polymeric system, the removal of an electron creates a free radical and a positive charge. The radical cation is then coupled with a local rearrangement in the bonds and a quinoid-like bond sequence is formed from the initial benzenoid-like sequence and because of the higher stability of the benzenoid-like sequence, the lattice distortions are limited. Figure 1.11 illustrates the transition from a benzenoid to quinoid-like structure in a polythiophene chain. The charges that are introduced into the polymer interact with certain molecular vibrations as a result of strong electron-phonon coupling and a finite conjugation length due to defects and disorder inherent in the polymer film. The formation of a charge with a free radical accompanied by a local lattice distortion is known as a polaron.

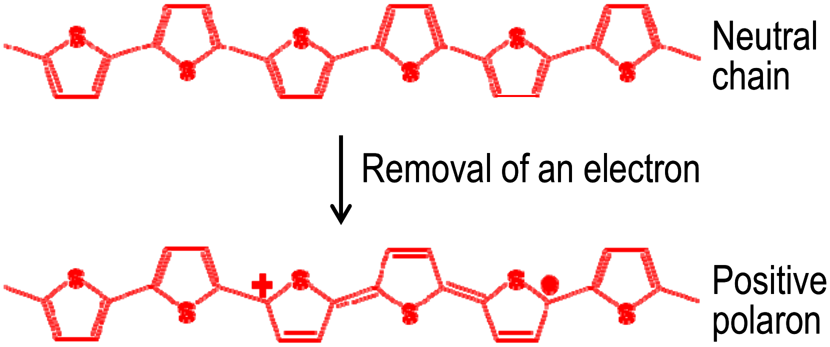

Figure 1.11 Formation of a polaron where a transition from a benzenoid-like sequence in the neutral polythiophene chain to a quinoid-like bond sequence occurs.

In a hypothetical and infinitely straight neutral polymer chain, the highest occupied molecular orbital (HOMO) and lowest unoccupied molecular orbitals (LUMO) are fully delocalized along the chain. In the formation of a polaron, new localized energy states arise between the HOMO and LUMO level of the neutral polymer as the result of structural and electronic relaxation upon self-trapping of the charge. With the absorption of a photon of an appropriate energy, the polaron can be freed from the potential well that self-traps it, thus giving rise to characteristic new optical transitions within the band gap of the neutral polymer. The energy level diagram illustrating the transitions in a simple isolated 1-dimensional and defects-free polymer chain is shown in Figure 1.12.

Self-trapped polaron (P^+) and bipolaron (BP^{2+}) states have been well-established respectively for the singly- and doubly-charged oligomers in the solution state.[45] However the description of these states is still unclear in longer chains[46] and particularly in the solid state.

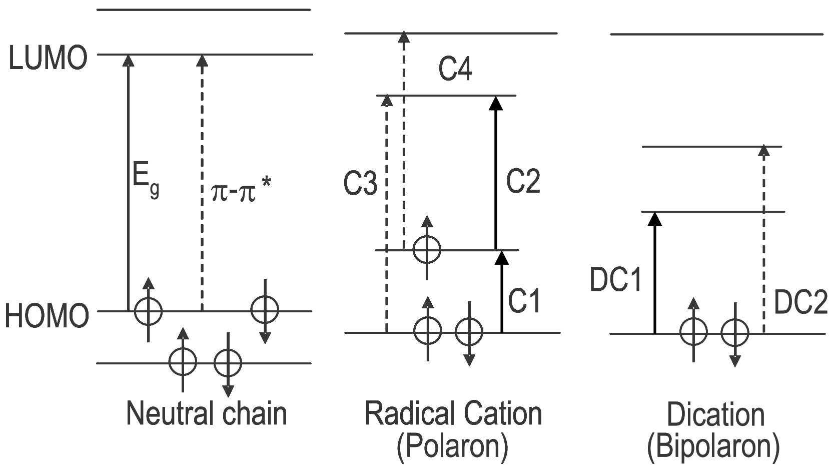

Figure 1.12 Energy level diagram of a neutral polymer and polaronic absorptions in a simple isolated chain model of radical cations and dications. The C3, C4 and DC2 transitions are usually forbidden due to symmetry considerations.

During the operation of a FET where the accumulation layer thickness is only a few monolayers- thick, the charge carrier concentration is small compared to the total amount of material in a film of semiconducting polymer. Therefore a stable and sensitive optical method is required for the detection of the spectroscopic changes in the absorbance of the material when charges are introduced, giving insights to the charge transport. Several techniques have been used to study charge carriers in organic semiconductors which include chemical doping, photo-induced absorption and charge modulation spectroscopy among which the latter will be discussed further in this thesis.

1.4 Charge carriers characterization: Charge modulation spectroscopy (CMS)

Charge modulation spectroscopy (CMS) is an electro-optical spectroscopic technique that allows the properties of charge carriers present in the conducting channels of operational FETs and other device structures such as metal-insulator-semiconductor (MIS) devices to be studied *in situ* via their spectroscopic signatures. It has an advantage over the conventional chemical doping technique in which charges are introduced into the polymer by doping it with an oxidizing or reducing agent which removes or adds a known amount of electronic charges from the chains. In this process, counter-ions are also inevitably introduced into the π-conjugated system which complicates the study.

In charge modulation spectroscopy, an oscillating bias is typically applied at the gate and the changes in the optical transmission of the operational FET induced by modulating the carrier concentration in the accumulation layer are detected. The detection of the modulated transmission is often aided by lock-in technique where the signal is singled out from background noise and amplified. This signal is essentially the difference between the peak and trough of the modulated voltage and probes charge carriers that are mobile on the time scale of the modulation. Charge carriers that are trapped on this time scale will not produce a differential signal. This technique will be further discussed in Chapter 3.

Several groups have attempted to use charge modulation spectroscopy in probing the behaviour of charge carriers in organic semiconductors. For example, Ziemelis *et* al.[47] performed CMS on thin films of regio-random P3HT in a MIS structure and assigned the features observed to those of polarons and bipolarons predicted by the 1D model of Fesser, Bishop and Campbell.[48] Harrison *et* al.[49,50] performed CMS experiments on a range of polycrystalline oligothiophenes in which they observed the existence of an aggregated state known as the π-dimer as a result of weak interchain interactions in 6T. Brown *et* al.[51,52] used the technique to study the charge carriers present in the conducting channels of FETs based on rr-P3HT and showed that the CMS spectra of their system is independent of charge density, modulation frequency and temperature and thus suggested the presence of only a single intrinsic charge carrier. The results also suggest that interchain coupling in rr-P3HT is sufficiently strong so that charge carriers cannot be considered to be confined to a single chain and instead spread over several π-stacked chains and exhibit quasi-2D characteristics.

1.5 References

1 <http://nobelprize.org/nobel_prizes/chemistry/laureates/2000/>

2 Burroughes, J. H. *et al.* Light-emitting diodes based on conjugated polymers. *Nature* 347, 539-541 (1990).

3 Liang, Y. *et al.* For the bright future- Bulk heterojunction polymer solar cells with power conversion efficiency of 7.4%. *Adv. Mater.* 22, E135-E138 (2010).

4 Crone, B. *et al.* Electronic sensing of vapors with organic transistors. *Appl. Phys. Lett.* 78, 2229-2231 (2001).

5 Bao, Z., Dodabalapur, A. & Lovinger, A. J. Soluble and processable regioregular poly(3-hexylthiophene) for thin film field-effect transistor applications with high mobility. *Appl. Phys. Lett.* 69, 4108-4110 (1996).

6 Sirringhaus, H. *et al.* Two-dimensional charge transport in self-organized, high-mobility conjugated polymers. *Nature* 401, 685-688 (1999).

7 Chen, T. A. & Rieke, R. D. The first regioregular head-to-tail poly(3-hexylthiophene-2,5-diyl) and a regiorandom isopolymer: Ni vs Pd catalysis of 2(5)-brom-5(2)-(bromozincio)-3-hexylthiophene polymerization. *J. Am. Chem. Soc.* 114, 10087-11088 (1992).

8 Chen, T. A., Wu, X. & Rieke, R. D. Regiocontrolled synthesis of poly(3-alkylthiophenes) mediated by Rieke zinc: their characterisation and solid-state properties. *J. Am. Chem. Soc.* 117, 233-244 (1995).

9 Prosa, T. J., Winokur, M. J., Moulton, J., Smith, P. & Heeger, A. J. X-ray structural studies of poly(3-alkylthiophenes): An example of an inverse comb. *Macromolecules* 25, 4364-4372 (1992).

10 Samitsu, S., Shimomura, T., Heike, S., Hashizume, T. & Ito, K. Effective production of poly(3-hexylthiophene) nanofibers by means of whisker method using anisole solvent: Structure, optical, and electrical properties. *Macromol.* 41, 8000-8010 (2008).

11 Kline, R. J. *et al.* Dependence of regioregular poly(3-hexythiophene) film morphology and field-effect mobility on molecular weight. *Macromol.* 38, 3312-3319 (2005).

12 Zen, A. *et al.* Effect of molecular weight on the structure and crystallinity of poly(3-hexylthiophene). *Macromol.* 39, 2162-2171 (2006).

13 Chang, J.-F. *et al.* Molecular-weight dependence of interchain polaron delocalization and exciton bandwidth in high-mobility conjugated polymers. *Physical Review B* 74, 115318 (2006).

14 Kline, R. J. *et al.* Dependence of regioregular poly(3-hexylthiophene) film morphology and field-effect mobility on molecular weight. *Macromol.* 38, 3312-3319 (2005).

15 Kline, R. J., McGehee, M. D., Kadnikova, E. N., Liu, J. & Fréchet, J. M. J. Controlling the field-effect mobility of regioregular polythiophene by changing the molecular weight. *Adv. Mater.* 15, 1519-1522 (2003).

16 Zen, A. *et al.* Effect of molecular weight and annealing of poly(3-hexylthiophene)s on the performance of organic field-effect transistors. *Adv. Funct. Mater.* 14, 757-764 (2004).

17 Chang, J.-F., Sirringhaus, H., Giles, M., Heeney, M. & McCulloch, I. Relative importance of polaron activation and disorder on charge transport in high-mobility conjugated polymer field-effect transistors. *Phys. Rev. B.* 76, 205204-205201 (2007).

18 Chang, J.-F. *et al.* Enhanced Mobility of Poly(3-hexylthiophene) Transistors by Spin-coating from High-Boiling-Point Solvents. *Chem. Mater.* 16, 4772-4776 (2004).

19 Kline, R. J., McGehee, M. D. & Toney, M. F. High oriented crystals at the buried interface in polythiophene thin-film transistors. *Nat. Mater.* 5, 222-228 (2006).

20 Wong, L. Y. *et al.* Interplay of processing, morphological order, and charge-carrier mobility in polythiophene thin films deposited by different methods: Comparison of spin-cast, drop-cast, and inkjet-printed films. *Langmuir* 26, 15494-15507 (2010).

21 Wang, G., Swensen, J., Moses, D. & Heeger, A. J. Increased mobility from regioregular poly(3-hexylthiophene) field-effect transistors. *J. Appl. Phys.* 93, 6137-6141 (2003).

22 Sirringhaus, H. *et al.* Two-dimensional charge transport in self-organised, high-mobility conjugated polymers. *Nature* 401, 685-688 (1999).

23 Heeney, M. *et al.* Stable polythiophene semiconductors incorporating thieno[2,3-b]thiophene. *J. Am. Chem. Soc.* 127, 1078-1079 (2005).

24 McCulloch, I. *et al.* Liquid-crystalline semiconducting polymers with high charge-carrier mobility. *Nat. Mater.* 5, 328-333 (2006).

25 Kline, R. J. *et al.* Significant dependence of morphology and charge carrier mobility on substrate surface chemistry in high performance polythiophene semiconductor films. *Appl. Phys. Lett.* 90, 062117- 062111-062113 (2007).

26 Lilienfeld, J. E. US Patent 1 745 175. (1930).

27 Koezuka, H., Tsumura, A. & Ando, T. Field-effect transistor with polythiophene thin film. *Synth. Met.* 18, 699-704 (1987).

28 Tsumura, A., Koezuka, H. & Ando, T. Polythiophene field-effect transistor: Its characteristics and operation mechanism. *Synth. Met.* 25, 11-23 (1988).

29 Coehoorn, R., Pasveer, W. F., Bobbert, P. A. & Michels, M. A. J. Charge-carrier concentration dependence of the hopping mobility in organic materials with Gaussian disorder. *Phys. Rev. B* 72, 155206-155201-155220 (2005).

30 Pernstich, K. P. *et al.* Threshold voltage shift in organic field effect transistors by dipole monolayers on the gate insulator. *J. Appl. Phys.* 11, 6431-6438 (2004).

31 Takeya, J. *et al.* Effects of polarized organosilane self-assembled monolayers on organic single-crystal field-effect transistors. *Appl. Phys. Lett.* 85, 5078-5080 (2004).

32 Kim, D. H. *et al.* Enhancement of field-effect mobility due to surface-mediated molecular ordering in regioregular polythiophene thin film transistors. *Adv. Funct. Mater.* 15, 77-82 (2005).

33 Knipp, D., Street, R. A. & Völkel, A. R. Morphology and electronic transport of polycrystalline pentacene thin-film transistors. *Appl. Phys. Lett.* 82, 3907-3909 (2003).

34 Veres, J., Ogier, S. D., Leeming, S. W., Cupertino, D. C. & Khaffaf, S. M. Low-k insulators as the choice of dielectrics in organic field-effect transistors. *Adv. Funct. Mater.* 13, 199-204 (2003).

35 Taylor, D. M., Gomes, H. L., Underhill, A. E., Edge, S. & Clemenson, P. I. Effect of oxygen on the electrical characteristics of field effect transistors formed from electrochemically deposited films of poly(3-methylthiophene). *J. Phys. D: Appl. Phys.* 24, 2032-2038 (1991).

36 Abdou, M. S. A., Orfino, F. P., Son, Y. & Holdcroft, S. Interaction of oxygen with conjugated polymers: charge transfer complex formation with poly(3-alkylthiophenes). *J. Am. Chem. Soc.* 119, 4518-4524 (1997).

37 Li, D. *et al.* Humidity effect on electrical performance of organic thin-film transistors. *Appl. Phys. Lett.* 86, 042105- 042101-042103 (2005).

38 Qiu, Y. *et al.* H2O effect on the stability of organic thin-film field-effect transistors. *Appl. Phys. Lett.* 83, 1644-1646 (2003).

39 Liu, Y., Wu, L., Lai, P. T. & Zuo, Q. Air-stability analysis and improvement of poly(3-hexylthiophene) field-effect transistors. *Semicond. Sci. Technol.* 24, 095013- 095011-095015 (2009).

40 Hoshino, S. *et al.* Influence of moisture on device characteristics of polythiophene-based field-effect transistors. *J. Appl. Phys.* 95, 5088-5093 (2004).

41 Ficker, J. *et al.* Influence of intensive light exposure on polymer field-effect transistors. *Appl. Phys. Lett.* 85, 1377-1379 (2004).

42 Abdou, M. S. A. & Holdcroft, S. Mechanisms of photodegradation of poly(3-alkylthiophenes) in solution. *Macromol.* 26, 2954-2962 (1993).

43 McCulloch, I. *et al.* Influence of molecular design on the field-effect transistor characteristics of terthiophene polymers. *Chem. Mater.* 17, 1381-1385 (2005).

44 Majewski, L. A., Kingsley, J. W., Balocco, C. & Song, A. M. Influence of processing conditions on the stability of poly(3-hexylthiophene)-based field-effect transistors. *Appl. Phys. Lett.* 88, 222108- 222101-222103 (2006).

45 Apperloo, J. J. *et al.* Optical and redox properties of a series of 3,4-ethylenedioxythiophene oligomers. *Chem. Eur. J.* 8, 2384-2396 (2002).

46 van Haare, J. A. E. H. *et al.* Redox states of long oligothiophenes: two polarons on a single chain. *Chem. Eur. J.* 4, 1509-1522 (1998).

47 Ziemelis, K. E. *et al.* Optical spectroscopy of field-induced charge in poly(3-hexyl thienylene) metal-insulator-semiconductor structures: evidence for polarons. *Phys. Rev. Lett.* 66, 2231-2234 (1991).

48 Fesser, K., Bishop, A. R. & Campbell, D. K. Optical absorption from polarons in a model of polyacetylene. *Phys. Rev. B* 27, 4804-4825 (1983).

49 Harrison, M. G., Friend, R. H., Garnier, F. & Yassar, A. The charged excitations in thin films of α-sexithiophene within semi-transparent field-effect devices: investigation by optical spectroscopy of field-induced charge and by photoimpedance spectroscopy. *Synth. Met.* 67, 215-221 (1994).

50 Harrison, M. G., Fichou, D., Garnier, F. & Yassar, A. In situ charge-modulation spectroscopy of oligothiophene field-effect diodes: from sexithiophene towards polythiophene. *Opt. Mater.* 9, 53-58 (1998).

51 Brown, P. J., Sirringhaus, H., Harrison, M., Shkunov, M. & Friend, R. H. Optical spectroscopy of field-induced charge in self-organized high mobility poly(3-hexylthiophene). *Phys. Rev. B* 63, 125204:125201-125211 (2001).

52 Brown, P. J., Sirringhaus, H. & Friend, R. H. Electro-optical characterisation of field effect devices with regioregular poly-hexylthiophene active layers. *Synth. Met.* 101, 557-560 (1999).

Chapter 2. Photo-doping mechanism in polythiophene and poly(bithiophene-*alt*-thienothiophene) organic semiconductor thin films

In this chapter, we describe a photo-doping pathway in thiophene-based organic semiconductors that accounts for the first-stage degradation of their semiconductor characteristics and of their organic field-effect transistors (FETs) when exposed progressively to the ambient. Fourier-transform infrared spectroscopy of two prototypical high-mobility polymer organic semiconductors (OSCs), regioregular poly(3-hexylthiophene) (rr-P3HT) and poly[2,5-bis(3-tetradecylthiophen-2-yl)thieno(3,2-*b*)thiophene] (PBTTT), reveals photoinduced doping involving both oxygen and water dissolved in the polymer matrix when exposed to light.

The equilibrium concentration of water at room temperature and 60% relative humidity in these films is *ca*. 2 x 10^{19} cm^{-3}, primarily as monomers, with a small population of dimers and other clusters. Photo-excitation in room light ultimately generates a polaron density of the order of few 10^{17} cm^{-3}, which is sufficient to degrade the saturation and *on–off* characteristics of organic field-effect transistors, and also the dark current of organic photovoltaics. The dopant anion has been identified primarily to be hydroxide ion species. This process occurs to a smaller extent in wet nitrogen, but even less in dry oxygen, which points to a key role of the dissolved water. The relative stability of PBTTT over rr-P3HT is found to be largely kinetic in origin, attributed to its higher crystallinity (X-ray diffraction crystallinity 27% *vs* 21% in rr-P3HT), and shorter $\pi...\pi$ stacking distance (3.64 Å *vs* 3.78 Å in rr-P3HT) which gives better moisture exclusion from its thiophene backbone.

2.1 Introduction

Understanding the degradation mechanisms of polymer OSC devices is an essential step to develop more robust OSC systems and their devices, whether in light-emitting diodes (LEDs), field-effect transistors (FETs) or photovoltaics (PVs). Despite decades of research, detailed spectroscopic studies have seldom been reported,[1-3] primarily because of considerable challenges in studying changes at the sub-1-mol% of repeat units in thin films. Yet these levels are electronically significant. The typical carrier density during LED operation[4] is *ca*. 1 x 10^{18} cm^{-3}, i.e. about 0.05 mol% of repeat units assuming a unit molecular weight of 300 g mol^{-1} and density of 1.1 g cm^{-3}. For organic FETs, doping at this level can open up a parallel source–drain Ohmic shunt conductance sufficiently to prevent shut *off* and saturation characteristics.[5-8] A simple performance figure-of-merit is the *on–off* ratio, which for small drain voltages V_d and for an *off*-state defined as at V_g = 0 V is given for long-channel FETs by

$$\frac{i_{on}}{i_{off}} = \frac{\mu C_{ox}(V_g - V_{th})}{\sigma d}$$

where μ is carrier mobility, C_{ox} is gate-dielectric capacitance, $(V_g - V_{th})$ is effective gate voltage, σ is shunt conductance and d is film thickness. For $\mu \approx 0.1$ cm^2 V^{-1} s^{-1}, $d \approx 30$ nm and typical values for other parameters, we require $\sigma < 10^{-8}$ S cm^{-1} to give an i_{on} / i_{off} ratio > 10^6. In this case the bulk carrier density n_{bulk} in the OSC cannot be allowed to exceed *ca*. 10^{17}–10^{18} cm^{-3}.[9]

Thiophene-based OSCs are particularly important materials classes for FET and PV applications. Previously it has been proposed variously that O_2[5-7] or moisture[8] is responsible for doping of thiophene-based FETs in ambient air, from the rise in the FET shunt conductance over time. It has been established that pure O_2 can reversibly dope polythiophenes to a small extent from electrical,[10] optical and electron paramagnetic studies.[11] A thermodynamic analysis of the stability of OSCs in contact with various redox couples, e.g. the O_2/OH^-, O_2/HO_2^- and H_2O/OH^-, has been formulated.[12] However the relative importance of these mechanisms in the ambient and the possible role of photoexcitation have yet to be clarified.

rr-P3HT[13,14] and PBTTT[15,16] are important polymer OSC prototypes with high hole mobilities ($\mu \approx 0.01–0.1$ cm^2 V^{-1} s^{-1}). Both have repeating thiophene motifs, similar absorption spectra (π–π^* onset at *ca*. 1.95 eV), nearly similar ionization potentials (I_p, rr-P3HT, 4.55 ± 0.1; PBTTT, 4.7 ± 0.1 eV)[17], yet widely differing storage and operational stabilities. rr-P3HT FETs are highly susceptible to unintentional doping while PBTTT FETs are more robust.[15] PBTTT is also considerably more crystalline.[15,16] During operation in ambient air, however, even PBTTT FETs show a slow performance loss.[18,19] Therefore understanding the molecular mechanisms underpinning these behaviors will provide important insights for rationale design and for back-end encapsulation.

In-situ Fourier-transform infrared spectroscopy (FTIR) measurement on rr-P3HT and PBTTT films with sufficient sensitivity to reveal the emerging doping signature[20,21] in these OSCs at the 10^{17} cm^{-3} level during the initial stages of their interaction with both ambient air and light will be discussed. We point out the role of photoexcitation, and identify the counterion formed to demonstrate a photo-doping pathway that H_2O dissolved in the polymer matrix. At very high photon doses (such as when exposed to the sun), conjugation breaking occurs and carbonyl defects are formed,[3] but such drastic changes do not occur during the early-stage degradation.

2.2 Experimental methods

2.2.1 Fabrication of OFETs

FETs were fabricated in the bottom-gate configuration with hexadimethyldisilazane (HMDS)-treated 200-nm-thick thermal SiO_2 as gate-dielectric, p^{++}-Si as gate, and lithographically-patterned Au source–drain electrodes (channel length L = 10 and 20 μm; channel width w = 2.0 cm). A 50 nm-thick film of rr-P3HT (Aldrich; which was then purified by hydrazine reduction and flash chromatography in-house to reduce unintentional doping to $< 10^{17}$ cm^{-3}) and end-capped PBTTT (synthesized in-house)[19] was spin-cast from chlorobenzene solutions in the glovebox (pO_2, $pH_2O < 1$ ppm). Both rr-P3HT and PBTTT show strong aggregation effects,[19] and this requires care to keep the solution history the same between runs for meaningful comparisons.[22] The films were then annealed in the glovebox for 10 min at 120°C (rr-P3HT) or 150°C (PBTTT) to remove residual solvent, and for PBTTT to achieve liquid-crystal ordering.[15,16,18,19]

2.2.2 Electrical characterization of OFETs

FET characteristics were collected in a nitrogen- purged glovebox using a Keithley 4200 semiconductor parameter analyzer. The electrical characteristics of the pristine devices were first measured in the glovebox before the devices were transferred out of the glovebox and exposed to the various ambient conditions. Measurements were then taken in the glovebox after each exposure condition. Exposure to cleanroom air in the dark was achieved by covering the device sample box with aluminum foil before transferring out of the glovebox.

2.2.3 In-situ FT-IR measurement of thiophene films

Thick films of rr-P3HT (3.1-μm) and PBTTT (7.1-μm) were deposited from chlorobenzene onto HMDS-treated intrinsic Si wafers. The films were annealed at 120°C for 10 min and loaded into the cryostat in the glovebox. Infrared spectroscopy spectra were collected with Nicolet 8700 FT-IR at a resolution of 2 cm^{-1}. The FT-IR spectra were recorded sequentially after each exposure *in-situ* without displacing the sample in the optical path. Exposure to air was achieved by venting to cleanroom air; while exposure to light was achieved by illuminating the sample with the output of a tungsten-halogen lamp[23] via an electromechanical flip mirror.

2.2.4 X-Ray powder diffraction

1 mm-thick rr-P3HT and PBTTT films were drop-cast on Al_2O_3 sample holders from 50 mg mL^{-1} solutions in chlorobenzene in a nitrogen glovebox. The films were then annealed to 150ºC (rr-P3HT) and 160ºC (PBTTT) for 10 min for solvent removal, followed by slow cooling to room temperature to develop maximum crystallinity. Molecular weights are nearly identical (M_n = 17k and 19k respectively). θ–2θ XRD diffractograms were collected with Bruker-AXS D8 Powder X-ray Diffractometer using monochromatized 1.541-Å Cu K_α radiation.

2.3 Results and discussion

2.3.1 The impact of ambient exposure on device characteristics

Regioregular poly(3-hexylthiophene)

Figure 2.1 shows the sequential transfer characteristics for rr-P3HT field-effect transistor (L = 20 μm) when it was exposed stepwise to the conditions as indicated. Even before exposure, pristine rr-P3HT FETs requires V_g = +8 V to switch *off* due to a weak doping by residual chlorobenzene solvent. The FETs are stable over prolonged periods in the glovebox, and even in cleanroom air (temperature 22ºC, relative humidity 60%) provided light is rigorously excluded (curves (i)–(iv)). The diffusion coefficient D for O_2 in regio-irregular P3HT has been found to be 1.2×10^{-8} cm^2 s^{-1},[11] and so is expected to be of the order of 1×10^{-8} cm^2 s^{-1} for these thiophene-based materials. The D for H_2O is likely to be even larger.[24] Thus the diffusion time given by $t_D = d^2/(2D)$ is of the order of 1 ms in these thin films, and equilibrium with ambient gases reached instantaneously in these experiments.

When rr-P3HT FETs are exposed also to orange-filtered cleanroom ambient light even for a brief 5 min (Figure 2.1, curves (v) and (vi)) at an intensity that gives an absorbed photon flux n_{ab} of 9×10^{13} ph s^{-1} cm^{-2}, the V_g required to turn *off* the FET shifts to +16 V for small V_d. This larger V_g is required to deplete an increased n_{bulk}. It is partially reversible by re-equilibrating in the glovebox for 1 wk (curve (vii)). After a longer light exposure of 1 h, the characteristics appear to reach a limiting state (curve (viii)) with the required V_g to turn *off* shifted to +35 V. From this we estimated $n_{bulk} \approx 6.1 \times 10^{17}$ cm^{-3}, and $\sigma \approx 2.5 \times 10^{-5}$ S cm^{-1}.

Poly[2,5-bis(3-tetradecylthiophen-2-yl)thieno(3,2-b)thiophene]

The FET transfer characteristics of PBTTT acquired after different exposure conditions is shown in Figure 2.2. Before exposure, pristine PBTTT FETs can be switched *off* fully even at V_g = 0 V, consistent with its lower doping propensity.[19] The PBTTT FETs, similar to the rr-P3HT FETs, are stable over prolonged periods in the glovebox and in cleanroom air when light is excluded (curves (i)– (iv)). However in contrast to the rr-P3HT FETs, the characteristics of PBTTT FETs changed only after longer exposures of > 15 min to light corresponding to the same n_{ab} (Figure 2.2, curves (v) and (vi)). These devices showed complete healing when re-equilibrated in the glovebox for 1 wk (curve (vii)). After prolonged light exposure of 1 d, the characteristics too reach a limiting state (curve (viii)) with the V_g for *off*-state shifted to *ca.* +14 V. This corresponds to $n_{bulk} \approx 2.4 \times 10^{17}$ cm^{-3}, which is nearly half of that of rr-P3HT. Similar results were found for L = 10 μm devices. Thus both rr-P3HT and PBTTT are susceptible to doping to similar extents as a result of interaction with both ambient air and light.

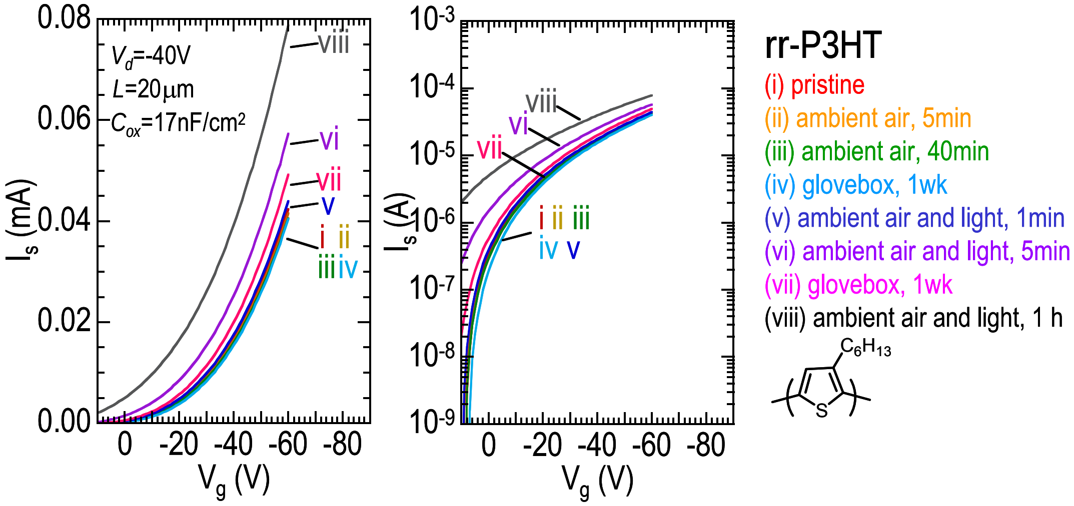

Figure 2.1 FET transfer characteristics of rr-P3HT sequentially acquired after different exposure conditions. Left and middle panels give the linear and log plots respectively; right panel lists the exposure conditions. “Ambient air” is cleanroom air (22ºC, RH 60%); “light” corresponds to an absorbed photon flux intensity of 9 x 10^{13} ph s^{-1} cm^{-2}; h = hour, d = day, wk = week.

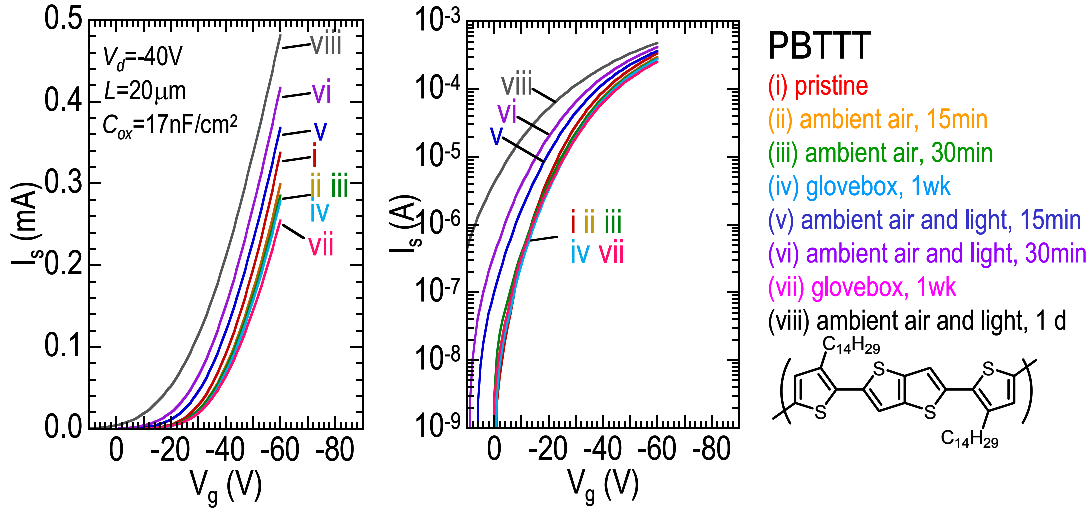

Figure 2.2 FET transfer characteristics of PBTTT sequentially acquired after different exposure conditions. Left and middle panels give the linear and log plots respectively. The set of exposure conditions for the device is listed on the right panel. “Ambient air” and “light” are as defined in Figure 2.1.

2.3.2 Spectroscopic changes in the semiconductor films

To identify the doping and other molecular changes, we acquired the FTIR spectra of thick films of these OSCs (3.1-μm rr-P3HT, 7.1-μm PBTTT) deposited from chlorobenzene onto HMDS-treated intrinsic Si wafers. Thick films were used to improve detectability and to suppress interference fringes, while keeping $t_D < 1$ min. The sharp molecular spectra of gas-phase H_2O and CO_2 present in the ambient were digitally removed for clarity.

The FTIR spectrum of the polymer film in vacuum is shown in Figure 2.3(a) and Figure 2.4(a) respectively for rr-P3HT and PBTTT. The difference spectra after different exposures were obtained by subtraction and shown in Figure 2.3(b) and Figure 2.4(b) respectively for these two OSCs. These spectra therefore track the cumulative effect of both air and light on the polymers. Another set of difference spectra were obtained by subtracting the film equilibrated with the ambient but in the dark, and these are shown in Figure 2.5 and Figure 2.6 for the rr-P3HT and PBTTT respectively. These track the effect of light alone.

Distinct spectral changes occurred in both OSCs upon exposure to the ambient even in the dark. Broad absorption bands at 3728 and 3626 cm^{-1} characteristic of molecular H_2O (ν_{as} and ν_s OH respectively) embedded in a matrix[25] were found. Hydrogen-bonded H_2O dimers at 3702 and 3597 cm^{-1},[25-27] and trimers at 3677 and 3484 cm^{-1}, were also found, but not larger H_2O clusters which are expected at 3200–3600 cm^{-1}.[25-27] The 3820 cm^{-1} band is a combination of νOH and intermolecular libration,[25] which could yield information on the molecular environment of these H_2O molecules.

The integrated νOH absorption intensities normalized to film thicknesses turn out to be nearly identical for these two OSCs. We estimated in PBTTT, sorbed H_2O = 1.7±0.2 x 10^{19} cm^{-3}, which corresponds to 0.4 mol% of thiophene rings (the thienothiophene unit being counted as two rings); and in P3HT, ≈ 2.0±0.2 x 10^{19} cm^{-3} (i.e., 0.5 mol% of rings), using an integrated absorption cross-section over 3200–3800 cm^{-1} of 1.4 x 10^{-16} cm per molecule, as in liquid H_2O.[28] These equilibrium concentrations of H_2O in ambient air at RH = 60% are thus about a factor of ten larger than that of pure O_2 in regio-irregular P3HT (1.2 x 10^{18} cm^{-3}).[11] CO_2 is also readily sorbed as evidenced by the broad bands at 2340 and 677 cm^{-1} (ν_{as} and δ CO_2 respectively).

These features persist throughout the experiment (spectra (ii)–(v)) confirming equilibrium was attained. Rr-P3HT but not PBTTT also showed changes in the polymer vibrations: 2958, 2920, 2858 (all three are νCH_2 alkyl), 1510 (backbone), 1456 (δCH), 819 and 725 cm^{-1} (both δ_{oop} ring-CH), at the 1–2% level, which we attribute to a re-orientation or a small frequency shift due to intercalation of H_2O, O_2 and/or CO_2. Thus the thiophene backbone of rr-P3HT is more perturbed by sorption of these molecules than of PBTTT.

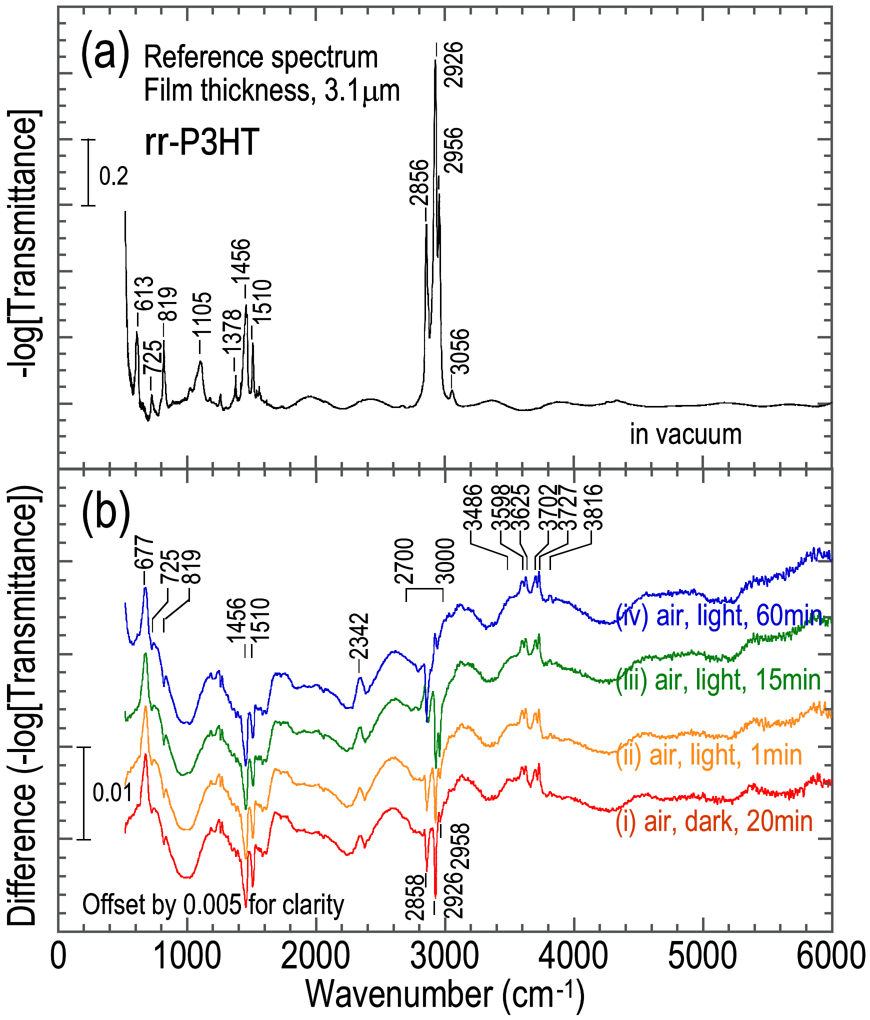

Figure 2.3 FTIR spectra of rr-P3HT film acquired sequentially after different *in-situ* exposure to cleanroom air. (a) Reference spectrum of film in vacuum. (b) Difference spectra obtained by subtracting the spectrum of the film in vacuum, offset for clarity. Spectra of gas-phase H_2O and CO_2 have also been removed for clarity. "Air" is cleanroom air (22ºC, RH 60%), and "light" corresponds to an absorbed photon flux intensity of 2.0 x 10^{15} ph s^{-1} cm^{-2}.

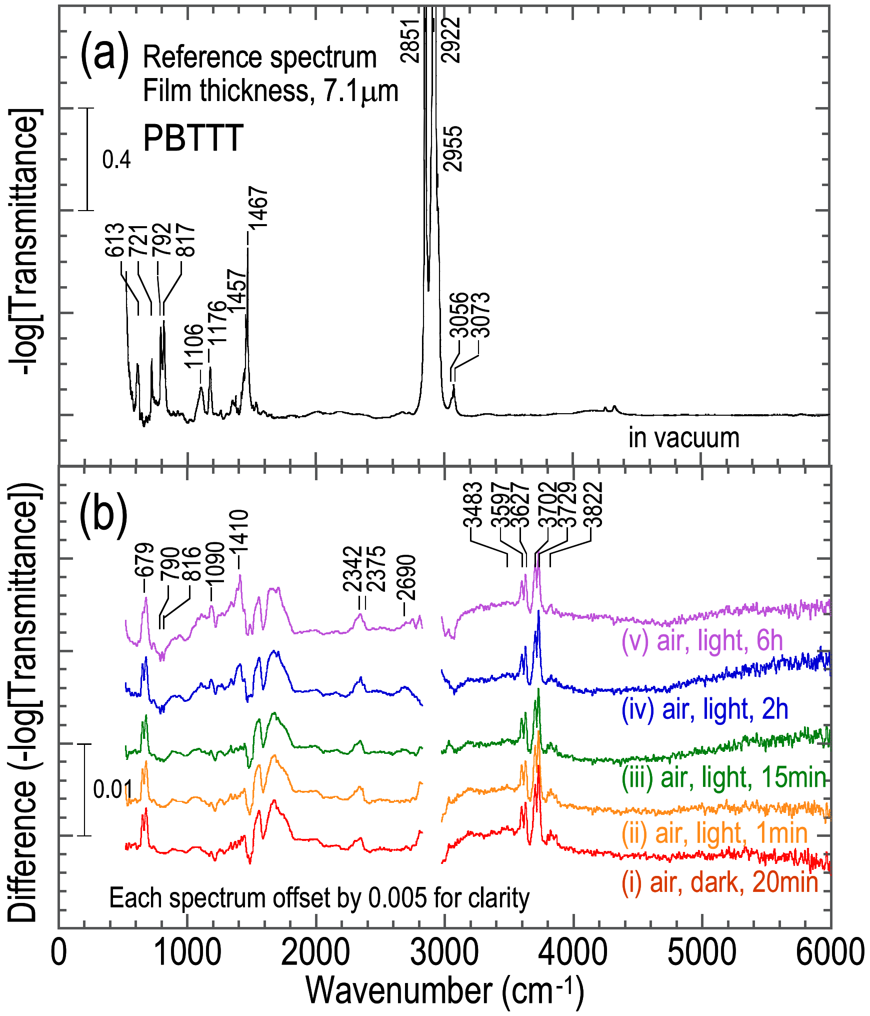

Figure 2.4 FTIR spectra of PBTTT film acquired sequentially after different *in-situ* exposure cleanroom air. (a) Reference spectrum of film in vacuum. (b) Difference spectra obtained by subtracting the spectrum of the film in vacuum, offset for clarity. Molecular spectra of gas-phase H_2O and CO_2 have also been removed for clarity. “Air” and “light” are as defined in caption of Figure 2.3.

After light exposure of 1 min for rr-P3HT and 15 min for PBTTT at the same intensity, the signature of polaron charge carriers emerges (Figure 2.5 and Figure 2.6: curves (ii)). This comprises the near-infrared tail above 2000 cm^{-1} which is the low-energy edge of the first polaron electronic transition,[20,21] and the set of discrete infrared-active vibration (IRAV) modes[29,30] at 850, and 1070 →1160 cm^{-1} for rr-P3HT; and 1485, 1410, 1385, 1348 and 1190 cm^{-1} for PBTTT. [The three humps on this tail for rr-P3HT however are interference fringes due to a small change in refractive index and film thickness.] This confirms progressive light-induced doping of these OSCs.

The polaron transition intensity red-shifts considerably with doping level of the polymer,[31] and with intermolecular interaction of oligomers,[32] but its peak absorption cross-section σ_p is less affected by these effects. From the peak σ_p value of 1.7×10^{-16} cm^2 per polaron found for weakly-doped polythiophene[31] and oligothiophenes,[32] we estimated the final polaron concentration to be 4.5×10^{17} cm^{-3} (i.e., 0.01 mol% of rings) for rr-P3HT, and 1.5×10^{17} cm^{-3} (i.e., 0.003 mol% of rings) for PBTTT. These concentrations are a small fraction of the H_2O (and O_2) present in the films, and are in good agreement with the FET results. The photo-doping quantum yield (i.e., polaron generated per photon absorbed in the fundamental π–π^* band) can thus be estimated to be $\approx 1 \times 10^{-4}$ for rr-P3HT and 1×10^{-5} for PBTTT films equilibrated in the ambient. Hence although the rate is decreased in PBTTT for a factor of ten, the equilibrium doping level is decreased only by a factor of 2–3. This shows the better stability of PBTTT is primarily kinetic rather than thermodynamic in origin.

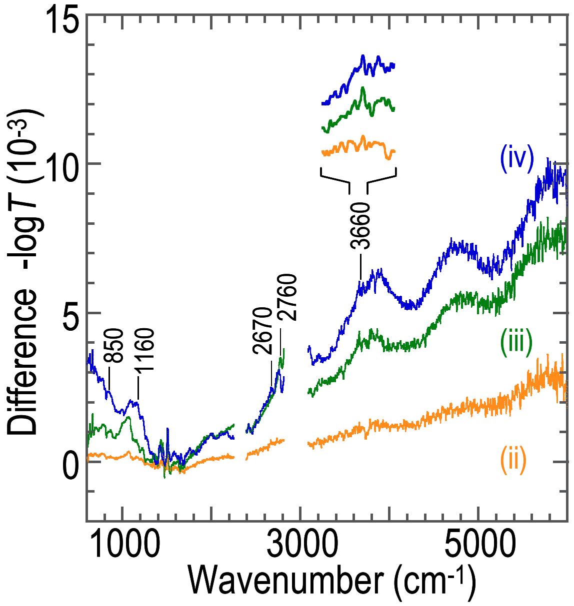

Figure 2.5 Difference spectra by subtracting the spectrum of the rr-P3HT film in air and in the dark. Spectra labels are the same as in Figure 2.3(b).

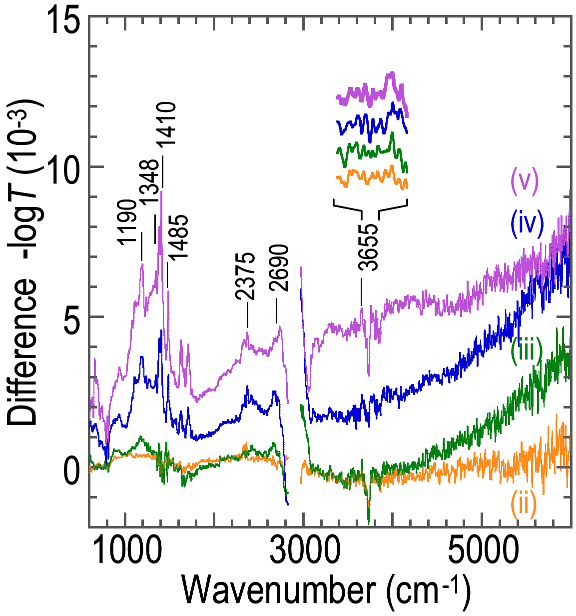

Figure 2.6 Difference spectra by subtracting the spectrum of the PBTTT film in air and in the dark. Spectra labels same as in Figure 2.4(b).

Identification of the counter-ion

To identify the counter ion produced is even more challenging because counter-ion vibrations do not have the large oscillator strengths characteristic of polaron electronic transitions or the IRAV modes. Careful inspection of the difference spectra Figure 2.5 and Figure 2.6 nevertheless reveals progressive growth of new bands (2670, 2760 and 2800–3000 cm^{-1} for rr-P3HT; 2375 and 2690 cm^{-1} for PBTTT) that do not belong to the polymer or H_2O (νOH vibrations lie above 3100 cm^{-1}; while the δH_2O vibration lies within the range 1590–1640 cm^{-1}).[25-27] These resemble the red-shifted stretching bands of H_2O bonded to OH^-.[33,34] The frequency of the OH^- vibration is expected at 3655–3695 cm^{-1}.[33,34] In fact such a band is detected at 3660 cm^{-1}. The final integrated intensities of these bands, assuming a cross-section of 0.70×10^{-16} cm per OH^- (taken to be half of that of H_2O), suggest an OH^- concentration of $3.5 \pm 0.5 \times 10^{17}$ cm^{-3} in rr-P3HT, and $1.5 \pm 0.5 \times 10^{17}$ cm^{-3} for PBTTT, which are in excellent agreement with the respective polaron densities found. This completes the evidence for a photo-doping mechanism of OSCs involving H_2O dispersed in the matrix.

2.3.3 Role of oxygen and moisture in the photo-doping pathway

To distinguish between the effects of O_2 and H_2O, we measured the response of rr-P3HT to dry synthetic air (pO_2 = 21%, pH_2O < 5 ppm) and wet N_2 (pO_2 < 1 ppm; RH = 66%, set by saturated sodium nitrite solution) in the dark and then at similar light exposures. The sequential difference spectra are shown in Figure 2.7(a) and (b) respectively. It is evident that wet $N_{2,}$ but not the dry synthetic air, can give a measurable photo-doping of the OSC. However the equilibrium H_2O concentration in the film is about one-fifth of that in the film exposed to ambient air, and the final polaron concentration is only 0.7×10^{17} cm^{-3}. In addition, exposure to dry synthetic air (but not wet N_2) changes the intensities of the skeletal vibrations at the 1–2% level, as is the case when the film is exposed to ambient air. This suggests that O_2 interacts with the thiophene core[11] to cause a local perturbation and re-orientation of the rings, with possible dilation of the local $\pi \ldots \pi$ distance, which may then promote further intercalation of H_2O. However O_2 alone does not appear to efficiently cause photo-doping. This is consistent with other findings, which showed that oxygen at 1 atm results only in lightly doped polythiophenes with $\sigma \sim 10^{-6}$ S cm^{-1}.[5,6] Also the presence of OH^- suggests that ozone[7] does not need to be the primary cause under normal conditions.

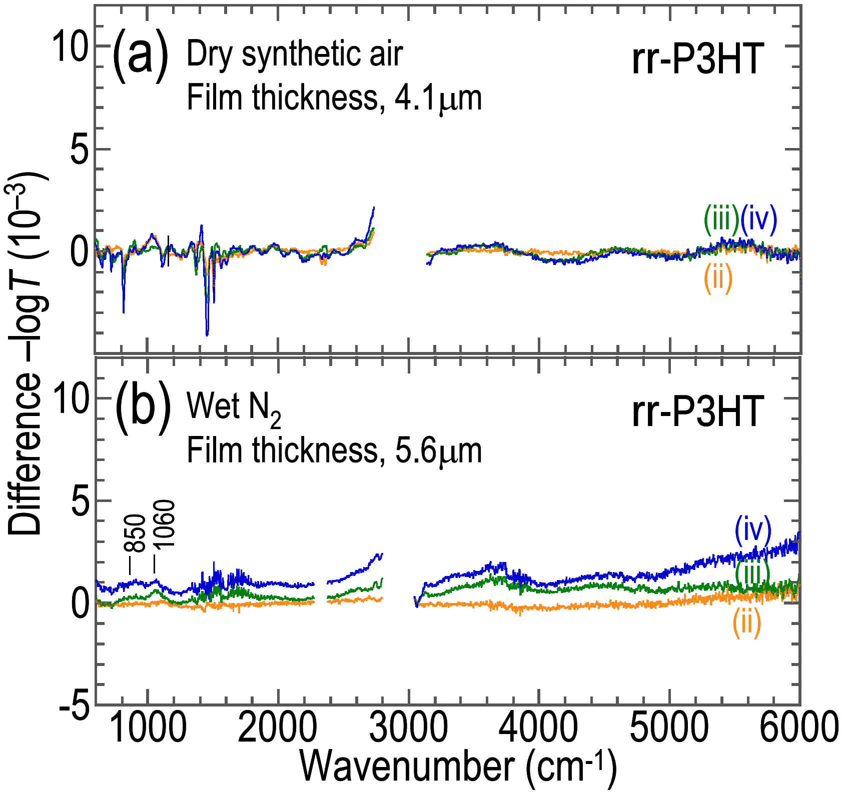

Figure 2.7 Difference FTIR spectra of rr-P3HT films by subtracting the spectrum of the film equilibrated in the following atmospheres in the dark from those acquired sequentially after different *in-situ* light exposure: (a) in dry synthetic air (pO_2 = 21%; pH_2O < 5 ppm), and (b) in wet N_2 (RH 66%, pO_2 < 1 ppm). Spectra labels same as in Fig. 2.3(c). "Ambient air" and "light" are as defined in caption of Fig. 2.3(c).

Formation of counter-ion

The photogeneration of OH^- may be by direct photo-injection into H_2O, or indirectly by photo-injection into O_2 to give the superoxide O_2^- which reacts with H_2O to give OH^- and OOH• radical (e.g., $O_2^- + H_2O \rightarrow OOH• + OH^-$), or by injection into OH• and OOH• intermediates. To overview these possibilities, we plot in Figure 2.8 the highest occupied molecular orbital (HOMO) and the (estimated) lowest unoccupied molecular orbital (LUMO) of PBTTT together with the electron affinities (EAs) of O_2, H_2O, OH• and OOH• and their molecular hydrates which may take part in the process. These EA values were rigidly shifted from experimental values measured in vacuum[35] by +1.5 eV to account approximately for the solid-state polarization-energy stabilization of the anions.[36] These need to be further shifted (not shown) by the mutual Coulomb stabilization of the polymer hole polaron and the anion,[37] which may amount to few tenths of an eV.

The diagram suggests that while none of these species can dope the OSC to any significant extent in the ground state, the photoexcited LUMO electron can be injected into OH•, OOH• and hydrated $O_2(H_2O)_n$ species. Hydrated $O_2(H_2O)_n$ clusters are deeper-lying acceptors than the O_2 molecule itself. This should then give rise to transient photo-hole-doping of the OSC, which experimentally persists for hours to days. Dry O_2 or pure H_2O clusters themselves are expected to be poor electron acceptors, which is borne out experimentally, although H_2O appears to be able to give photo-doping.

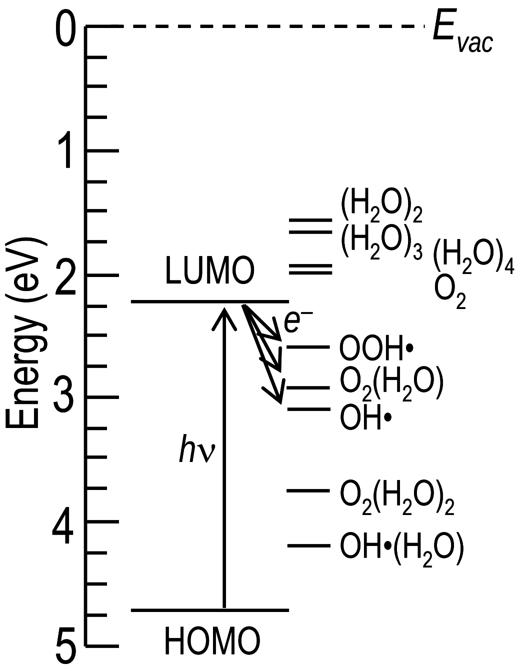

Figure 2.8 Schematic of energetic levels of acceptor species relevant to the photo-hole-doping of the organic semiconductor. All energies refer to the solid-state, but without Coulomb relaxation.

2.3.4 On the origin of higher stability

For a comparative study, we have used here polymers of similar molecular weights, and very thick (1 mm) films which were prepared by drop-casting from chlorobenzene and annealed to give maximum crystallinity with random orientation of the crystallites. This gives essentially "powder" diffractograms, from which the XRD crystallinity can be computed from

$$\chi = \frac{\int_{Bragg} \mathrm{I}\cdot\sin^2\theta\cdot\cos\theta\cdot d\theta}{\int_{total} \mathrm{I}\cdot\sin^2\theta\cdot\cos\theta\cdot d\theta}\ .^{38}$$

In contrast, thin films show strong texturing (i.e., preferred orientation of their crystallites) due to substrate alignment.[16,39-41]

Both rr-P3HT and PBTTT show the characteristic progression of (*h*00) Bragg reflections arising from their lamellae structure, and a distinct (010) reflection due to $\pi\ldots\pi$ stacking,[16,39-41] which can be separated from the background using a Gaussian sum to model the amorphous scattering. We found χ be higher for PBTTT (27%) than rr-P3HT (21%). This is primarily due to better lamellae order, as evidenced by the higher intensity and visibility of reflections up to the fourth order of (100), whose spacing (22.0 Å) is also larger than in rr-P3HT (16.8 Å) due to its longer side chain. The Debye–Waller factor σ^2 in $I = I_0 \exp(-\sigma^2 q^2)$ is 2.9 Å^2 for PBTTT and *ca*. 4.5 Å^2 for rr-P3HT. The Scherrer coherence length $\ell_{coh} = \dfrac{0.9\lambda}{\theta_{fwhm} \cos\theta}$ is 30 nm for PBTTT and 22 nm for rr-P3HT. However PBTTT shows a (010)-spacing (3.64 Å; $\ell_{coh} = 9$ nm) in the $\pi\ldots\pi$ stacking direction that is smaller than rr-P3HT (3.78 Å; $\ell_{coh} = 17$ nm). This suggests its thiophene rings are stacked in a slightly closer packing (i.e., more eclipsed configuration) which may retard the close approach of H_2O and O_2. Achieving high crystallinity and close $\pi\ldots\pi$ stacking particularly at the dielectric interface itself may thus be helpful not only for improved charge-carrier mobility but also improved stability.

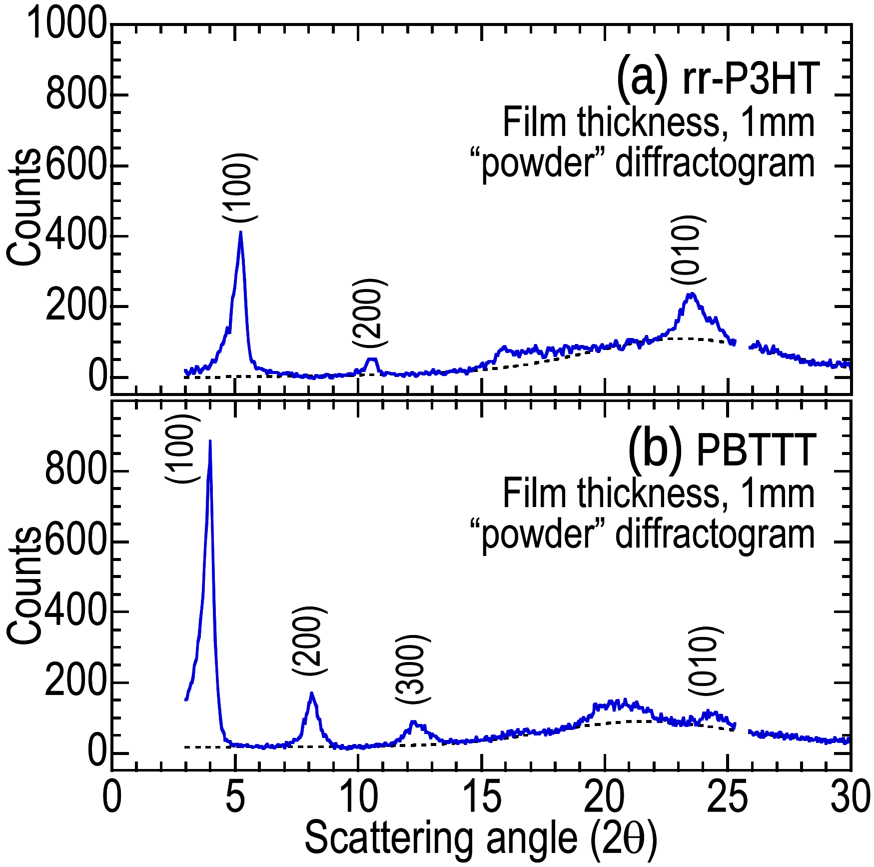

Figure 2.9 θ–2θ XRD diffractograms of 1 mm-thick films of (a) rr-P3HT and (b) PBTTT at room temperature in vacuum (10^{-2} mbar) using Cu K_α radiation. Solid line is data, dotted line is fitted amorphous background using a sum of two Gaussians.

2.3.5 Improved stability: Device encapsulation

To further probe the effect of retarding the diffusion of H_2O and O_2 into the polymer film on the photo-doping process, an rr-P3HT FET was capped with a layer of 1 mm- thick PDMS film before exposure to the ambient. A schematic of the cross- section of the device is shown in Figure 2.10 and the transfer characteristics are shown in Figure 2.11. Before exposure, the pristine FETs requires V_g = +5 V to turn *off*. After exposure to orange-filtered cleanroom ambient light for 30 min (Figure 2.11 (ii)) at the same intensity as defined in Figure 2.1, there was no significant shift in the V_g to turn *off* and the bulk carrier density remained almost identical. This observation further validated that the doping mechanism relies on the presence of H_2O and O_2 with light and showed possible device preservation by back- end encapsulation.

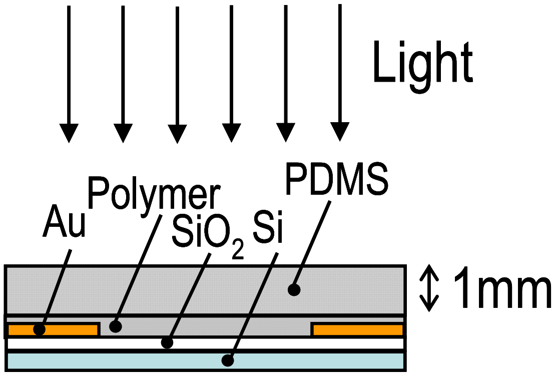

Figure 2.10 Schematic of the cross- section of an rr-P3HT FET capped with a layer of PDMS film.

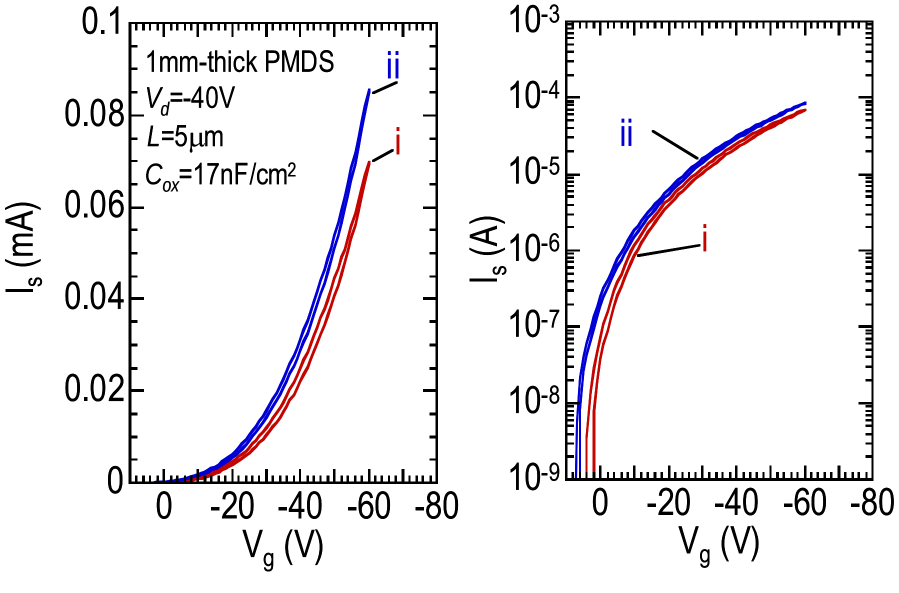

Figure 2.11 FET transfer characteristics of rr-P3HT capped with a layer of 1 mm-thick PDMS film. (i) Pristine and (ii) After exposure to the ambient for 30 min. “Ambient” corresponds to cleanroom air (22ºC, RH 60%) and an absorbed photon flux intensity of 9 x 10^{13} ph s^{-1} cm^{-2}. Left and right panels give the linear and log plots respectively.

2.4 Conclusion

In summary, this chapter uncovers a photo-doping pathway in thiophene-based organic semiconductors that degrades their electronic semiconductor properties when exposed to the ambient air and light. Water plays a key role in this mechanism, while oxygen plays a secondary role in promoting the water sorption. Therefore the elimination and exclusion of sorbed H_2O is central to device stability. High crystallinity is the key to improving stability by excluding sorbed species from the interior of the crystallite domains. This photo-doping mechanism may also account for the photoluminescence quenching and polaron photogeneration observed in optical-pumping experiments, if moisture was inadvertently introduced into the films by exposure to the ambient. These results are for devices at “rest”. If the devices are operated in the ambient, we may further expect injected carriers to also participate in electrochemical processes,[42] such as of the type recently described for poly(3,4-ethylenedioxythiophene).[43]

2.5 References

1 Kim, J. S., Ho, P. K. H., Murphy, C. E., Baynes, N. & Friend, R. H. Nature of non-emissive black spots in polymer light-emitting diodes by in-situ micro-raman spectroscopy. *Adv. Mater.* 14, 206-209 (2002).

2 Kim, J. S. *et al.* Electrical degradation of triarylamine-based light-emitting polymer diodes monitored by micro-Raman spectroscopy. *Chem. Phy. Lett.* 386, 2-7 (2004).

3 Ficker, J. *et al.* Influence of intensive light exposure on polymer field-effect transistors. *Appl. Phys. Lett.* 85, 1377-1379 (2004).

4 Tanase, C., Meijer, E. J., Blom, P. W. M. & De Leeuw, D. M. Unification of the hole transport in polymeric field-effect transistors and light-emitting diodes. *Phys. Rev. Lett.* 91, 216601-216601-216604 (2003).

5 Horowitz, G., Peng, X., Fichou, D. & Garnier, F. The oligothiophene-based field-effect transistor: How it works and how to improve it. *J. Appl. Phys.* 67, 528-532 (1990).

6 Meijer, E. J. *et al.* Dopant density determination in disordered organic field-effect transistors. *J. Appl. Phys.* 93, 4831-4835 (2003).

7 Chabinyc, M. L., Street, R. A. & Northrup, J. E. Effects of molecular oxygen and ozone on polythiophene-based thin-film transistors. *Appl. Phys. Lett.* 90, 123508-123501-123503 (2007).

8 Hoshino, S. *et al.* Influence of moisture on device characteristics of polythiophene-based field-effect transistors. *J. Appl. Phys.* 95, 5088-5093 (2004).

9 Brown, A. R., Jarrett, C. P., de Leeuw, D. M. & Matters, M. Field-effect transistors made from solution-processed organic semiconductors. *Synth. Met.* 88, 37-55 (1997).

10 Taylor, D. M., Gomes, H. L., Underhill, A. E., Edge, S. & Clemenson, P. I. Effect of oxygen on the electrical characteristics of field effect transistors formed from electrochemically deposited films of poly(3-methylthiophene). *J. Phys. D: Appl. Phys.* 24, 2032-2038 (1991).

11 Abdou, M. S. A., Orfino, F. P., Son, Y. & Holdcroft, S. Interaction of oxygen with conjugated polymers: charge transfer complex formation with poly(3-alkylthiophenes). *J. Am. Chem. Soc.* 119, 4518-4524 (1997).

12 De Leeuw, D. M., Simenon, M. M. J., Brown, A. R. & Einerhand, R. E. F. Stability of n-type doped conducting polymers and consequences for polymeric microelectronic devices. *Synth. Met.* 87, 53-59 (1997).

13 Sirringhaus, H. *et al.* Two-dimensional charge transport in self-organised, high-mobility conjugated polymers. *Nat.* 401, 685-688 (1999).

14 Kline, R. J., McGehee, M. D., Kadnikova, E. N., Liu, J. & Fréchet, J. M. J. Controlling the field-effect mobility of regioregular polythiophene by changing the molecular weight. *Adv. Mater.* 15, 1519-1522 (2003).

15 McCulloch, I. *et al.* Liquid-crystalline semiconducting polymers with high charge-carrier mobility. *Nature Mater.* 5, 328-333 (2006).

16 Chabinyc, M. L., Toney, M. F., Kline, R. J., McCulloch, I. & Heeney, M. X-ray scattering study of thin films of poly(2,5-bis(3-alkylthiophen-2-yl)thieno[3,2-b]thiophene). *J. Am. Chem. Soc.* 129, 3226-3237 (2007).

17 Measured by ultraviolet photoemission spectroscopy, with photoemission onset extracted self-consistently.

18 Umeda, T., Tokito, S. & Kumaki, D. High-mobility and air-stable organic thin-film transistors with highly ordered semiconducting polymer films. *J. Appl. Phys.* 101, 054517-054511-054515 (2007).

19 Wang, S. *et al.* Solvent effects and multiple aggregate states in high-mobility organic field-effect transistors based on poly(bithiophene-alt-thienothiophene). *Appl. Phys. Lett.* 93, 162103-162101-162103 (2008).

20 Heeger, A. J., Kivelson, S., Schrieffer, J. R. & Su, W. P. Solitons in conducting polymers. *Rev. Mod. Phys.* 60, 781-850 (1988).

21 Jiang, X. M. *et al.* Spectroscopic studies of photoexcitations in regioregular and regiorandom polythiophene films. *Adv. Funct. Mater.* 12, 587-597 (2002).

22 Eastoe, J., Hollambly, M. J. & Hudson, L. Recent advances in nanoparticle synthesis with reversed micelles. *Adv. Colloid Interface Sci.* 128, 5-15 (2006).

23 The incident photon spectral intensity $S(\lambda)$ was measured with a calibrated spectrograph and photodiode system. The absorbed photon flux n_{ab} was obtained by integrating this $S(\lambda)$ over the absorption spectrum of the film. This is the relevant parameter to quantify the potential for reaction because all low-lying electronically excited states relax back to the ground excited state from which photochemical processes occur.

24 van Krevelen, D. W. *Properties of polymers. Their correlation with chemical structure: their numerical estimation and prediction from additive group contributions*. 3 edn, (Elsevier, 1990).

25 Bentwood, R. M., Barnes, A. J. & Orville-Thomas, W. J. Studies of intermolecular interactions by matrix isolation vibrational spectroscopy: self-association of water. *J. Mol. Spectr.* 84, 391-404 (1980).

26 Ayers, G. P. & Pullin, A. D. E. The i.r. spectra of matrix isolated water species: I. Assignment of bands to the $(H_2O)_2$, $(D_2O)_2$ and HDO dimer species in argon matrices. *Spectrochim. Acta* 32A, 1629-1639 (1976).

27 Huisken, F., Kaloudis, M. & Kulcke, A. Infrared spectroscopy of small size-selected water clusters. *J. Chem. Phys.* 104, 17-25 (1996).

28 Robertson, C. W. & Williams, D. Lambert absorption coefficients of water in the infrared. *J. Opt. Soc. Am.* 61, 1316-1320 (1971).

29 Horovitz, B. Infrared activity of Peierls systems and application to polyacetylene. *Solid State Commun.* 41, 729-734 (1982).

30 Lopez Navarrete, J. T. & Zerbi, G. Lattice dynamics and vibrational spectra of polythiophene. II: Effective coordinate theory, doping induced, and phoexcited spectra. *J. Chem. Phys.* 94, 965-970 (1991).

31 Kaneto, K., Hayashi, S., Ura, S. & Yoshino, K. ESR and transport studies in electrochemically doped polythiophene film. *J. Phys. Soc. Jpn.* 54, 1146-1153 (1985).

32 van Haare, J. A. E. H. *et al.* Redox states of long oligothiophenes: two polarons on a single chain. *Chem. Eur. J.* 4, 1509-1522 (1998).

33 Robertson, W. H., Diken, E. G., Price, E. A., Shin, J. W. & Johnson, M. A. Spectroscopic determination of the OH^- solvation shell in the $OH^-.(H_2O)_n$ clusters. *Science* 299, 1367-1371 (2003).

34 Lee, H. M., Tarkeshwar, P. & Kim, K. S. Structures, energetics and spectra of hydrated hydroxide anion clusters. *J. Chem. Phys.* 121, 4657-4664 (2004).

35 *NIST chemistry webbook, NIST standard reference database number 69 (http://webbook.nist.gov)*. (National Institute of Standards and Technology).

36 Pope, M. & Swenberg, C. E. *Electronic processes in organic crystals and polymers*. 2 Ed edn, (Oxford University Press, 1999).

37 Chia, P. J. *et al.* Direct evidence for the role of the Madelung potential in determining the work function of doped organic semiconductors. *Phys. Rev. Lett.* 102, 096602-096601-096604 (2009).

38 Ruland, W. X-ray determination of crystallinity and diffuse disorder scattering. *Acta Cryst.* 14, 1180-1185 (1961).

39 Chen, T. A., Wu, X. & Rieke, R. D. Regiocontrolled synthesis of poly(3-alkylthiophenes) mediated by Rieke zinc: their characterisation and solid-state properties. *J. Am. Chem. Soc.* 117, 233-244 (1995).

40 Aasmundtveit, K. E. *et al.* Structural anisotropy of poly(alkylthiophene) films. *Macromolecules* 33, 3120-3127 (2000).

41 Hugger, S., Thomann, R., Heinzel, T. & Thurn-Albrecht, T. Semicrystalline morphology in thin films of poly(3-hexylthiophene). *Colloid Polym. Sci.* 2004, 932-938 (2004).

42 Chua, L. L. *et al.* General observation of n-type field-effect behaviour in organic semiconductors. *Nature* 434, 194-199 (2005).

43 Chia, P. J. *et al.* Injection-induced de-doping in a conducting polymer during device operation: asymmetry in the hole injection and extraction rates. *Adv. Mater.* 19, 4202-4207 (2007).

Chapter 3. Interferogram-modulated Fourier-transform charge modulation spectroscopy

In this chapter, we describe the development of a novel and more efficient interferogram-modulated Fourier-transform charge modulation spectroscopy (FT-CMS) technique that provided higher sensitivity (*ca.* 10^{-6}) than the widely-used *on-off* FT-IR method.

This FT-CMS method is successfully used to measure the infrared absorption spectrum of the polaron charges at the Fermi-level E_f in a heavily *p*-doped conducting poly(3,4-ethylenedioxythiophene)–poly(styrenesulfonic acid) (PEDT:PSSH) film. The spectrum indicates softer phonons and weaker electron–phonon coupling riding on a strongly red-shifted Drude-like electronic transition, different from the population-averaged “bulk” spectrum. This provides direct evidence that the E_f holes are sufficiently delocalized even in such disordered materials to reside in an energy continuum (band states) while the rest of the hole population resides in self-localized gap states.

3.1 Introduction

Despite significant advances in high-performance π-conjugated OSC materials, a number of fundamental aspects of their semiconductor physics remain to be clarified. This includes the nature of the charge carriers in these materials which determines mobility and other properties. While self-trapped polaron (P^{+}) and bipolaron (BP^{2+}) states are well-established respectively for the singly- and doubly-charged oligomers in the solution state,[1] the description in longer chains[2] and particularly in the solid state is unclear.

In heavily-doped OSCs, a finite density-of-states at the Fermi level $D(E_f)$ has been firmly established from Pauli spin susceptibility and ultraviolet photoemission measurements for a wide range of materials.[3] This can arise either from localized gap states smeared out by Coulomb disorder,[4] or from states delocalized by interchain interaction.[5] In heavily-doped polymer OSCs, measurements that reflect the entire carrier population, such as infrared (IR) or temperature-dependent dc conductivity σ_{dc} indicated significant carrier localization due to Coulomb and site disorder, except in a recent unusual sample of polyaniline doped with camphorsulfonic acid.[6] In undoped and highly-ordered OSCs on the other hand, IR measurements of field-induced carriers[7] and photogenerated carriers[8] not subjected to such disorder have yielded a more extended delocalization.

Here we have directly measured the spectrum of the E_f holes in a *p*-doped PEDT:PSSH[9] using a more efficient interferogram-modulated Fourier-transform charge modulation spectroscopy (FT-CMS) technique to determine whether its finite $D(E_f)$ is related more to Coulomb disorder or interchain P^{+} interaction.

Poly(3,4-ethylenedioxythiophene)–poly(styrenesulfonic acid) (PEDT:PSSH)

Poly(3,4-ethylenedioxythiophene) has unprecedented thermal and electrochemical stability and can be prepared by standard oxidative or electrochemical polymerization methods[9] and was initially found to be an insoluble polymer. Poly-(3,4-ethylenedioxythiophene) complexed with polystyrene sulfonic acid (PEDT:PSSH) is a blend that allows PSS^- to act as a source of the charge balancing counter ion and to keep the PEDT segments dispersed in the aqueous medium, hence enhancing processability. It is obtained directly in the *p*-doped state (i.e. $PEDT^+$) by oxidative polymerization of ethylenedioxythiophene in an aqueous emulsion in the presence of PSSH.

PEDT:PSSH is the prototype of a heavily-doped but highly-disordered conducting polymer widely used in organic electronics as a hole conductor and injector. The chemical structure of PEDT:PSSH is shown in Figure 3.1. This polymer blend displays good film-forming properties, has high electrical conductivity (approximately 10 S cm^{-1}), high transparency to visible light and excellent chemical stability. The PEDT:PSSH used here has a mole ratio of PEDT-to-PSS ≈ 0.34[10] and a doping level of ≈ 0.3 holes/ring,[10] which corresponds to a carrier concentration of ≈ 3×10^{20} cm^{-3}, but a short conjugation length of ≈ 12–20 rings/chain.[10] We use "holes" and "P^+" interchangeably here. Although holes in heavily doped conducting polymers have sometimes been described as BP^{2+} in the literature, we consider in the balance of recent theoretical work[11] and IR and Raman spectroscopy[12] of *p*-PEDT that the P^+ character is dominant. Nevertheless, our conclusions do not depend on the distinction between P^+ and BP^{2+}.

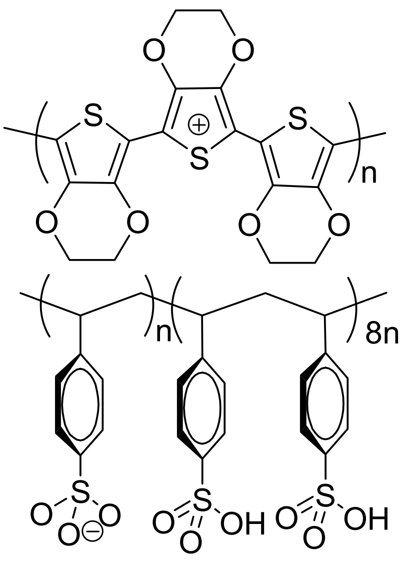

Figure 3.1 The chemical structure of PEDT:PSSH

Charge modulation spectroscopy in mid-IR spectral range: A conventional approach

An *on-off* method has been widely used previously in the mid-IR region where vibronic signatures of charges carriers in OSCs can be found. In this method, FT-IR absorption spectra were measured with the device biased at V_1 and V_2 respectively and subtracting one spectrum from the other to obtain the difference (ΔT) spectrum. The final CMS spectrum is presented as $\Delta T/T$ where the difference spectrum is normalized against the reference transmittance spectrum. However the reliability of such an *on-off* method depends on the stability of the system over time since the two spectra are not measured simultaneously. Simultaneous measurement not only reduces the time required to perform the experiment, but also minimizes spectral artifacts arising from time-dependent atmospheric and spectrometric deviations during the period of data collection.

3.2 Experimental

3.2.1 Device fabrication

A 50-nm-thick PEDT:PSSH film (HC Starck, Leverkussen) was spin-cast over an oxygen-plasma-treated interdigitated Cr/Au source–drain array fabricated by photolithography on 200-nm thermal SiO_2/p^{++}-Si. The channel length and width of this array is 20 μm and 22.5 cm and the area is *ca*. 3 x 3 mm. Electrical connections to the source and drain electrodes were made with Ag paint. The film was then heated at 120°C for 15 min to remove moisture, and mounted in the N_2-purged spectrometer (Nicolet 8700 FT-IR) at room temperature.

3.2.2 Development of an interferogram-modulated FT-CMS method

A commercial Nicolet 8700 FT-IR spectrometer was used in which the Fourier-transform technique compares favourably to a dispersive infrared spectrometer. The signal-to-noise ratio is enhanced (also known as Fellgett advantage) for an FTIR spectrum recorded over the same total time as a dispersive spectrum. The optics of a Fourier transform instrument provides a much better energy throughput (also known as Jacquinot advantage) than the latter in which the throughput is limited by the necessity of narrow slit widths. The position of the moving mirror and hence the frequency is also measured with great precision by counting interference fringes from a helium-neon laser (also known as Connes advantage).[13]

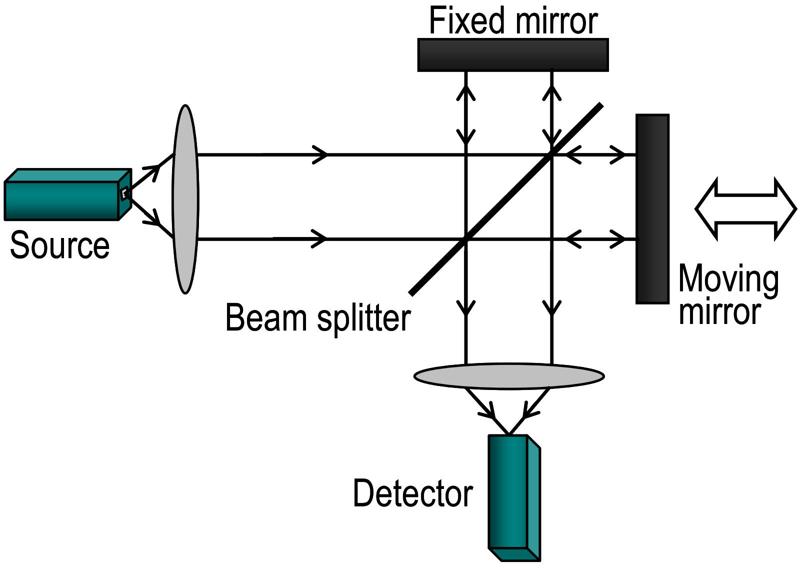

Figure 3.2 Schematic of a classic Michelson interferometer which consist of the three major components: a fixed mirror, moving mirror and a beam splitter.

The heart of a FT-IR spectrometer is the Michelson interferometer. The schematic of a Michelson interferometer is shown in Figure 3.2. The detector in the spectrometer sees the reflected beams from the fixed and moving mirror simultaneously. The two combined beams interfere constructively or destructively depending on the wavelength of the light and the optical path difference (also known as retardation, δ) determined by the position of the moving mirror. The interferogram I (δ) is constructed from signals received by the detector as a function of retardation.

In a continuous-scan interferometry, the moving mirror moves at a constant velocity (cm s^{-1}) and because of the continuous mirror movement, the interferogram I(δ) becomes an explicit function of time described by the Fourier frequency.[13] The use of laser signal ensures that I(δ)

is measured at precisely equal intervals of mirror positions and provides an internal wavelength calibration for every scan. Instead of the conventional continuous-scan interferometry, a step-scan technique is used in which the movable mirror moves incrementally in steps. The movable mirror is held stationary at each equally spaced sampling position and then moved rapidly to the next sampling position. The step-scan interferometry eliminates Fourier modulation interference encountered in continuous-scan FT-IR and allows measurements to be made as an explicit function of phase, time, or space.[14]

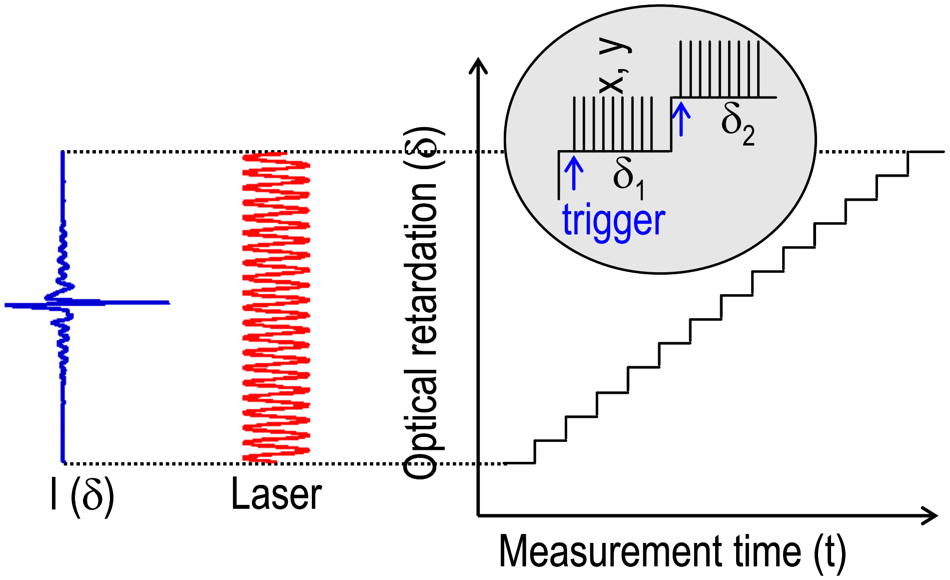

Figure 3.3 Data acquisition scheme for the space-resolved step-scan FT-IR experiment. The interferogram I (δ) constructed is shown in the left panel.

The data acquisition scheme for a space-resolved step-scan experiment is illustrated in Figure 3.3. The interferogram signal is produced by integrating the detector output signal during the time interval t_{coll} that the mirror is held stationary while the time interval during which the mirror is stepped from one sampling position to the next is lost time that does not contribute to the observation. An additional settling time t_{set} can be set to allow the mirror to settles in its new position before data acquisition commences.

Figure 3.4 shows a schematic of the experimental setup. A device is mounted in the N_2-purged spectrometer (Nicolet 8700 FT-IR) at room temperature. Light from the broadband IR source was passed through the beam-splitter and Michelson interferometer and focused onto the device. The transmitted intensity is measured by a mercury cadmium telluride (MCT) detector with bandwidth of 50 Hz – 150 kHz. The reference output voltage from a lock-in amplifier (SRS 830) was amplified by a homebuilt high-voltage summing amplifier, superimposed on a dc bias, and injected into the electrode array.

The dc interferogram (IFG) was first collected by rapid scan (v_{scan} = 0.6329 – 1.8987 cm s^{-1}) taking care to keep the Fourier frequencies ($f_F = 2\ v_{scan}\ \overline{\nu}$) within the detector bandwidth, and FT to the single-beam dc spectrum. The in-phase and quadrature root-mean-square (rms) ac IFG was collected by step-scan of the mirror displacements (retardation) and demodulating detector response at each step at f_{mod} using the lock-in amplifier, and FT to their respective ac spectra. An appropriate settling time t_{set}, time constant τ, filter slope S and collection time t_{coll} are used. The dc spectrum can also alternatively be obtained from the dc IFG acquired at each retardation. For phase correction we used de Haseth algorithm, which allows both positive and negative intensities. The zero phase angle was independently verified by pulsing a tungsten lamp (modulation frequency f_{mod} = 0.1 kHz). The $\Delta T/T$ spectra were then obtained by normalizing the ac spectrum to the dc spectrum ($\Delta T/T = -2.303\ \Delta \mathrm{A}$, where A is the absorbance). This technique is an improvement over the on–off method, not only because it provides phase information but also because it allows sample modulation–demodulation to be performed far away from dc, with consequently less 1/f noise.

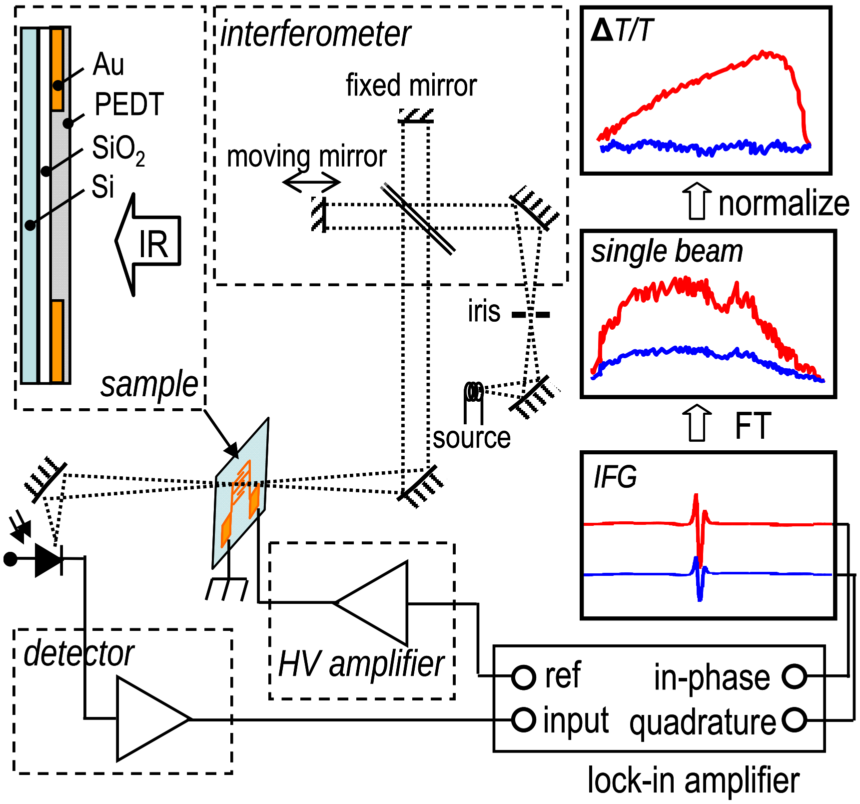

Figure 3.4 A schematic of the interferogram-modulated FT-CMS experiment. Top left inset shows the cross-section of device used in the experiment.

3.2.3 Characterization of the novel experimental method

We first characterized this technique extensively using an optical chopper (SRS 540) to modulate the output through an iris at focus in place of the sample to verify it is well-behaved and reproducible. Figure 3.5 shows an example of the results obtained. The in-phase ac spectrum exactly matches the scaled dc spectrum from rapid scan over a range of f_{mod} (200–

10000 Hz) and v_{scan} (0.1582 – 1.898 cm s^{-1}), indicating that the spectral ratio is $\overline{\nu}$ -independent over a wide range of f_{mod} and v_{scan}. Thus the rapid scan technique can be used to generate the appropriate reference dc spectrum. The ratio of the ac to the dc single-beam spectra (8.0) also closely matches the expected overall gain [i.e., g /(0.9* $\sqrt{2}$)= 7.8, with lock-in amplifier gain g = 10, instrument factor 0.9, and $\sqrt{2}$ to take into account the lock-in outputs rms values for the ac IFG, while the digitizer outputs instantaneous values for the dc IFG], and used for calibrating the intensity response of the technique. The phase spectra were flat (≈ 0º) for all f_{mod} in this range. The detector response (inset) was confirmed to be flat with no gain peaking.

The parameters used for the calibration and in subsequent experiments described in this chapter are as follows. Sample modulation FTS: f_{mod} = 1 kHz, t_{set} = 100 ms, lock-in amplifier time constant τ = 10 ms, S = 24 dB/oct, t_{coll} = 100 ms. Rapid-scan: v_{scan} = 1.898 cm s^{-1}. An IR source, a liquid N_2-cooled (MCT) detector and Ge/KBr beam-splitter are used.

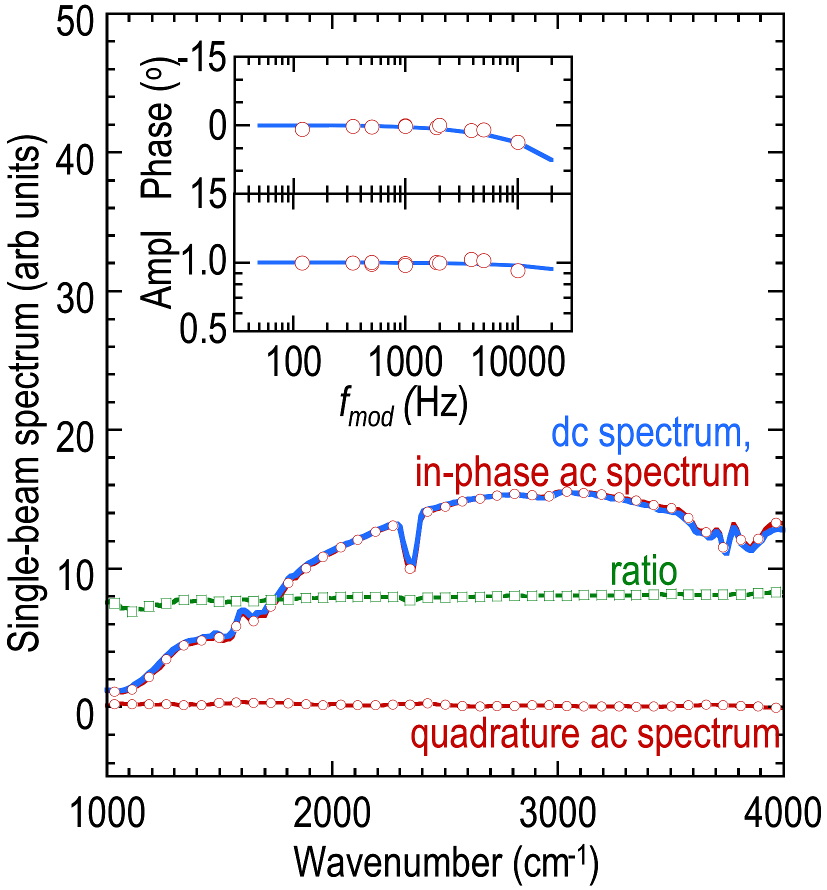

Figure 3.5 Tests with chopping of the beam at focus. In-phase and quadrature ac ΔT/T spectra (circles, 20% of data shown); scaled rapid-scan dc spectrum (continuous line); and the ratio spectrum of in-phase ac to dc (squares). Inset: Relative amplitude and phase response of the MCT detector vs f_{mod} (circles) and theoretical response of a 150 kHz- bandwidth detector (lines).

3.3 Direct evidence for delocalization of charge carriers at the Fermi level in a doped conducting polymer

Figure 3.6 shows the population-averaged IR absorptivity spectrum $\alpha(\bar{\nu})$ of PEDT:PSSH measured in transmission and corrected for reflection losses. Because of the dilution effect of the PSSH matrix, the optical function does not fluctuate strongly in the IR, which thus leads to a nearly flat reflectivity spectrum. This facilitates easy measurement of $\alpha(\bar{\nu})$ which provides a good comparison with the CMS spectra.

The population-average spectrum shows a broad transition which peaks at *ca*. 4400 cm^{-1} (0.55 eV) and tails towards zero at both low and high wavenumbers. This feature is well-established to arise from the electronic excitation of holes,[1,15] even though their exact nature needs further clarification. The spectrum also shows charge-induced vibrational modes (also called in the literature the infrared active vibrations IRAVs) between 1525–773 cm^{-1} (see expanded inset) which are greatly intensified modes due to coupling to hole motion.[16,17] These features are typical of *p*-doped PEDT with different counterions and synthesized in different ways.[18] The current–voltage (*IV*) characteristic (inset) gives an average in-plane dc conductivity of 0.1 S cm^{-1}, and a weak but symmetric deviation from Ohmic behavior at moderate $V > 10$ V (average applied field $E > 5$ kV cm^{-1}) indicating a small increase in carrier mobility. No significant self-heating effects occur in this voltage range (no hysteresis).

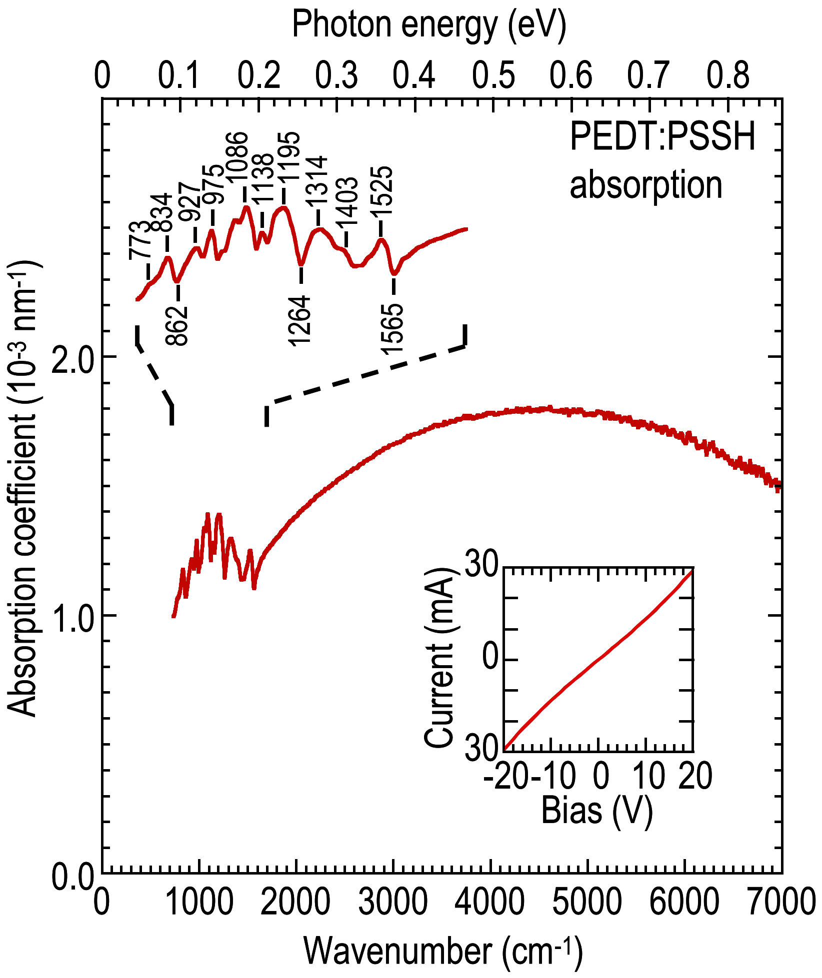

Figure 3.6 Absorption spectrum of a 1:2.5 mol/mol PEDT:PSSH measured in transmission in N_2. Resolution= 16 cm^{-1}. Inset: *IV* characteristic of the interdigitated device (length L = 20 μm; width w = 22.5 cm; area $A \approx 3 \times 3$ mm^2; film thickness t = 50 nm).

The PEDT:PSSH device was then subjected to various excitation conditions of $V_{ac} + V_{dc}$, such that the peak voltage V_{peak} is increased progressively. The corresponding CMS $\Delta T/T$ magnitude spectra are shown in Figure 3.7. No irreversible change in the *IV* characteristics occurred after the measurements, as the data were collected well within the reversible bias regime of PEDT:PSSH. Previous experiments on this material indicated that an irreversible loss in conductance due to injection-induced dedoping occurs at *ca*. 50 kV cm^{-1}, which will require a V_{dc} of 100 V across the electrode array, far above the largest V_{peak} of *ca*. 30 V used here. Thus the charge-modulation spectra collected here are related to the intrinsic transport mechanism of PEDT.

The electronic transition now becomes highly asymmetric as a result of a pronounced redshift of the band maximum to 0.24 eV while leaving a long tail into the visible. Higher resolution spectra not only show vibrational absorption features characteristic of *p*-doped PEDT, but also richer details (compare the expanded insets of Figure 3.6 and Figure 3.7) including pre-resonance dips, e.g. at 1557, 1434, … 797 cm^{-1}. These Fano-type resonances point to strong coupling of the vibrational transition to an underlying electronic transition, which must therefore extend to < 0.1 eV. The corresponding phase spectra were flat near ≈ 0°. Thus these features are induced transmission (i.e. bleaching) in-phase with the peak of the excitation voltage and current. The carriers are transiently depleted at E_f, due to faster hole extraction than injection into the film.[19] The transition dipole moments of vibrational modes in PSSH are too weak ($< 10^{-2}$ of these features) to be observed here.

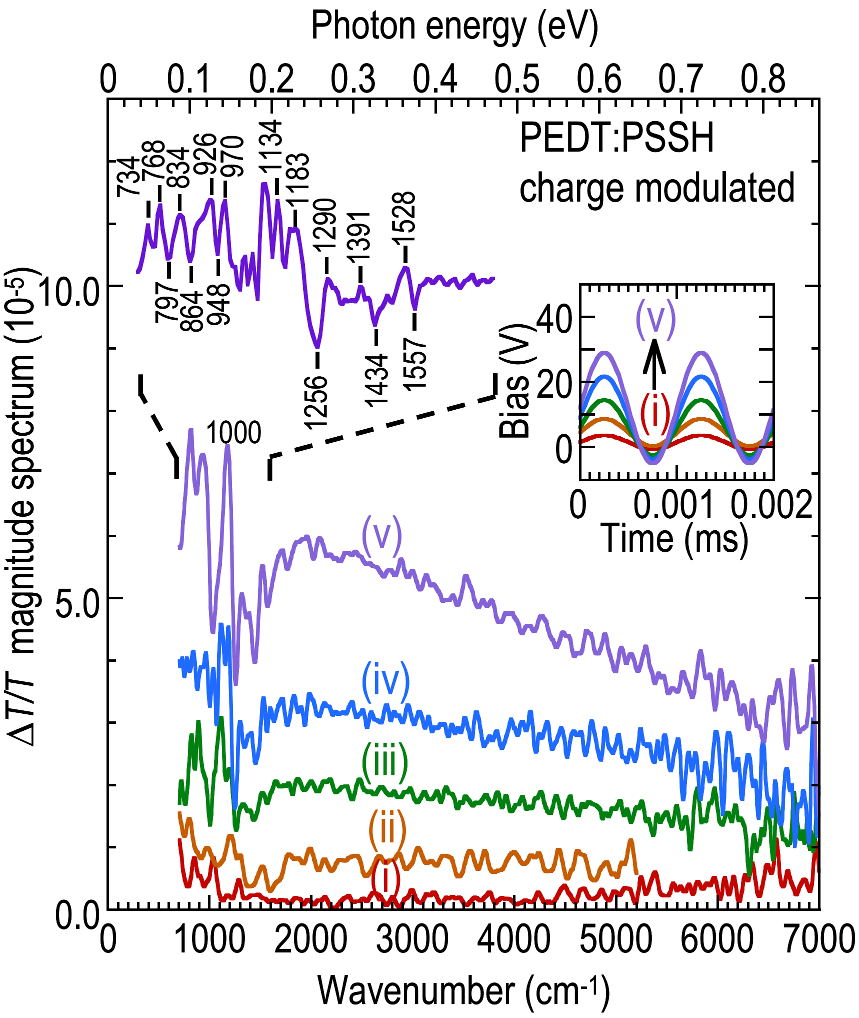

Figure 3.7 CMS $\Delta T/T$ magnitude spectra for excitation conditions (i)–(iv) as shown in the inset. No irreversible change occurred in the *IV* characteristics of the device measured again at the end of each experiment. The phase spectrum is ≈ 0° and spectrally flat. The $\Delta T/T$ spectrum thus corresponds to induced transmission (i.e., bleaching) in phase with the peak in the voltage (and current) excitation cycles. Resolution, 50 cm^{-1} due to mathematical smoothing using a smoothing spline function; expanded spectrum resolution, data collected at 16 cm^{-1} resolution for conditions similar to (v) and unsmoothed.

The frequency dispersion of these charge-induced phonon modes relates directly to electron delocalization, which has been described in both the effective conjugate coordinate (ECC)[17] and the amplitude mode (AM)[16] theories. The red-shifting of the modes due to increasing electron delocalization and hence lowering electron–phonon (*e–ph*) coupling strength can be quantified by an effective force constant (in ECC theory) or a collective phonon propagator (AM). Detailed AM dispersion plots have been computed for polythiophene by Österbacka et al (see Fig. 3b in Ref[8]). A number of these symmetric modes are sufficiently weakly coupled to the 3,4-ethylenedioxy bridge to be useful also for PEDT, as confirmed experimentally. Using seven of the charge-induced modes of *p*-doped PEDT, we obtained the pinning parameter[8] α_p = 0.24±0.01 for E_f holes, compared with 0.33±0.01 for the population average, in *p*-doped PEDT; and 0.27 in *p*-doped regioregular P3HT.[8] Thus the Fermi-level holes are more delocalized than the population average. This conclusion is robust and independent of model details, since both the electronic and phonon features of the modulated spectrum are clearly red-shifted.

The strong asymmetry of the electronic feature in the modulated spectra suggests significant Drude-like character. Furthermore, this peak position (0.2 eV) is considerably red-shifted from the 1.1 eV expected of the first electronic transition of the isolated *p*-doped PEDT chains at similar doping levels. [Both thiophene and PEDT oligomer cations in the solution-state give the first electronic transition at 1.1 eV at a doping level of 0.3 h^+/ring, regardless of whether P^+ or BP^+ were present, while π–π dimerization leads to a general blue shift.][20] Therefore the interchain delocalization here is more extensive, even though it is still incomplete. Accordingly we fitted the data to a Drude model that has been modified to incorporate weak localization effects to find the effective plasma $\overline{\nu}_p$ and collision $\overline{\nu}_c$ frequencies of both the population-average and E_f holes.

The classical Drude model gives:

$$\tilde{\varepsilon} = \varepsilon_1 - i\varepsilon_2 = 1 - \overline{\nu}_p{}^2(\overline{\nu}^{\,2} + \overline{\nu}_c{}^2)^{-1} - i \cdot \overline{\nu}_p{}^2\overline{\nu}_c\overline{\nu}^{-1}(\overline{\nu}^{\,2} + \overline{\nu}_c{}^2)^{-1},$$

but localization effects add a correction to ε_2 which in first order is:[21,22]

$$\varepsilon_2' = \varepsilon_2(1 - (1 - \sqrt{3\overline{\nu}/\overline{\nu}_c})(\Lambda)^{-2}),$$

where Λ is a dimensionless localization parameter ≈ 1–2 in disordered OSCs. The absorptivity and conductivity spectra are related by $\alpha = 2k\kappa$ and $\sigma = \omega\varepsilon_o\varepsilon_2'$, where k and ω are the wavevectors and angular frequency respectively, and $\kappa = \mathrm{Im}(\sqrt{\tilde{\varepsilon}})$. Thus three parameters completely specify $\alpha(\overline{\nu})$ and $\sigma(\overline{\nu})$ in this simple model. We constrained $\overline{\nu}_p$ and Λ to be the same in both modulated and unmodulated spectra, and found that the set of parameters: $\overline{\nu}_p$ = 7000 cm^{-1}, Λ = 1.6, and $\overline{\nu}_c$ = 6000 cm^{-1} for the population average, and 800 cm^{-1} at E_f [error ±10%], gives excellent overall fits.

The parameters found for the population average are in fact similar to those obtained elsewhere by fitting conductivity spectra of similarly heavily-doped conducting polymers,[6,22] except for a slight redshift of $\overline{\nu}_p$ here due to the dilution effects of PSSH. The predicted $\alpha(\overline{\nu})$ and σ_{dc} are consistent with experiment, after taking into account this dilution effect. Therefore, fitting to the modified Drude model reveals that the E_f holes are far more weakly scattered than the population average by a factor of seven.

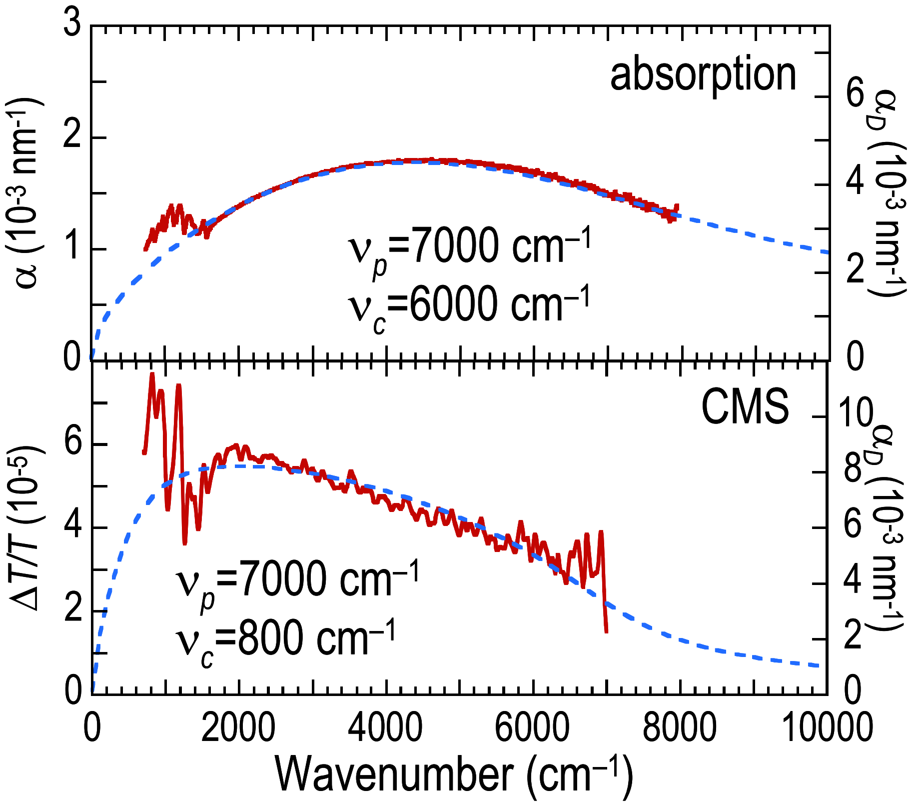

Figure 3.8 Experimental spectra (solid line, left axis) and computed spectra (dotted line, right axis) from the Drude model modified for weak localization.

Therefore it can be firmly established from the Drude-like line shape of the electronic transition, and phonon softening of the IRAV modes that holes at the Fermi level are significantly more delocalized than the population average, even in such a degenerately-doped disordered conducting polymer as PEDT:PSSH. The extent of delocalization appears to be similar to that of the carriers field-induced at far lower concentrations in highly-ordered and undoped regioregular P3HT,[23] and significantly more so than that in a non-regioregular polymer.[24] Therefore it appears that interchain interaction can successfully drive the formation of the polaron band at sufficiently high charge carrier densities, even in the presence of Coulomb disorder. The interaction bandwidth *B* must consequently exceed the Hubbard energy *2U*

(Figure 3.9), so that the E_f holes can reside in an energy continuum with zero gap. The lower bound for the estimate of U is ca. 0.55 eV from the observed electronic transition in model oligomers.[20] The alternative picture of a random Coulomb potential $V_{ran} >> (2U - B)$ with $B << 2U$ predicts an optical gap in the electronic transition of the E_f holes, and so can be ruled out as the primary cause of the finite $D(E_f)$.

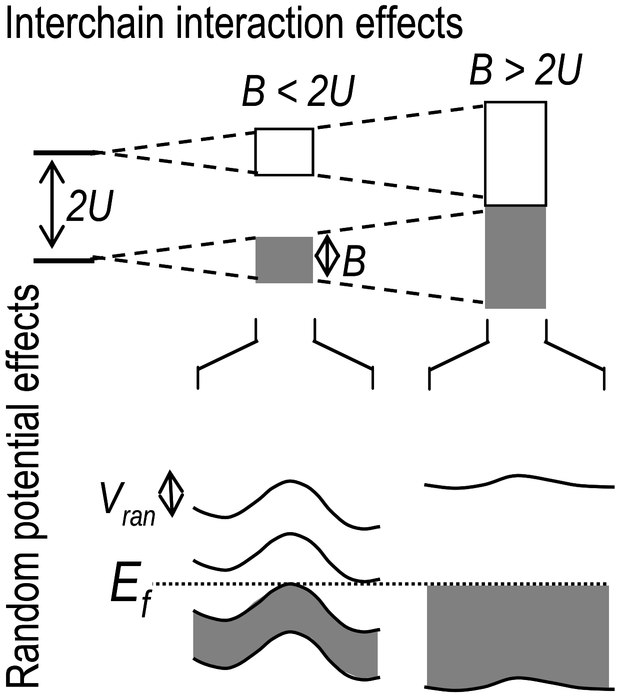

Figure 3.9 Schematic of the effects of interchain interaction (top) and random potential (bottom) on the energy of carriers in doped conducting polymers, both leading to finite $D(E_f)$, but with different optical gaps. Effects of random potential are drawn to be less severe for delocalized carriers. These energy levels correspond to one-electron states, so the classical “half-filled” polaron band is obtained only when the upper band meets the lower band.

3.4 Conclusion

We have developed a sensitive interferogram-modulated FT-CMS technique, with which we provided direct spectroscopic evidence for significantly enhanced charge-carrier delocalization at the Fermi level despite severe disorder in a heavily-doped organic semiconductor. The weak scattering provides support for a model of strong interchain interactions between the carriers. Nevertheless, some electron–phonon coupling remains and complete delocalization has not occurred.

3.5 References

1 Apperloo, J. J. *et al.* Optical and redox properties of a series of 3,4-ethylenedioxythiophene oligomers. *Chem. Eur. J.* 8, 2384-2396 (2002).

2 van Haare, J. A. E. H. *et al.* Redox states of long oligothiophenes: two polarons on a single chain. *Chem. Eur. J.* 4, 1509-1522 (1998).

3 Lögdlund, M., Lazzaroni, R., Stafström, S. & Salaneck, W. R. Direct observation of charge-induced pi-electronic structural changes in a conjugated polymer. *Phys. Rev. Lett.* 63, 1841-1844 (1989).

4 Mele, E. J. & Rice, M. J. Semiconductor-metal transition in doped polyacetylene. *Phys. Rev. B* 23, 5397-5411 (1981).

5 Kivelson, S. & Heeger, A. J. First-order transition to a metallic state in polyacetylene: a strong-coupling polaronic metal. *Phys. Rev. Lett.* 55, 308-311 (1985).

6 Lee, K. *et al.* Metallic transport in polyaniline. *Nature* 441, 65-68 (2006).

7 Sirringhaus, H. *et al.* Two-dimensional charge transport in self-organized, high-mobility conjugated polymers. *Nature* 401, 685-688 (1999).

8 Österbacka, R., Jiang, X. M., An, C. P., Horovitz, B. & Vardeny, Z. V. Photoinduced quantum interference antiresonances in pi-conjugated polymers. *Phys. Rev. Lett.* 88, 226401:226401-226404 (2002).

9 Groenendaal, L. B., Jonas, F., Freitag, D., Pielartzik, H. & Reynolds, J. R. Poly(3,4-ethylenedioxythiophene) and Its derivatives: past, present, and future. *Adv. Mater.* 12, 481-494 (2000).

10 Png, R. Q. *et al.* Electromigration of the conducting polymer in organic semiconductor devices and its stabilization by crosslinking. *Appl. Phys. Lett.* 91, 013511 (2007).

11 Zade, S. S. & Bendikov, M. Theoretical study of long oligothiophene polycations as a model for doped polythiophene. *J. Phys. Chem. C* 111, 10662-10672 (2007).

12 Yokonuma, N., Furukawa, Y., Tasumi, M., Kuroda, M. & Nakayama, J. Electronic absorption and Raman studies of tetrafluoroborate-doped polythiophene based on the spectra of the radical cation and dication of alpha-sexithiophene. *Chem. Phys. Lett.* 255, 431-436 (1996).

13 Griffiths, P. R., de Haseth, J. A. *Fourier transform infrared spectrometry* (Wiley, New York, 1986).

14 Jiang, E. Y. *Principles, experiments and applications*. (Thermo Electron Technical Note).

15 Kvarnström, C., Neugebauer, H., Ivaska, A. & Sariciftci, N. S. Vibrational signatures of electrochemical p- and n-doping of poly(3,4-ethylenedioxythiophene) films: an in-situ attenuated total reflection Fourier transform infrared (ATR-FTIR) study. *J. Mol. Struct.* 521, 271-277 (2000).

16 Horovitz, B. Infrared activity of Peierls systems and application to polyacetylene. *Solid State Commun.* 41, 729-734 (1982).

17 Lopez Navarrete, J. T. & Zerbi, G. Lattice dynamics and vibrational spectra of polythiophene. II: Effective coordinate theory, doping induced, and phoexcited spectra. *J. Chem. Phys.* 94, 965-970 (1991).

18 Crispin, X. *et al.* Conductivity, morphology, interfacial chemistry, and stability of poly(3,4-ethylenedioxythiophene)-poly(styrenesulfonate): A photoelectron spectroscopy study. *J. Polym. Sci. B: Polym. Phys.* 41, 2561-2583 (2003).

19 Chia, P. J. *et al.* Injection-induced de-doping in a conducting polymer during device operation: asymmetry in the hole injection and extraction rates. *Adv. Mater.* 19, 4202-4207 (2007).

20 Apperloo, J. J. *et al.* Optical and redox properties of a series of 3,4-ethylenedioxythiophene oligomers. *Chem. Eur. J.* 8, 2384-2396 (2002).

21 Mott, N. F. & Davis, E. A. *Electronic processes in non-crystalline materials*. 2nd edn, (Clarendon Press, Oxford, England, 1979).

22 Chang, Y., Lee, K., Kiebooms, R., Aleshin, A. & Heeger, A. J. Reflectance of conducting poly(3,4-ethylenedioxythiophene). *Synth. Met.* 105, 203-206 (1999).

23 Brown, P. J., Sirringhaus, H., Harrison, M., Shkunov, M. & Friend, R. H. Optical spectroscopy of field-induced charge in self-organized high mobility poly(3-hexylthiophene). *Physical Review B* 63, 125204- 125201-125211 (2001).

24 Ziemelis, K. E. *et al.* Optical spectroscopy of field-induced charge in poly(3-hexyl thienylene) metal-insulator-semiconductor structures: evidence for polarons. *Phys. Rev. Lett.* 66, 2231-2234 (1991).

Chapter 4. Influence of dielectric surface modification on morphology and charge carrier properties in rr-P3HT thin films

In this chapter, we present evidence for the presence of a hitherto unknown polymer OSC transition layer at the dielectric interface that has large impact on the μ_{FET} of the devices. This transition layer which is formed by polymer OSC adsorption, rather than switching of the bulk π-stacking orientation, resolves the long-standing mystery of how dielectric surfaces can so markedly influence the μ_{FET} of the charge-carriers even amongst films prepared under identical conditions. We show from height histogram data collected by atomic force microscopy of ultrathin films the occurrence of a significant population of face-on (i.e., lying-down) rr-P3HT chains which decreases significantly across the series: trimethylsilyl > trifluromethyl > trimethyl ≈ hydroxyl-terminated SiO_2, although the bulk and top surface organization of the chains in thicker films are identical. Concomitantly, charge-modulation spectroscopy in both the infrared and optical spectral regions reveals that the face-on transition layer does not support delocalized field-induced polarons unlike the edge-on π-stacked layer. Finally, detailed modeling of the μ_{FET}–temperature–hole density surface of the FETs, reveals that face-on transition layer has a broader transport density-of-states width, and the Fermi level lies further away from the transport level.

4.1 Introduction

Solution-processable organic FETs are reaching new levels of performance with μ_{FET} values (>0.5 $cm^2\ V^{-1}\ s^{-1}$) that surpasses those of amorphous Si.[1-4] A large part of this effort has presently centered on developing new materials for “standard” prototyping FET configurations. However it is increasingly important to understand the processing and morphology aspects and how these influence materials performance, because manufacturing processes can deviate significantly (for example, use of inkjet printing) from the spin-casting often used for prototyping. Amongst these materials, rr-P3HT is a particularly important model of a π-stacked semicrystalline polymer OSC that has been extensively studied for organic FET and solar cell applications.

The choice of solvents[5,6], deposition method[5,7-9], molecular weight[10-14] variation and structural regio-regularity[9] on the morphology and μ_{FET} of the rr-P3HT FETs has already been widely studied in the literature. Apart from optimization of film morphology and crystallinity, it is also important to understand their interaction with the dielectric surface because organic FETs will be manufactured on substrates that are different from those used for prototyping. The influence of the dielectric constant on μ_{FET} has been investigated,[15,16] but its potential in “templating” a transition “wetting” layer appears largely to have escaped notice. Therefore while it has been known that dielectric surface modifications can induce large variations in the observed μ_{FET} of rr-P3HT FETs, the mechanism has not yet been clarified. Any change in μ_{FET} is almost invariably attributed to a switch between edge-on and face-on π-stacking of the polymer OSC at the interface, but how the molecular interaction could turn the π-stacks on their sides, and other puzzling features, including the large disparity between μ_{FETs} obtained on nominally alkylterminated surfaces (such as hexamethyldisilazane-, octatrichlorosilane and octadecyltrichlorosilane-treated surfaces), and the non-monotonic dependence of μ_{FET} on surface energy[17-19] are not addressed.

In this chapter, we study the properties of rr-P3HT thin films in bottom-gate, bottom-contact FETs with which the SiO2/p^{++}-Si surfaces have been chemically modified prior to polymer deposition. The controlled modification of the surfaces of these SiO_2 gate dielectrics by well-established self-assembled monolayers that are only 1 – 3 nm thick permits one to study the influence of the surface termination itself on the intrinsic charge-transport characteristics of the adjacent field-induced channel, substantially free from variations in the effective dielectric constant and polarization effects which may otherwise also influence polaron transport.[16]

We select the following surface treatments (Figure 4.1) : oxygen-plasma (OP) which generates a hydrophilic surface (H_2O contact angles: advancing θ_a = 18°; receding θ_r = 4°); and three SAM treatments which generate hydrophobic surfaces: octadecyltrichlorosilane (OTS) end-capped with hexamethyldisilazane (HMDS) (θ_a = 105°; θ_r = 103°), HMDS alone, (θ_a = 87°; θ_r = 76°); and 1*H*,1*H*,2*H*,2*H*-perfluorodecyldimethylchlorosilane (PDS) (θ_a = 90°; θ_r = 80°). The OP surface gives θ_a and θ_r very similar to those of freshly oxygen-plasma-treated plastic substrates; while both HMDS and PDS surfaces give similar H_2O contact angles and hystereses as those on a variety of clean plastic substrates. However, the HMDS and PDS surfaces exhibit different relative contributions by the dispersion and polar components to the surface energy, with the PDS surface being more polar because of the large CF_2 bond dipole moment.[20] The OTS treatment produces a close-packed methyl-terminated surface for reference.[21,22]

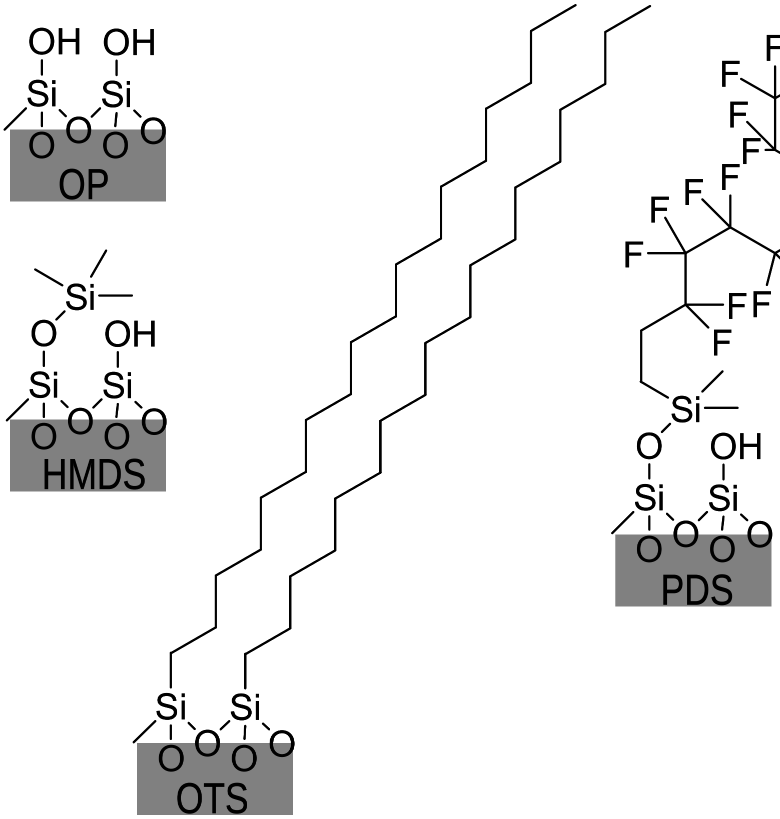

Figure 4.1 Schematic of the SiO_2/Si surface after surface-treatment with oxygen-plasma, hexamethyldisilazane (HMDS), octadecyltrichlorosilane (OTS) and 1,1,2,2-4H-perfluorodecyldimethylchlorosilane (PDS).

4.2 Experimental methods

4.2.1 Surface modification

Thermal-SiO_2/p^{++}-Si substrates were photo-lithographically patterned with Au source-drain arrays of various channel lengths. These were then cleaned by oxygen plasma (200 W, 300 mbar; 10 min). For the OTS- and PDS-modification, these wafers were treated with OTS and PDS respectively in the solution phase (0.1 mM in HPLC-grade toluene, 25ºC; 2 h) in a N_2-purged glovebag to form a close-packed monolayer. Conducting the growth in the glovebag is crucial to limit the amount of moisture available for hydrolysis of the trichlorosilyl group to avoid the formation of multilayers.[21,23] The substrates were then rinsed thrice with clean toluene and annealed at 120°C (10 min, hotplate in the glovebag) to promote the covalent bonding of the SAM to the SiO_2 surface. We routinely established the quality of these SAM by spectroscopic ellipsometry (2.8-nm for OTS and 1.4-nm for PDS) and contact-angle measurements. The OTS-modified surface was then further treated with HMDS (120°C, 10min) to terminate all the unreacted silanol groups. For the HMDS-modification, the substrates were placed in a covered petri dish saturated with HMDS vapor at 120°C (10 min, hotplate).

4.2.2 Atomic force microscopy

Atomic force microscopy (AFM) was performed in air with a Dimension 3000 Nanoscope operating on a tapping mode. Silicon cantilevers are used and 1 x 1 μm areas are scanned using 256 lines at 1 Hz scan speed.

4.2.3 Ultraviolet – visible Spectroscopy

UV-Vis absorption spectra were collected using a diode-array UV-Vis spectrograph (DW 1024, Ocean Optics). Thin and ultrathin rr-P3HT films were spin-cast at 3000 rpm from 9 mg mL^{-1} and 0.36 mg mL^{-1} rr-P3HT solutions respectively on SC1-cleaned and surface-modified substrates.

4.2.4 Near-edge X-ray absorption fine structure spectroscopy

Total-electron-yield near-edge X-ray absorption fine structure spectra were collected at the Singapore Synchrotron Light Source (SSLS) on the SINS beamline fitted with a dragon monochromator using linearly-polarized x-rays ($P \geqslant 0.97$) with energy resolution of 0.6eV at the C_{1s} edge, and calibrated using carbon dips in the mirror currents. Energy precision is ± 0.05 eV, and accuracy is ± 0.1 eV. The spectra were normalized to the mirror current using sputter-cleaned gold as reference.

Samples were prepared by spinning rr-P3HT from chlorobenzene solution on pre-treated SiO_2/Si substrates. The top interfaces were studied directly, while the bottom was exposed by lifting off these films with conductive copper tape at light force without deformation. For each film, the spectra were collected at four angles (25°, 35°, 55° and 90°), with respect to the sample surface. Between each scan, the sample is translated 0.75 mm to a pristine spot for data collection to avoid any complication due to X-ray damage.

4.2.5 Variable temperature field-effect transistors characterization

Variable-temperature FET measurements were carried out in a LakeShore TTP4 Probe Station kept at under 10^{-6} mbar and recorded by the Keithley 4200-SCS semiconductor parameter analyzer. FETs were fabricated in a similar way with photo-lithographically defined 20 μm channel length and 225 mm channel width.

4.2.6 Charge modulation spectroscopy in mid-IR to visible region

The devices for CMS were based on bottom-gate field-effect transistor. Interdigitated Cr/Au source- drain electrode array (channel length L = 20 µm; width of 225 mm) was fabricated by photolithography on 200 nm thermal SiO_2/p^{++}-Si. The interdigitated area is approximately 3 x 3 mm. The fabricated substrates were subjected to the respective SAM treatment before an approximately 50 nm- thick layer of rr-P3HT was spin-cast from chlorobenzene solution. The device was mounted in a closed-cycle helium cryostat (Janis CCS-100/202) with KBr windows and evacuated to 10^{-6} mbar for the measurements.

The helium cryostat was then mounted in a N_2-purged spectrometer (Nicolet 8700 FT-IR) where the transmitted light intensity was measured with a liquid N_2-cooled mercury cadmium telluride detector. The output voltage from a lock-in amplifier (SR 830) at 170 Hz was amplified by a dual channel high-voltage amplifier (Avtech) and superimposed on a dc bias before injecting into the device. A reference spectrum was first collected by rapid scan. After which, the in-phase and quadrature interferograms were constructed by step-scan mirror displacements and the detector response at each step was then demodulated by the lock-in amplifier at the reference frequency of 170 Hz before Fourier transformed to their respective spectra. The $\delta T/T$ spectra were obtained by normalizing the in-phase spectra to the reference spectrum. The schematic of the experimental setup is shown in Figure 3.4.

CMS spectra in the visible region were collected using a home-built optics rig (see Figure 4.2). A sinusoidal ac voltage superimposed on a dc bias was applied across the device as before at 170 Hz. Monochromatic light was incident on the device and its reflection was collected by mirror optics onto a photodiode with transimpedance gain of 10^7. The voltage output was demodulated by a lock-in amplifier phase-locked to the ac voltage at 170 Hz.

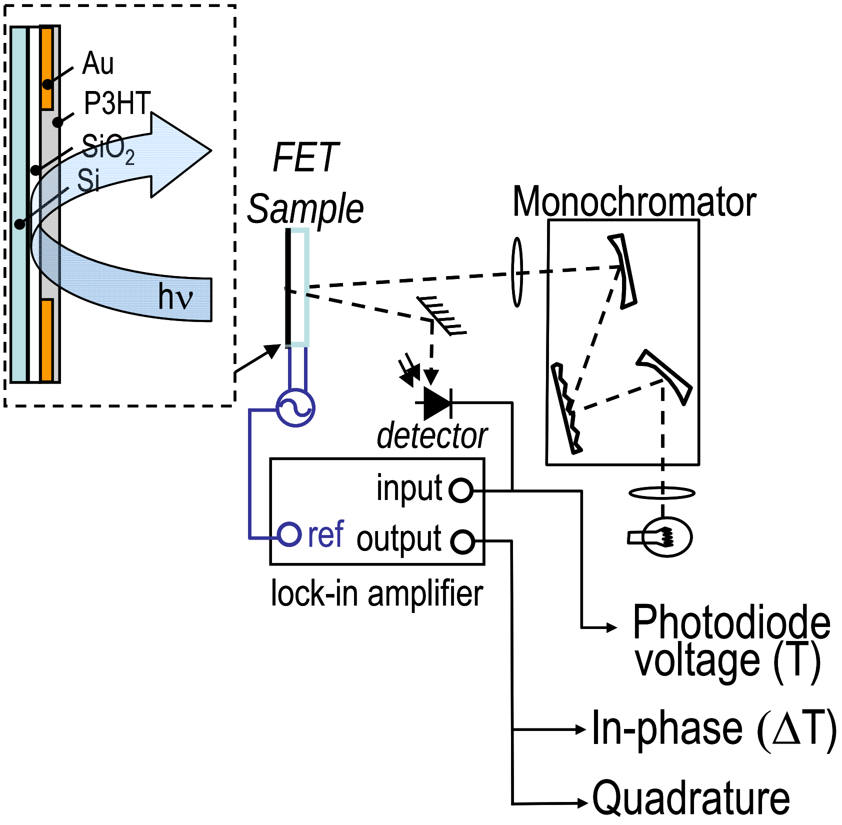

Figure 4.2 Experimental setup for charge modulation spectroscopy in the visible spectra range.

4.3 Results and discussion

4.3.1 Overview of field-induced transport characteristics

Figure 4.3 (left panel) shows the temperature dependence of the linear-regime μ_{FET} extracted from transfer characteristics of the FETs according to

$$\mu_{FET} = \frac{L}{C_{ox}W} \cdot \frac{1}{V_d} \cdot \frac{dI_s}{dV_g}$$

where C_{ox} is the capacitance of the gate dielectric, w the channel width, L the channel length, V_d the drain voltage and V_g the gate voltage, for the set of films fabricated on OP-, OTS-, PDS- and HMDS-treated substrates. This gives the mobility of an incremental carrier density accumulated into the channel. The FETs had long channel lengths (20 μm) to suppress contact resistance effects. Because μ_{FET} is generally dispersive (i.e., varies with carrier density σ), we evaluated this equation at constant V_g of –60 V, corresponding to σ of 4.3 x 10^{12} hole cm^{-2} which is much higher than that trapped particularly at low temperatures, and at a relatively large V_d of –40 V to avoid contact resistance effects. The FET characteristics in both output and transfer plots are well-behaved over the entire temperature with only a small hysteresis above room temperature (see Figure 4.4 for example for the OP device), for all the surface modifications investigated, in contrast to literature reports which suggests strong charge trapping in particular by the perfluoroalkyl SAM with large attendant V_g shifts and sweep hysteresis.[17,24] The careful formation of high-quality SAM layers here (in particular the termination of excess hydrolyzed silanol groups in OTS with HMDS, and the use of mono-dentate PDS) has alleviated this undesired effect, and the μ_{FET} values measured here are reliable.

The results show that μ_{FET}–T curves vary with dielectric surface termination as OP > OTS > PDS >> HMDS with a room-temperature μ_{FET} in OP devices (0.04 cm^2 V^{-1} s^{-1}) two orders of magnitude higher than in HMDS devices (4 x 10^{-4} cm^2 V^{-1} s^{-1}). These results are highly reproducible with repeat device fabrication and measurements.

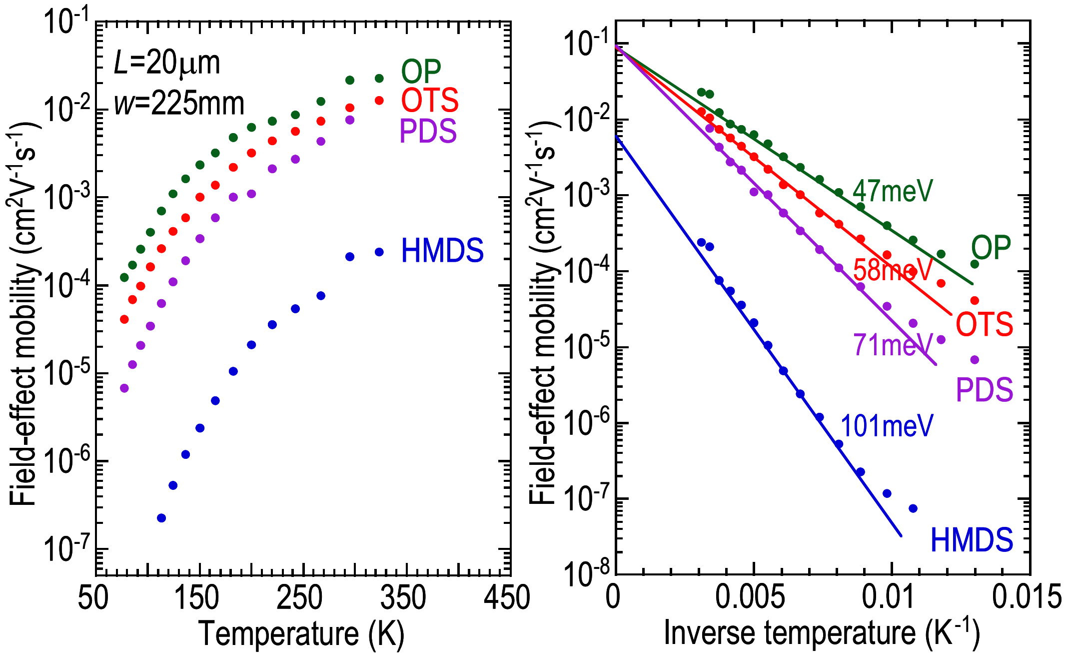

Figure 4.3 Left panel: Field-effect hole mobilities of rr-P3HT transistors fabricated on different modified SiO_2/Si surfaces. The mobilities were extracted from the linear regime at V_g = -60V and V_d = -40V. Right panel: Arrhenius plot of the four corresponding devices. Symbols are experimental data; lines are best-fit lines from which the apparent field-effect mobility activation energy is derived. The activation energy increases in the order of O_2 < OTS < PDS << HMDS.

The Arrhenius representation of the data is shown in Figure 4.3 (right panel). The different devices exhibit nearly similar thermally activated behavior from 77 to 323 K. The apparent Arrhenius activation energy evaluated at the same 4.3 x 10^{12} hole cm^{-2}, given by

$$E_a = -k_B \frac{\partial \ln \mu_{FET}}{\partial (1/T)},$$

where k_B is the Boltzmann constant, varies from 47 meV for OP devices to 101 meV for HMDS devices. A small jump in μ_{FET} occurs around room temperature followed by a decline due to a polymorphic phase transition (indicated by differential scanning calorimetry) overlapping with possibly other transitions.[25] The E_a of OP and OTS devices here are lower but the HMDS device similar to those reported elsewhere.[9,14] This suggests that the width of the transport density-of-states (DOS) in the OP and OTS devices is even smaller and hence the conduction channel is more ordered here than achieved elsewhere.

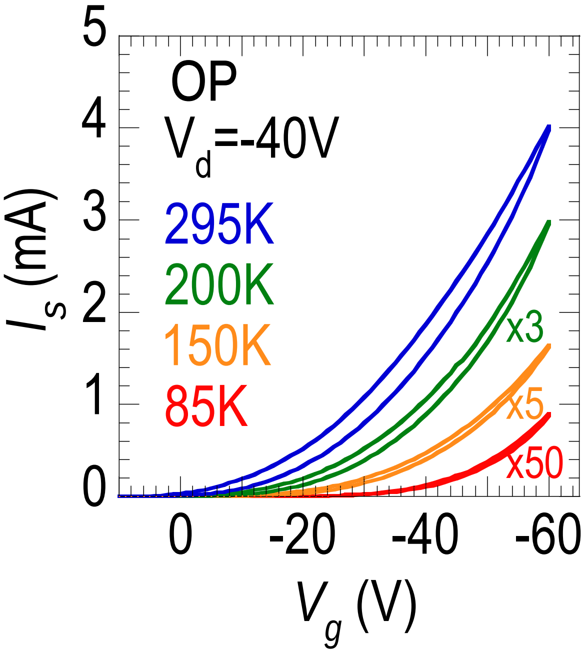

Figure 4.4 Transfer curves of a device fabricated on OP-treated substrate at T = 85K, 150K, 200K and 295K.

4.3.2 Structural characterization

Structural information of the "bulk" in rr-P3HT films

The UV-Vis absorption spectra measured in transmission for 20 nm-thick films of rr-P3HT spin-cast on the various surface-modified substrates are shown in Figure 4.5.

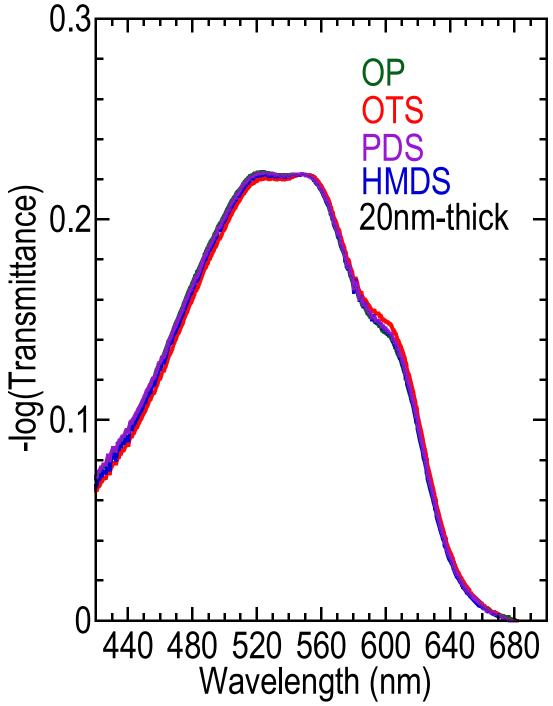

Figure 4.5 UV-Vis absorption spectra of 20nm-thick rr-P3HT spin-cast from 9 mg mL^{-1} solution on OP, OTS, PDS and HMDS -treated glass substrates.

As expected, these "bulk" spectra are practically identical showing vibronic features at 603 (shoulder, 2.06), 557 (peak, 2.23) and 520 nm (2.38 eV). These have been assigned to the 0–0, 0–1 and 0–2 vibronic transitions coupled by an "average" 0.16 eV phonon related to the benzenoid→quinoid bond-alternation inversion vibration. It has been established that deposition solvent,[6] solvent evaporation rate[26,27] and deposition method[8] can critically affect polymer chain morphology and the resultant spectra. This observation is supported by UPS spectra of rr-P3HT films prepared from different solution concentrations where the features are independent of the film thicknesses.[28] The identical spectra obtained here attest to the excellent control over solution history and the film fabrication process. The atomic force microscopy (AFM) images of the top surface are also substantially identical (Figure 4.6) showing the expected nodular morphology.

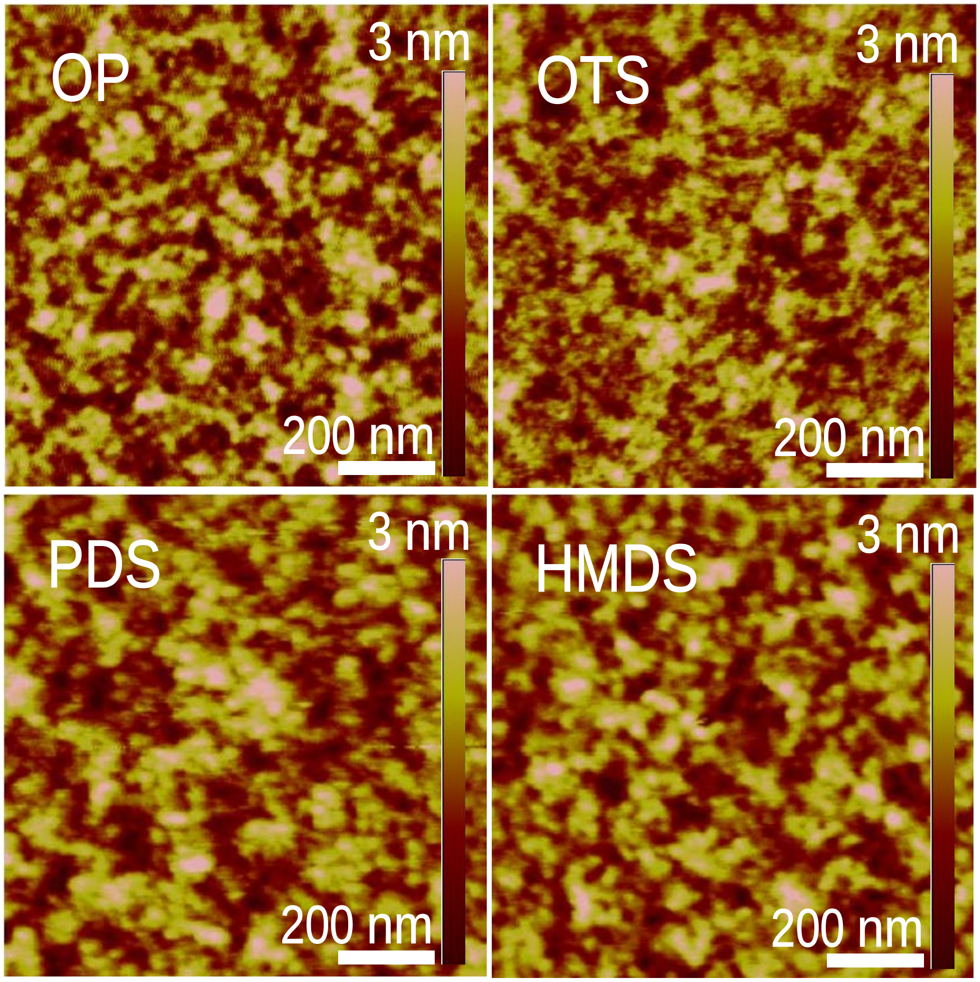

Figure 4.6 AFM images of 20 nm-thick rrP3HT films on OP, OTS, PDS and HMDS-treated Si substrates.

Ultra-thin rr-P3HT film

To probe the polymer film morphology in the frontier monolayer at the substrate interface, we also fabricated 2.0-nm-thick ultrathin films (verified by UV-Vis spectroscopy, Figure 4.7) by spinning very dilute 0.36 mg mL^{-1} solution on the various surface-modified substrates in the same way as the thicker device films, and imaged the monolayer morphology using atomic force microscopy (AFM). This will reveal the existence of transition layer if any which has a different orientation and packing of the polymer chains from the bulk. Such a layer would be determined strongly by the van der Waals energetics of the surface, assuming (pseudo)equilibrium is reached.

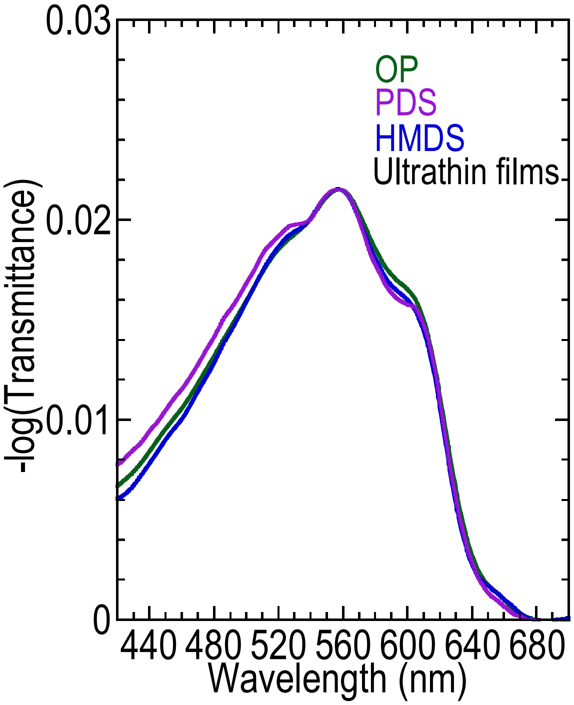

Figure 4.7 UV-Vis absorption spectra of ultrathin rr-P3HT spin-cast from 0.36 mg mL^{-1} solution on OP, PDS and HMDS-treated substrates.

The most striking observation here is that these monolayer films are better-ordered than in the bulk, as evidenced by the increase in the intensity of the 0–0, and decrease in intensity of the 0–2 relative to the 0–1 band.[29]

The AFM results obtained are remarkable (Figure 4.8). Unlike the usual top-surface topography of thicker rrP3HT films which show nodular morphology on the tens of nm length scale and independent of the underlying substrate, these ultrathin films yield well-defined terraces with a step height d_{eo} of 1.7 nm which corresponds to the thickness of the in-plane π-stacks in the (100) direction with edge-on orientation of the polymer chains, and is clearly evidenced by the two-color contrast in the images. This film organization at the interface is thus similar to that routinely observed on both thick and ultrathin PBTTT films.[25,30] However other step heights are also found, in particular at d_{fo} of 0.4 nm and its multiples, which corresponds to the thickness of a face-on oriented rrP3HT chain. These can be clearly seen as shallow steps in the "valley" between adjacent in-plane π-stacked lamellae, and also over parts of the lamellae, but its occurrence depends strongly on surface modification of the substrate.

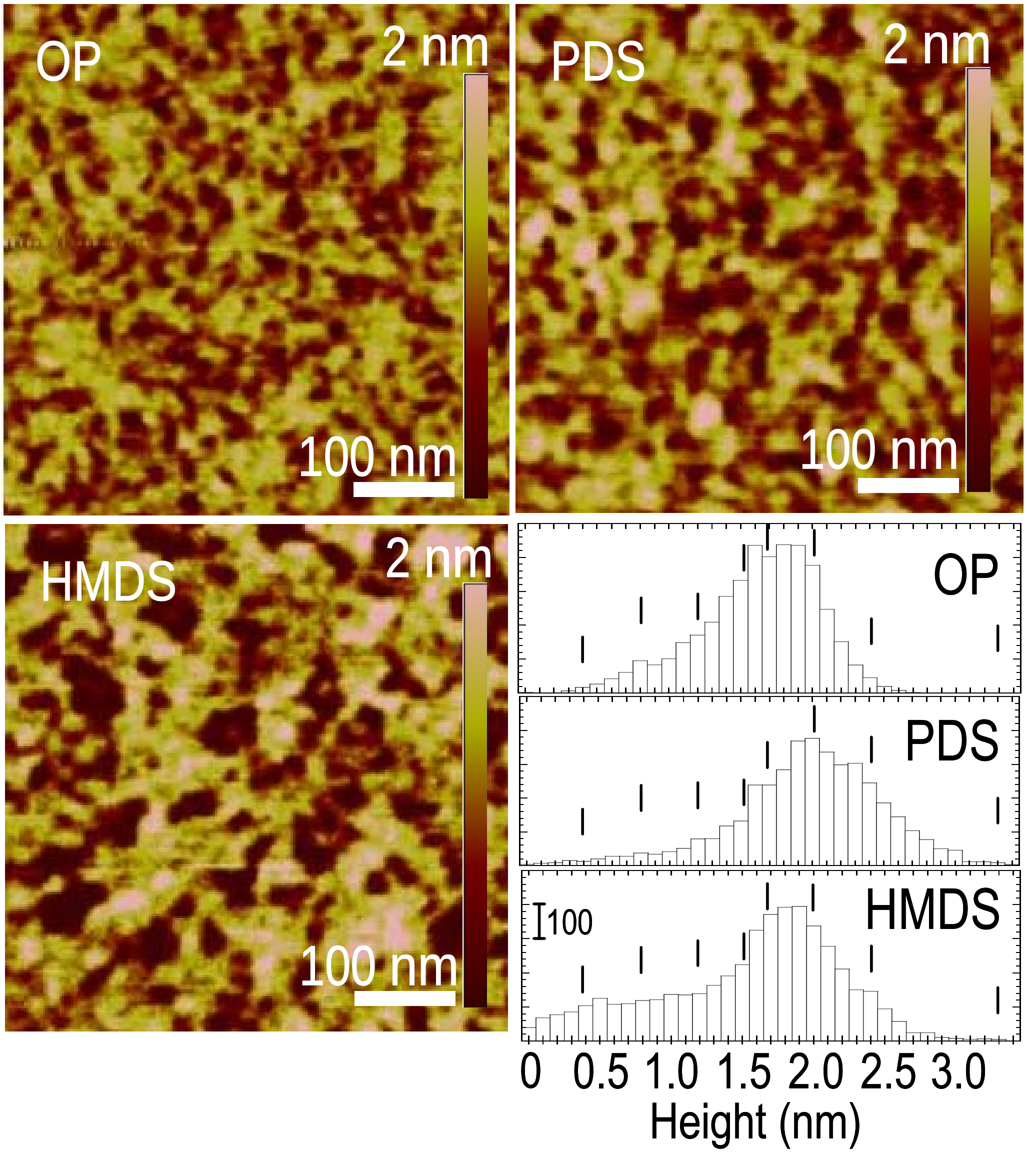

Figure 4.8 AFM images of ultrathin rrP3HT films on OP, PDS and HMDS-treated SiO$_2$/Si substrates and their corresponding height-distribution histograms. The height corresponding to the lying-down fraction, lamellar stack and their multiples are marked on the histograms.

To quantify this population, we reconstructed the AFM height distribution histogram $P(z)$ by carefully locating the true zero of the substrate level in the image and then correcting the height and slope of the line scans line-by-line by aligning the stepped profiles. This overcomes the data smearing by the usual image processing softwares that remove baseline shifts using best-fit lines. The results (histogram in Figure 4.8) reveal that indeed the dominant height mode is d_{eo}, but depending on the surface, there can also be significant populations at d_{fo} and its multiples $n \cdot d_{fo}$ (where n is a positive integer) and also at $d_{eo} + n \cdot d_{fo}$. The latter is interpreted as in-plane π-stacked lamellae sitting on one or two layers of face-on oriented chains. These d_{eo} steps are clearly evident within each line scan, and so are not due to imaging or data processing artifacts. No bilayer lamellae which would occur at $2d_{eo}$ of 3.4 nm were observed here, because the average thickness of the film cast was only 2 nm to probe the first monolayer.

The $P(z)$ histogram shows that HMDS surface has the largest fraction of film thicknesses distributed in the $n \cdot d_{fo}$ and $d_{eo} + n \cdot d_{fo}$ modes. To quantify this, we modeled the $P(z)$ distribution as a sum of Gaussians, $P(z) = \Gamma(d_{eo}) + \Gamma(n \cdot d_{fo}) + \Gamma(d_{eo} + n \cdot d_{fo})$, where $\Gamma(d)$ is the Gaussian function centered at d. The first term represents the contribution from areas covered with edge-on chains in π-stacked lamellae, the second term from areas covered with one or more layers of face-on chains, and the third term from areas covered with one or more layers of presumably buried face-on chains overlaid with edge-on chains in π-stacked lamellae. The results reveal that about three-quarters of the HMDS surface but only one-half of the PDS surface and one-third of the OP surface is covered by the face-on population. The face-on population is due to adsorption of flat rr-P3HT chains on these surfaces. It is characterized by small *n*, which rules out the vertical deposition of π-stacks. Furthermore this interface monolayer morphology does not persist to the top surfaces of thicker rrP3HT films, which all have the same nodular morphology, and is therefore localized. In addition, the usually large contribution of the third term on the PDS surface indicates that the face-on chains there are predominantly covered with in-plane lamellae. Therefore it is clear that these face-on monolayers are a transition or wetting layer arising from adsorption of a flat conformation of rr-P3HT from the solution onto the surface before the deposition of the π-stacks. This also explains a curious observation: a wait time on the order of minutes is required for successful film spinning on the PDS but not on OP or HMDS surface, which suggests its wetting layer takes a longer time to develop. For OTS surfaces, the required wait time is even longer, and so for typical film preparation conditions, we expect the wetting layer to be least well developed.

Interfacial packing probed by NEXAFS

We obtained independent evidence for the existence of this wetting layer also in thicker spin-cast films by measuring the absorption dichroic ratio of the thiophene $C_{1s} \rightarrow 1\pi^*$ transition at 285 eV in near-edge X-ray absorption fine structure (NEXAFS) spectroscopy which gives the average orientation of the polymer chains in the frontier layers.[8,27] This experiment was performed on two of the surfaces OTS and PDS which can be delaminated at near zero force.

A linearly polarized X-ray is directed onto the sample at a defined angle θ, measured with respect to the normal of the sample plane. Due to the strong directional character of the molecular orbitals, the intensity of the transition from the C_{1s} to an unoccupied $1\pi^*$ orbital is dependent on the incidence angle θ can thus can be used to determine the orientation of π-

orbital and molecular orientation of thiophene ring α. The definition of various angles is illustrated in Figure 4.9.

Figure 4.10 show the total-electron-yield $C_{1s}\rightarrow 1\pi^*$ spectra measured at the SINS beamline of the Singapore Synchrotron Light Source for both the top and bottom (delaminated) surfaces of 50-nm-thick rrP3HT films spin-cast onto the OTS- or PDS-modified SiO_2/ Si substrates. The bottom interfaces were delaminated by carefully lifting the films with conductive copper tape without causing shear or deformation of the polymer chains there.[8,27] In this way it is possible to probe the frontier chain organization for both the top and bottom film interfaces in the same type of sample. Previous measurements of the total electron yield suggests that the sampling depth is only 3.5 nm for this technique, and so the information obtained pertains to the topmost few monolayers that are directly related to injection and FET transport.[31]

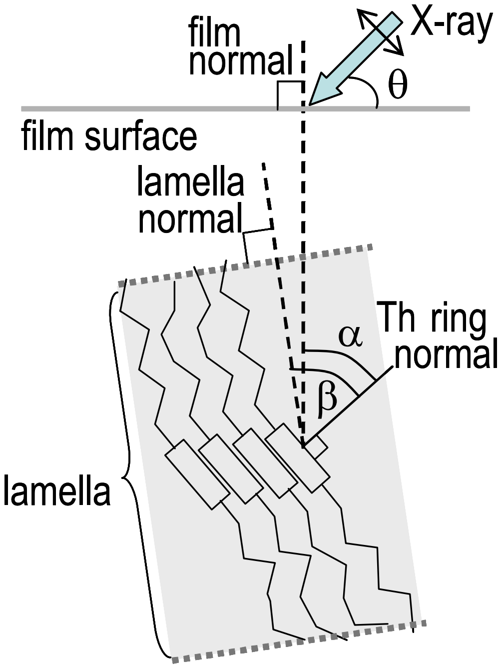

Figure 4.9 Diagram illustrating the definition of angles θ, α and β.

The average orientation angle of the thiophene rings $\langle\alpha\rangle_{Th}$ (defined in Figure 4.9) was determined by standard dichroic analysis[32] of the polarization-angle dependence of the photoemission yield for the $C_{1s} \rightarrow 1\pi^*$ transition at 285 eV as follows:

$$I \approx \left[1 + 0.5\left(3\cos^2\theta - 1\right)\left(3\cos^2\alpha - 1\right)\right]$$

This dependence of transition intensity on θ is shown in Figure 4.11 for the films on OTS- and PDS-substrates. The results show that the air interface has $\langle\alpha\rangle_{Th} = 68 \pm 1°$, independent of the substrate, as reported previously for rr-P3HT films.[8,27] However the substrate interface differs significantly when spin-cast on OTS ($\langle\alpha\rangle_{Th} = 63°$) or PDS (55º) surfaces. Since the roll angle β of the Th rings within the lamellae (Figure 4.9) is ≈ 70º,[8] the $\langle\alpha\rangle_{Th}$ of the air interface exhibits nearly complete parallel lamellae orientation with in-plane π-stacks (*ca*. 95%), but the bottom interfaces exhibit significantly mixed orientations. The $\langle\alpha\rangle_{Th}$ for the PDS interface suggests one-quarter of the polymer chains within the probe depth is in the face-on orientation, which broadly agrees with the AFM results, while that for the OTS interface is only ≈ 10%.

The results thus provide strong evidence for the existence of a transition layer that varies markedly with the surface of the dielectric. A schematic of the two limiting cases of transition layers at the interface revealed by these results is shown in Figure 4.12.

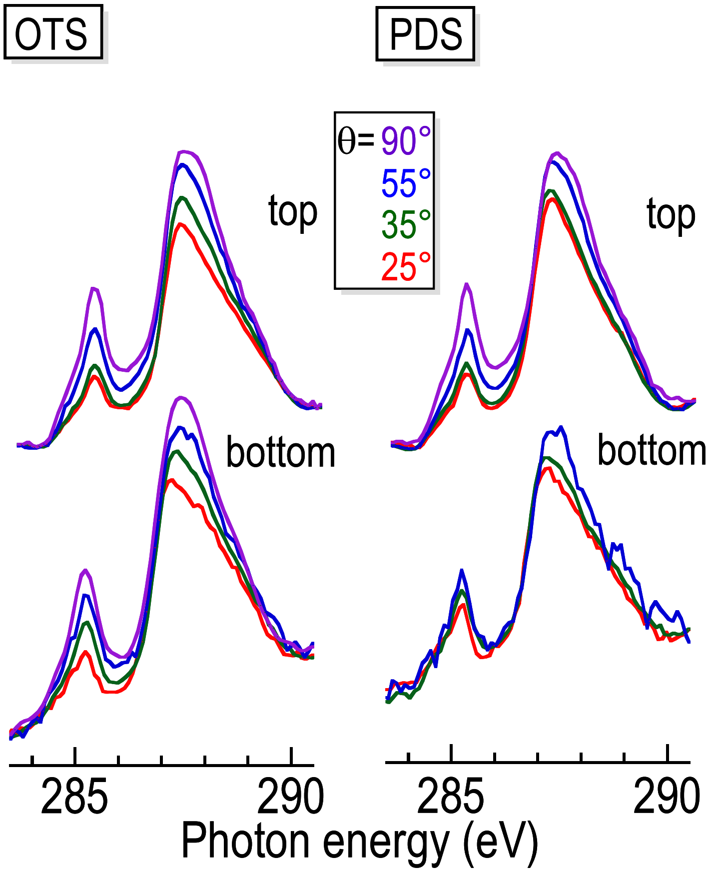

Figure 4.10 Total-electron-yield- near-edge X-ray absorption spectroscopy (TEY-NEXAFS) spectra of rr-P3HT spin-cast from chlorobenzene onto OTS-treated and PDS-treated native silicon substrate. Top panel shows the spectra of the film at the air interface. Bottom panel shows the spectra of the film at the substrate interface revealed by gentle delamination. The average angle between the thiophene ring normal and the film normal is denoted by <α>.

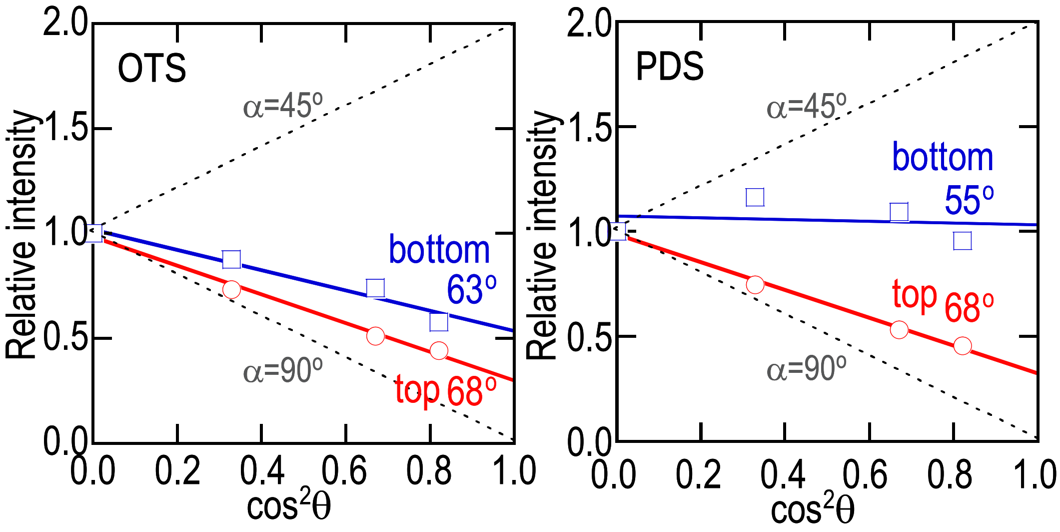

Figure 4.11 Dichroic analysis of the polarization-angle dependence of absorption of the incident X-rays for the $C_{1s}\rightarrow 1\pi^*$ transition at 285.0 eV for the film at the substrate interface (squares) and the air interface (circles).

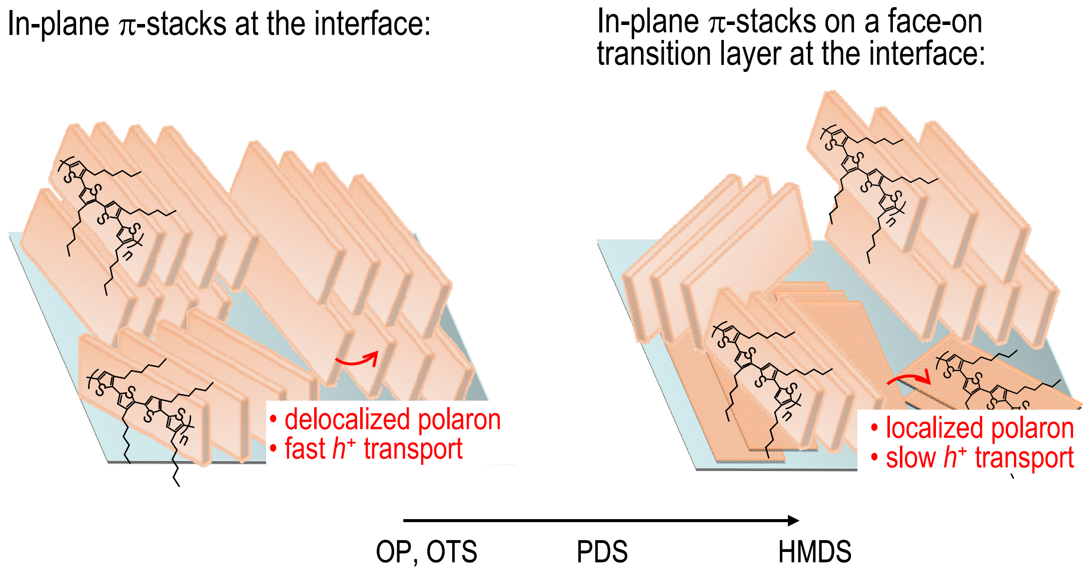

Figure 4.12 Approximate examples of rr-P3HT on SAM-modified surfaces.

4.3.3 Character of field-induced polarons

The optical signature of the polarons reveals a remarkable change in their character from small polarons on the HMDS surface to large (delocalized) polarons on the OP surface. Figure 4.14 shows the CMS spectra collected in the NIR–optical region of the four devices in the accumulation regime at 298 K. This experiment probes the higher-lying subgap transition of the polarons together with the charge-induced bleaching of the neutral rr-P3HT chain segments. Current–voltage (*IV*) characteristics of these FETs recorded before and after the CMS measurements showed that the FETs were not changed by the measurements. In particular the threshold V_g of all the FETs is similar (Figure 4.13). Two spectra are shown for each device, for high $\sigma_{dc} = 6.8 \times 10^{12}$ cm^{-2} and moderate $\sigma_{dc} = 3.8 \times 10^{12}$ cm^{-2}, with root-mean-square (rms) $\Delta\sigma = 0.2 \times 10^{12}$ cm^{-2} at 170 Hz, well within the bandwidth of the devices (a few kHz). These show that the CMS spectra of the modulated hole density change significantly with the dielectric interface but not with hole density. The quadrature spectra show no features, and hence there is no slow or irreversible process. CMS spectra were also collected when the devices were biased to depletion at V_g = +28 V (not shown) where the signal diminished as expected.

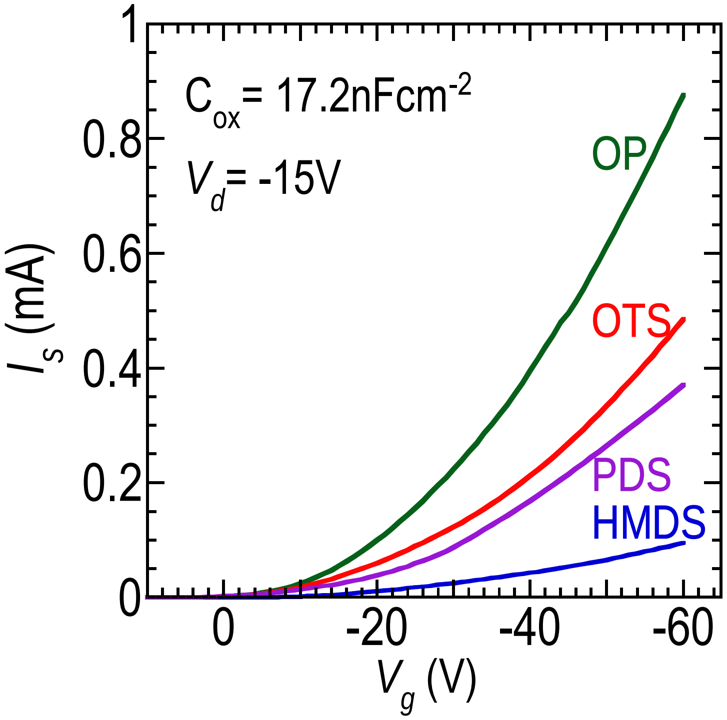

Figure 4.13 Transfer curve of devices fabricated on OP, OTS, PDS, and HMDS-treated substrates, measured before CMS experiments at 298K.

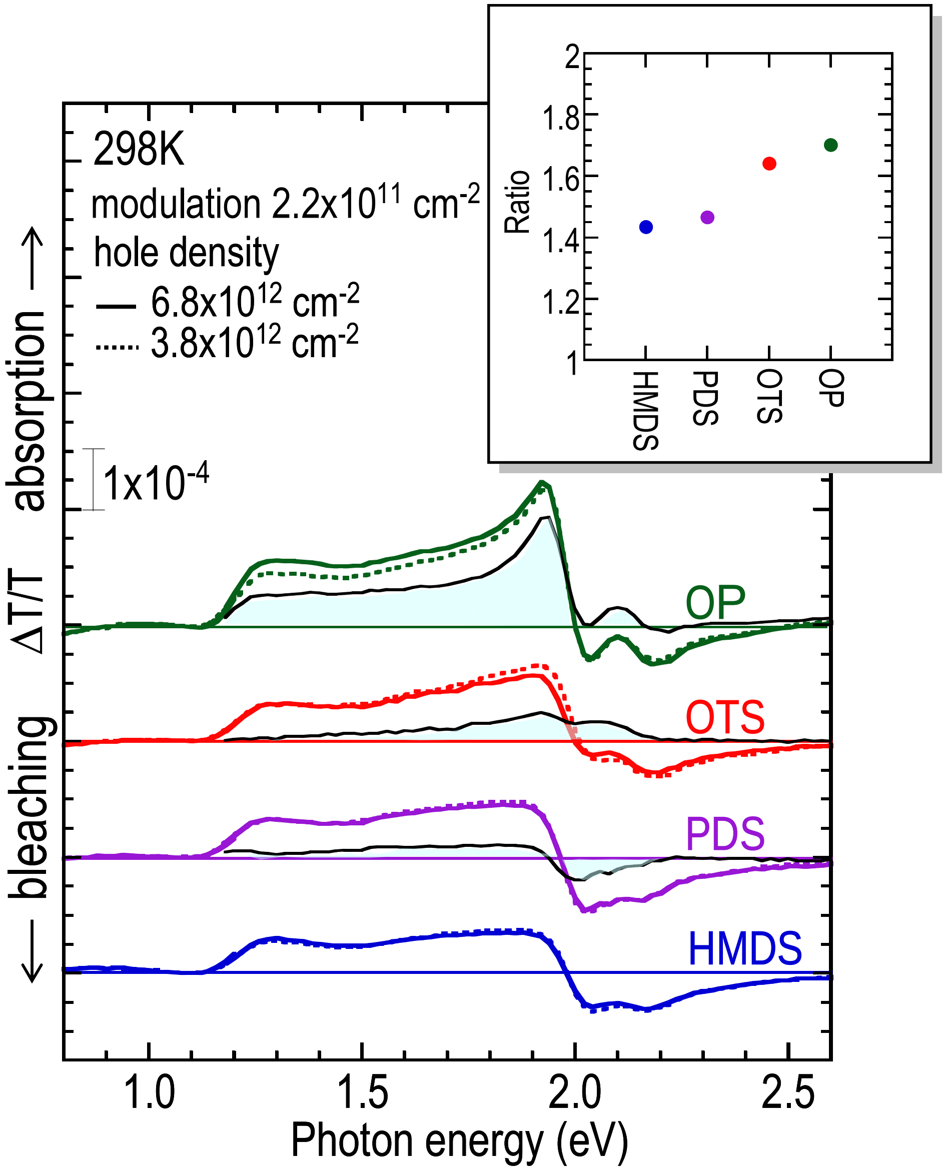

Figure 4.14 In-phase CMS optical spectra of the holes accumulated in the channel of rr-P3HT FETs fabricated on different surface-modified substrates measured at 298K (offset for clarity). Solid lines show spectra for high σ_{dc} = 6.8 x 10^{12} cm^{-2} and dotted lines show spectra for moderate σ_{dc} = 3.8 x 10^{12} cm^{-2}, with root-mean-square (rms) $\Delta\sigma$ = 0.2 x 10^{12} cm^{-2} at 170 Hz. Shaded regions represent spectrum difference against that of the HMDS device at σ_{dc} = 6.8 x 10^{12} cm^{-2}. The quadrature spectra show no features and hence no slow or irreversible processes. Inset shows the ratio of the delocalized polaron intensity at *ca*. 1.9 eV to the intensity at 1.28 eV.

The ground-state absorption region above 2.0 eV has been well-established to arise from bleaching of the ground-state π-π^* absorption ($\Delta T/ T > 0$).[9,29,35] This is characterized by two induced transmission bands at 2.04 and *ca*. 2.19 eV for all the devices here. The positions of these bands match very well the absorption shoulder (2.04 eV) and band maximum (2.21 eV) respectively in both the UV-Vis spectra (Figure 4.5 and Figure 4.7). However the spectral shapes differ across the devices. The OP-modified FET gives the best resolved features suggesting that polarons in this FET reside in the most ordered states.

The subgap region below 2.0 eV is also well-established previously to arise from induced absorption of the accumulated polarons.[9,29,36] Traditionally, the spectrum is interpreted as the sum of a “molecular” polaron at 1.35 eV and an interchain-delocalized polaron at 1.75 eV.[9,24,25] The spectra here suggest that an even more fully delocalized polaron than previously observed is found at 1.95 eV, which was found by subtracting the spectrum of the HMDS device from each of the other three devices, and shown as the shaded area in Figure 4.14. The blue-shift of the polaron electronic transition towards the π–π^* absorption edge has been predicted theoretically for a symmetric delocalized polaron dimer P_2^+ (where P represents a polymer chain segment).[37] A simple rationalization for the general case of P_n^+ based on a one-electron picture suggests that this inter-level transition broadens into an inter-band transition with spectral weight shifting to the π–π^* absorption edge.[25] The existence of such a fully-delocalized polaron has been observed previously in photoinduced absorption spectroscopy in rrP3HT film,[38,39] and in PBTTT FETs with well-ordered π-stacked lamellae,[16] but not yet in rrP3HT FETs.[9,36] Therefore we propose that the ratio of the delocalized polaron intensity at *ca*.

1.9 eV to the intensity at 1.28 eV provides a measure of the population of delocalized polarons. This ratio (inset of Figure 4.14) increases across HMDS < PDS < OTS < OP.

This result is further confirmed by CMS collected in the mid-infrared region which probes the lower-lying (and intra-band) electronic transition of the field-induced polarons together with the infrared-active vibrational (IRAV) modes[40,41] (Figure 4.15). The position and appearance of this transition also reveals the state of delocalization of these polarons. In addition the IRAV modes derive their oscillator strength from the coupling of lattice vibrations to polaron motion in the infrared field. This optical field-induced motion leads to absorption cross sections vastly larger than the intrinsic vibrational modes, and can therefore reveal information about the microscopic motion of these carriers. The CMS spectra of the four devices were obtained in accumulation at σ of 3.0×10^{12} cm^{-2} and rms $\Delta\sigma$ of 1.4×10^{12} cm^{-2}, also at 170 Hz and 298 K. The spectra exhibit a broad polaronic transition with an intensity that greatly increases across the series HMDS < PDS < OTS < OP. The spectral weight also red shifts across this series, which is a characteristic feature of increasing delocalization.

For the OP-surface, a series of IRAV peaks[40] were found at 1120, 1259 and 1387 cm^{-1}; and dips at 1061, 1209, 1357 1446 cm^{-1}. These band intensities decrease markedly across to HMDS-surface. The Raman modes of rrP3HT are found at 1377 and 1454 cm^{-1} and these modes are related to ring-breathing benzenoid→quinoid bond inversion modes coupled to the electronic transition. Therefore, the field-induced holes in OP device show strong coupling to these modes, which we relate to polaron motion along or across chain segments. On the other hand, the field-induced holes in the HMDS-device show weak coupling to these modes, but an intense coupling to the CH in-plane vibration mode of the thiophene rings. This suggests that these polarons are highly localized within the rings.

Hence it can be firmly concluded that holes are localized in the transition layers where these are present in the device.

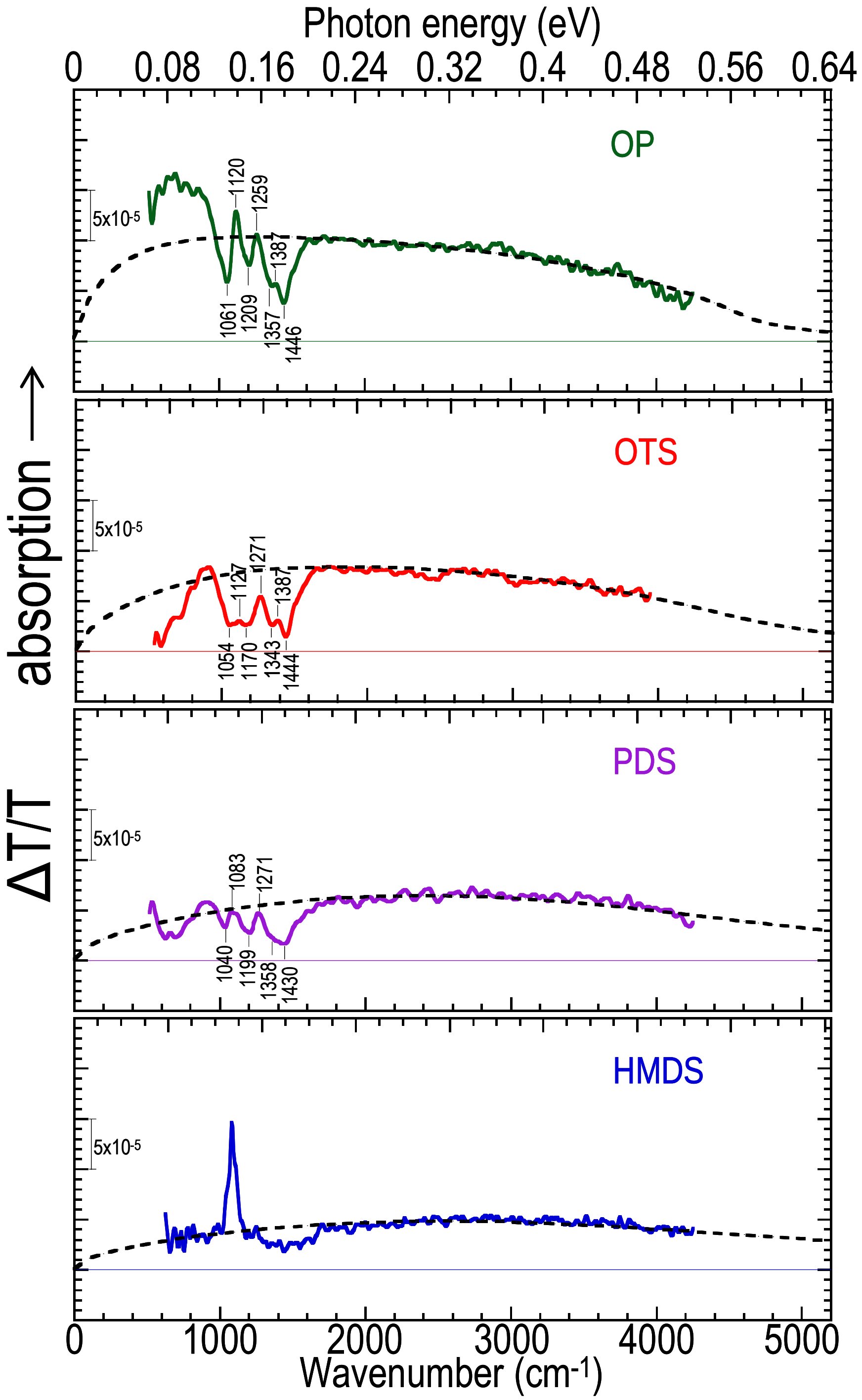

Figure 4.15 In-phase FT-IR CMS spectra for rr-P3HT transistors fabricated on SAM-modified surfaces at 298K. The devices were biased in the accumulation regime at σ_{dc} = 3.0x10^{12} cm^{-2}, with root-mean-square (rms) $\Delta\sigma$ = 1.4x10^{12} cm^{-2} at modulation frequency of 170 Hz. Solid lines represent data and horizontal lines indicated zero; dotted lines are guide to the eye.

4.3.4 Character of field-effect transport on different surfaces

We modelled the field-effect mobility versus hole density versus temperature (μ_{FET}-p-T) data to extract the transport parameters in the Coehoorn formalism based on hopping transport in a disordered Gaussian density-of-states DOS.[33] The results are shown in Figure 4.16 where the μ_{FET} at different hole carrier densities (p) for the four different devices were evaluated in a consistent way and fitted to the generalised Coehoorn hopping transport model described by:

$$\mu_{FET} = \frac{e\nu_o}{nk_BT}\phi\exp(-p_o - \ln(c) - (a\frac{\sigma_{DOS}}{k_BT} - \frac{E_f}{k_BT}) + \frac{d}{p_o}(\frac{\sigma DOS}{k_BT})^2),$$

where a and d are numerical constants taken from the Vissenberg-Matters model,[34] n is the 2D hopping site density, $p_o = (\frac{4B}{\pi}.\frac{\alpha^2}{n})^{\frac{1}{2}}$ and ν_o is the attempt frequency. A single σ_{DOS} was used for each device to obtain good fits where solid lines represent prediction and symbols represent the data. The results appear to be well described by the hopping model, suggesting that the macroscopic transport of these polarons is limited by hopping. The extracted E_f–p relationship and σ_{DOS} for these FETs (shown in Figure 4.17) shows that the width of the transport density-of-states and hence the gap between Fermi level and the transport level decreases in the order of OTS ≈ OP < PDS < HMDS. The required energetic hop to the percolating transport level near the DOS centre varies in the same sequence. In addition, the E_f for PDS and HMDS devices lie further than $2\sigma_{DOS}$ over the entire range of p compared to OTS and OP devices suggesting the presence of deep states.

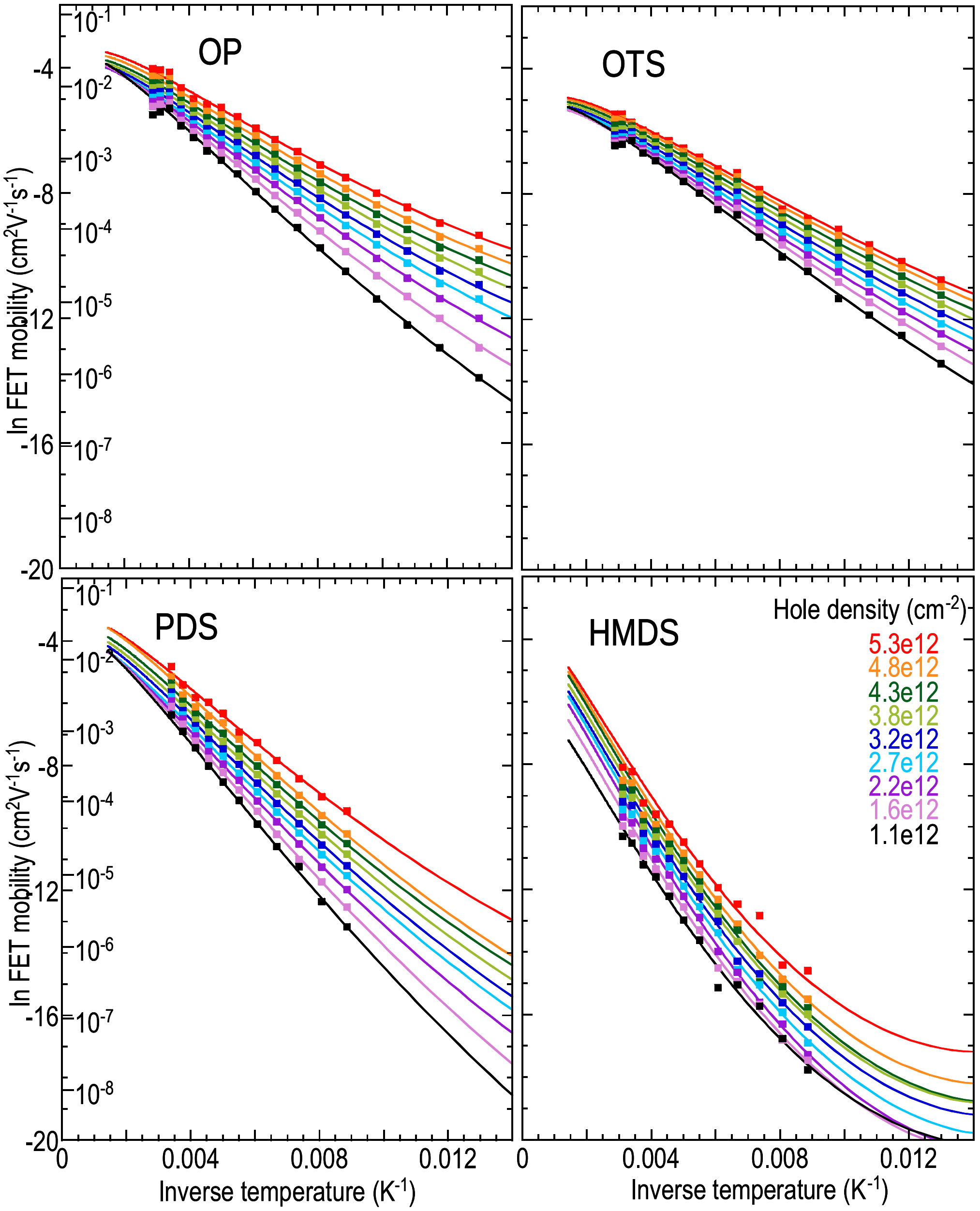

Figure 4.16 Plots of the field-effect mobility against inverse temperature at different hole densities. Symbols are data; lines represent predictions using the Coehoorn generalized hopping model. Inner scales on the left plots indicate μ_{FET} on a log scale.

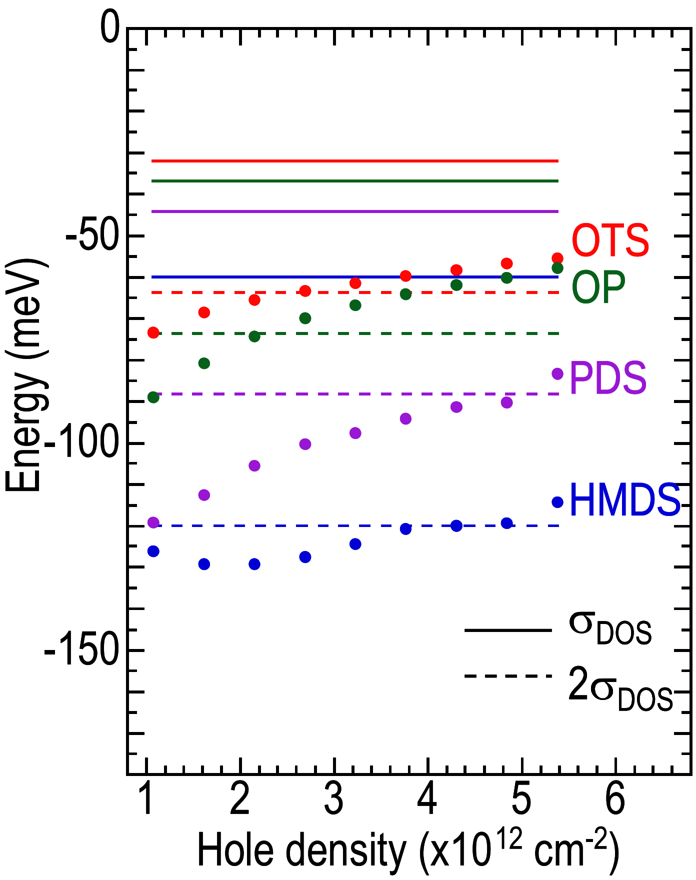

Figure 4.17 Plot of the Fermi energy and DOS width against hole densities for devices fabricated on OTS, OP, PDS and HMDS-treated substrates. Zero corresponds to the center of the Gaussian-like DOS.

4.4 Conclusion

The following picture emerges from the structural information, electrical transport characteristics and the optical signatures of these charge carriers. An ultrathin rr-P3HT wetting layer with flat conformation and face-on orientation of the chain can be formed at the dielectric substrate. This layer leads to strong charge localization and hence lowers carrier mobility by more than one order of magnitude. The significance of this finding is that a key towards higher and reproducible μ_{FET} is the suppression of the formation of this layer by controlling the Van der Waals energetics. Research is still in progress on this. Finally, this finding also explains why the μ_{FET} results coming from different laboratories may not agree if the formation of this transition layer becomes variable.

4.5 References

1 Park, S. K., Jackson, T. N., Anthony, J. E. & Mourey, D. A. High mobility solution processed 6,13-bis(triisopropyl-silylethynyl)pentacene organic thin film transistors. *Appl. Phys. Lett.* 91, 063514- 063511-063513 (2007).

2 Li, Y., Singh, S. P. & Sonar, P. A high mobility p-type DPP-thieno[3,2-b]thiophene copolymer for organic thin-film transistors. *Adv. Mater.* 22, 4862-4866 (2010).

3 Tsao, H. N. *et al.* Ultrahigh mobility in polymer field-effect transistors by design. *J. Am. Chem. Soc.* 133, 2605-2612 (2011).

4 Bronstein, H. *et al.* Thieno[3,2-b]thiophene-diketopyrrolopyrrole-containing polymers for high-performance organic field-effect transistors and organic photovoltaic devices. *J. Am. Chem. Soc.* 133, 3272-3275 (2011).

5 Bao, Z., Dodabalapur, A. & Lovinger, A. J. Soluble and processable regioregular poly(3-hexylthiophene) for thin film field-effect transistor applications with high mobility. *Appl. Phys. Lett.* 69, 4108-4110 (1996).

6 Chang, J.-F. *et al.* Enhanced Mobility of Poly(3-hexylthiophene) Transistors by Spin-coating from High-Boiling-Point Solvents. *Chem. Mater.* 16, 4772-4776 (2004).

7 Wang, G., Swensen, J., Moses, D. & Heeger, A. J. Increased mobility from regioregular poly(3-hexylthiophene) field-effect transistors. *J. Appl. Phys.* 93, 6137-6141 (2003).

8 Wong, L. Y. *et al.* Interplay of processing, morphological order, and charge-carrier mobility in polythiophene thin films deposited by different methods: Comparison of spin-cast, drop-cast, and inkjet-printed films. *Langmuir* 26, 15494-15507 (2010).

9 Sirringhaus, H. *et al.* Two-dimensional charge transport in self-organized, high-mobility conjugated polymers. *Nature* 401, 685-688 (1999).

10 Chang, J.-F. *et al.* Molecular-weight dependence of interchain polaron delocalization and exciton bandwidth in high-mobility conjugated polymers. *Physical Review B* 74, 115318 (2006).

11 Kline, R. J. *et al.* Dependence of regioregular poly(3-hexylthiophene) film morphology and field-effect mobility on molecular weight. *Macromol.* 38, 3312-3319 (2005).

12 Kline, R. J., McGehee, M. D., Kadnikova, E. N., Liu, J. & Fréchet, J. M. J. Controlling the field-effect mobility of regioregular polythiophene by changing the molecular weight. *Adv. Mater.* 15, 1519-1522 (2003).

13 Zen, A. *et al.* Effect of molecular weight and annealing of poly(3-hexylthiophene)s on the performance of organic field-effect transistors. *Adv. Funct. Mater.* 14, 757-764 (2004).

14 Chang, J.-F., Sirringhaus, H., Giles, M., Heeney, M. & McCulloch, I. Relative importance of polaron activation and disorder on charge transport in high-mobility conjugated polymer field-effect transistors. *Phys. Rev. B.* 76, 205204-205201 (2007).

15 Veres, J., Ogier, S. D., Leeming, S. W., Cupertino, D. C. & Khaffaf, S. M. Low-k insulators as the choice of dielectrics in organic field-effect transistors. *Adv. Funct. Mater.* 13, 199-204 (2003).

16 Zhao, N. *et al.* Polaron localization at interfaces in high-mobility microcrystalline conjugated polymers. *Nat. Mater.* 21, 1-5 (2009).

17 Salleo, A., Chabinyc, M. L., Yang, M. S. & Street, R. A. Polymer thin-film transistors with chemically modified dielectric interfaces. *Appl. Phys. Lett.* 81, 4383-4385 (2002).

18 Kim, D. H. *et al.* Enhancement of field-effect mobility due to surface-mediated molecular ordering in regioregular polythiophene thin film transistors. *Adv. Funct. Mater.* 15, 77-82 (2005).

19 Wu, Y. *et al.* Controlled orientation of liquid-crystalline polythiophene semiconductors for high-performance organic thin-film transistors. *Appl. Phys. Lett.* 86, 142102-142101- 142103 (2005).

20 van Krevelen, D. W. *Properties of polymers. Their correlation with chemical structure: their numerical estimation and prediction from additive group contributions*. 3 edn, (Elsevier, 1990).

21 Wasserman, S. R., Tao, Y.-T. & Whitesides, G. M. Structure and reactivity of alkylsiloxane monolayers formed by reaction of alkyltrichlorosilanes on silicon substrates. *Langmuir* 5, 1074-1087 (1989).

22 Le Grange, J. D., Markham, J. L. & Kurkjian, C. R. Effects of surface hydration on the deposition of silane monolayers on silica. *Langmuir* 9, 1749-1753 (1993).

23 Wang, Y. & Lieberman, M. Growth of ultrasmooth octadecyltrichlorosilane self-assembled monolayers on SiO2. *Langmuir* 19, 1159-1167 (2003).

24 Kobayashi, S. *et al.* Control of carrier density by self-assembled monolayers in organic field-effect transistors. *Nat. Mater.* 3, 317-322 (2004).

25 Zhao, L. H. *et al.* Manuscript submitted. (2011).

26 DeLongChamp, D. M. *et al.* Variations in semiconducting polymer microstructure and hole mobility with spin-coating speed. *Chem. Mater.* 17, 5610-5612 (2005).

27 Ho, P. K. H. *et al.* Solvent effects on chain orientation and interface pi-interaction in conjugated polymer thin fims: Direct measurements of the air and substrate interfaces by near-edge x-ray absorption spectroscopy. *Adv. Mater.* 19, 215-221 (2007).

28 Hao, X. T. *et al.* Control of the interchain pi-pi interaction and electron density distribution at the surface of conjugated poly(3-hexylthiophene) thin films. *J. Phys. Chem. B* 111, 10365-10372 (2007).

29 Brown, P. J. *et al.* Effect of interchain interactions on the absorption and emission of poly(3-hexylthiophene). *Phys. Rev. B.* 67, 064203 (2003).

30 McCulloch, I. *et al.* Liquid-crystalline semiconducting polymers with high charge-carrier mobility. *Nat. Mater.* 5, 328-333 (2006).

31 Chua, L. L. *et al.* Large damage threshold and small electron escape depth in X-ray absorption spectroscopy of a conjugated polymer thin film. *Langmuir* 22, 8587-8594 (2006).

32 Stöhr, J. *NEXAFS* spectroscopy (Springer-Verlag, 1992).

33 Coehoorn, R., Pasveer, W. F., Bobbert, P. A. & Michels, M. A. J. Charge-carrier concentration dependence of the hopping mobility in organic materials with Gaussian disorder. *Phys. Rev. B* 72, 155206-155201-155220 (2005).

34 Vissenberg, M. C. J. M. & Matters, M. Theory of the field-effect mobility in amorphous organic transistors. *Phys. Rev. B* 57, 12964-12967 (1998).

35 Brown, P. J., Sirringhaus, H., Harrison, M., Shkunov, M. & Friend, R. H. Optical spectroscopy of field-induced charge in self-organized high mobility poly(3-hexylthiophene). *Physical Review B* 63, 125204- 125201-125211 (2001).

36 Brown, P. J., Sirringhaus, H., Harrison, M., Shkunov, M. & Friend, R. H. Optical spectroscopy of field-induced charge in self-organized high mobility poly(3-hexylthiophene). *Phys. Rev. B* 63, 125204- 125201-125211 (2001).

37 Belijonne, D. *et al.* Optical signature of delocalized polarons in conjugated polymers. *Adv. Func. Mater.* 11, 229-234 (2001).

38 Jiang, X. M. *et al.* Spectroscopic studies of photoexcitations in regioregular and regiorandom polythiophene films. *Adv. Funct. Mater.* 12, 587-597 (2002).

39 Osterbacka, R., An, C. P., Jiang, X. M. & Vardeny, Z. V. Two-Dimensional Electronic Excitations in Self-Assembled Conjugated Polymer Nanocrystals. *Sci.* 287 (2000).

40 Horovitz, B. Infrared activity of Peierls systems and application to polyacetylene. *Solid State Commun.* 41, 729-734 (1982).

41 Lopez Navarrete, J. T. & Zerbi, G. Lattice dynamics and vibrational spectra of polythiophene. II: Effective coordinate theory, doping induced, and phoexcited spectra. *J. Chem. Phys.* 94, 965-970 (1991).

Chapter 5. Outlook

Polymer organic semiconductors are a promising new class of materials that opens up possibilities in niche electronic devices. The scientific insights discovered in this thesis provide leads in the molecular and device designs and in improving the ambient stability and performance of organic devices. The deeper understanding of the molecular mechanisms underpinning the behaviour of organic semiconductors in field-effect transistors exposed to the ambient provided important insights for rationale design and back-end encapsulation that will have immediate implications on device stability and technological applications. The successful development of a sensitive charge modulation spectroscopy technique provides an efficient way to study the nature of charge carriers in other organic semiconductor polymers. Using regioregular poly(3-hexylthiophene) (rr-P3HT) as a model system to describe the charge transport, morphology and nature of charge carriers, we found the formation of an ultrathin rr-P3HT transition layer at the gate dielectric interface depending on surface energetic that leads to charge carriers trapping. Moving forth, this finding provides opportunities for new processing conditions to achieve ultimately a delocalised charge transport and hence improving device performance.

Appendix

Publications related to work done in this thesis

3. J.-M. Zhuo, L.-Y. Wong, H. Guo, L.-H. Zhao, X.-Y. Gao, A. T.-S. Wee, L.-L. Chua, P. K.-H. Ho, "Effect of dielectric surface on polymer chains alignment and charge transport in poly(3-hexylthiophene) thin film: nanostructure effects", manuscript in preparation.
4. J.-M. Zhuo, L.-H. Zhao, R.-Q. Png, L.-Y. Wong, P.-J. Chia, J.-C. Tang, S. Sivaramakrishnan, M. Zhou, E. C.-W. Ou, S.-J. Chua, W.-S. Sim, L.-L. Chua, P. K.-H. Ho, "Direct spectroscopic evidence for a photodoping mechanism in polythiophene and poly(bithiophene-alt-thienothiophene) organic semiconductor thin films involving oxygen and sorbed moisture", *Adv. Mater*., 21 (2009) 4747
5. J.-M. Zhuo, L.-H. Zhao, P.-J. Chia, W.-S. Sim, R. H. Friend, P. K.-H. Ho, "Direct evidence for delocalization of charge carriers at the Fermi level in a doped conducting polymer", *Phys. Rev. Lett.*, 100 (2008) 186601

Publications (up till 2011) from work not described in this thesis

1. L.-H. Zhao, R.-Q. Png, J.-M. Zhuo, H. Guo, J.-C. Tang, L.-Y. Wong, R. H. Friend, L.-L. Chua, P. K.-H. Ho, "A new twist in semicrystalline π-conjugated organic semiconductors and polaron delocalization", manuscript submitted.

2. L.-H. Zhao, R.-Q. Png, J.-M. Zhuo, L.-Y. Wong, J.-C. Tang, Y.S. Su, L.-L. Chua, “A general method to induce macroscopically well-oriented lamellar order π-stackable polymer films using borderline-poor solvents”, manuscript submitted.
3. L.-H. Zhao, R.-Q. Png, J.-M. Zhuo, J.-C. Tang, P. K.-H. Ho, L.-L. Chua, “Polymer chain-length dependence of thermal transitions of the alkyl side-chains and π-conjugated backbone of a semicrystalline polythiophene polymer”, manuscript submitted
4. P.-J. Chia, L.-L. Chua, S. Sivaramakrishnan, J.-M. Zhuo, L.-H. Zhao, W.-S. Sim, Y.-C. Yeo, P. K.-H. Ho, “Injection-induced de-doping in a conducting polymer during device operation: Asymmetry in the hole injection and extraction rates”, *Adv. Mater.*, 19 (2007) 4202

Conference presentations

J.-M. Zhuo, L.-H. Zhao, R.-Q. Png, L.-Y. Wong, P.-J. Chia, J.-C. Tang, S. Sivaramakrishnan, M. Zhou, E. C.-W. Ou, S.-J. Chua, W.-S. Sim, L.-L. Chua, P. K.-H. Ho, “Direct spectroscopic evidence for a photodoping mechanism in polythiophene and poly(bithiophene-alt-thienothiophene) organic semiconductor thin films involving oxygen and sorbed moisture”, Materials Research Society (MRS) Spring Conference, 5- 9 April 2010, San Francisco, USA (Oral presentation)

J.-M. Zhuo, L.-H. Zhao, R.-Q. Png, L.-Y. Wong, P.-J. Chia, J.-C. Tang, S. Sivaramakrishnan, M. Zhou, E. C.-W. Ou, S.-J. Chua, W.-S. Sim, L.-L. Chua, P. K.-H. Ho, "Direct spectroscopic evidence for a photodoping mechanism in polythiophene and poly(bithiophene-alt-thienothiophene) organic semiconductor thin films involving oxygen and sorbed moisture", International Conference on Materials for Advanced Technology (ICMAT), 28 June- 3 July 2009, Singapore (Poster presentation)

L.-H. Zhao, J.-M. Zhuo, P.-J. Chia, W.-S. Sim, R. H. Friend, P. K.-H. Ho, "Direct evidence for delocalization of charge carriers at the Fermi level in a doped conducting polymer", European Materials Research Society (E-MRS) Spring Conference, 26- 30 May 2008, Strasbourg, France (Poster presentation)

J.-M. Zhuo, L.-H. Zhao, P.-J. Chia, W.-S. Sim, P. K.-H. Ho, "Charge modulation spectroscopy of charge carriers in a conducting polymer thin film", International Conference on Materials for Advanced Technology (ICMAT), 1- 6 July 2007, Singapore (Poster presentation)